The Dissertation Committee for Lanlan Gu

certifies that this is the approved version of the following dissertation:

Micro- and nano-periodic-structure-based devices for laser beam control

Committee:

Ray T. Chen, Supervisor

Sanjay K. Banerjee

Ananth Dodabalapur

Michael F. Becker

Paul S. Ho

Micro- and nano-periodic-structure-based devices for laser beam control

by

Lanlan Gu, B.S., M.S., M.S.E.

Dissertation

Presented to the Faculty of the Graduate School of

the University of Texas at Austin

in Partial Fulfillment

of the Requirements

for the Degree of

Doctor of Philosophy

The University of Texas at Austin

August 2007

Dedicated to my parents, husband, and daughter

Acknowledgements

I would like to thank my advisor, Dr. Ray Chen, for his guidance and support in every aspect of my research. I also would like to thank Dr. Sanjay K. Banerjee, Dr. Ananth Dodabalapur, Dr. Michael F. Becker, and Paul S. Ho, for serving on my dissertation committee and giving insightful advices on my dissertation research. Many thanks go to my fellow group members in the Optical Interconnect Group at University of Texas at Austin. They have been good friends and often provided valuable inputs and stimulating discussions into my doctoral research.

Last but not a bit least, I wish to express my deepest gratitude to my great parents Xingbao Gu and Xiuying Jiang, and my beloved husband Minhao Wu. They have been there for me every step of the way, showing endless love and unconditional support. Special appreciation goes to my dear father, who has influenced me in many ways, and who has been my role model, my confidant, my mentor every since I can remember.

Lanlan Gu

Univeristy of Texas at Austin

August, 2007

Micro- and nano-periodic-structure-based devices for laser beam control

Publication No. __________

Lanlan Gu, Ph.D.
The University of Texas at Austin, 2007

Supervisor: Ray T. Chen

With the progress of microfabrication and nanofabrication technologies, there has been a reawakened interest in the possibility of controlling the propagation of light in various materials periodically structured at a scale comparable to, or slightly smaller than the wavelength. We can now engineer materials with periodic structures to implement a great variety of optical phenomena. These include well known effects, such as dispersing a variety of wavelength to form a spectrum and diffracting light and controlling its propagation directions, to new ones such as prohibiting the propagation of light in certain directions at certain wavelengths and localizing light with defects in some artificially synthesized dielectric materials. Advances in this field have had tremendous impact on modern optical and photonic technologies. This doctoral research was aimed at investigating some of the physics and applications of periodic structures for building blocks of the optical communication and interconnection system.

Particular research emphasis was placed on the exploitation of innovative periodic structure-based optical and photonic devices featuring better functionality, higher performance, more compact size, and easier fabrication. Research topics extended from one-dimensional periodic-structure-based wavelength-division-multiplexing (WDM) optical interconnects (beam wavelength selection devices), and liquid crystal beam steerers (beam steering devices), to two-dimensional periodic-structure-based silicon photonic-crystal thermo-optic and electro-optic modulators (beam switching devices).

This research was specifically targeted to seek novel and effective solutions to some long-standing technical problems, such as the limited wavelength coverage of coarse WDM devices, small bandwidth of highly dispersed dense WDM devices, low deflection efficiency of high-resolution liquid crystal beam steerers, slow switching speed, large device size, and high power consumption of silicon optical modulators, among others. For each subtopic, research challenges were presented and followed by the proposed solutions with extensive theoretical analysis. The proposals were then verified by experimental implementations. Experimental results were carefully interpreted and the future improvements were also discussed.

Table of Contents

Chapter 1

Introduction

Chapter 2

Chapter 4

Chapter 5

Chapter 6

Chapter 7

Appendix

List of Figures

List of Tables

Chapter 1

Introduction

1.1 A brief history of the study of light wave diffraction by periodic structures

The study of the diffraction of electromagnetic wave by periodic structures has a long history since that goes back to the 18th century [1]. Diffraction is defined as the bending and spreading of a traveling wave when it encounters an obstruction that has a dimension similar to its wavelength. If the obstruction is periodic, or indeed if there is a periodic variation of refractive-index which affects the propagation of wave in the optical region, the mutual interference of the scattered waves leads to reflection or transmission of the incidence in discrete directions. Diffraction effects are seen both in nature and at home: they are responsible for the sheen of some bird feathers, for the colors that are observed on gramophone records, and for the colored patterns that are seen when a street light is viewed through the fabric of an umbrella. However, the real importance of diffraction effects is the fact that they provide an effective mechanism to build various functional photonic devices for applications of controlling and manipulating the light flow.

Research of the diffraction from light started with one-dimensional (1-D) structures whose dielectric constants are periodically modulated on the wavelength scale. This kind of 1-D periodic structure is usually called diffraction grating. American astronomer David Rittenhouse made the first diffraction grating in 1785, and reported constructing a half-inch-wide grating with fifty-three apertures [2]. However, it is Joseph von Fraunhofer who deserves the credit for the invention of the diffraction grating as we know it today. In 1821, unaware of the earlier American report, he produced reflection gratings which enabled him to measure the absorption lines of the solar spectrum. He also derived and verified grating equations. His work inspired other efforts in the areas of fabrication and analysis of diffraction gratings. The distribution of incident field power of a given wavelength diffracted by a grating into the various diffraction orders depends on many parameters, including the power and polarization of the incident light, the angle of incidence, the (complex) index of refraction of the grating materials, and the grating spacing. Principally, gratings can be classified to work in two regimes: Raman-Nath regime and Bragg regime [3]. A complete treatment of grating efficiency for both requires solving Maxwell's equations. However, with a series of fundamental assumptions, both have analytical solutions. Raman-Nath regime of diffraction is characterized by many propagation orders so that no single one is predominant. It usually happens in the 'thin' grating where the thickness of the planar grating is thin. Bragg regime of diffraction is characterized by two order of propagation, usually the 0th (transmission) and the 1st (diffraction) orders. In most cases it occurs in a 'thick' grating as well as the incidence satisfies the Bragg condition. We will review the theories, fabrications and applications of diffraction gratings in more detail later.

Although 1-D periodic structures have received intensive study for more than a century, it was not until 1987 that the principle of 1-D diffraction effects was extended to two-dimensional (2-D) and three-dimensional (3-D) periodic structures [4, 5]. The new classes of 2-D and 3-D periodic optical structures were named photonic crystals (PhCs). Unlike 1-D Bragg grating which prohibits light propagation within a frequency range at a specific angle, 3-D PhCs can under certain conditions open a fairly large photonic-band-gap (PBG) for a forbidden frequency range in all directions and 2-D PhCs may result in PBG in all directions within a 2-D plane [6-9]. Examples of the schematic and band diagram of 1-D, 2-D, 3-D periodic structures are illustrated in Fig. 1.1.1 [6]. The work done in the first four or five years was mostly theoretical studies, the great concern of which was determining the type of structure and the difference of relevant refractive indices suited to obtain a full PBG. Experimentally, E. Yablonovitch and his coworkers verified for the first time the existence of a full PBG for a 3-D PhC in 1991 with a lattice constant in the micrometer region [10]. In the near-infrared or optical region, 2-D samples began being successfully fabricated in the first half of the 1990s. However, a 3-D sample with a full band gap, which was a main target of the research, was still technically difficult to fabricate. Around 1999, Noda and his coworkers succeeded, for the first time, in fabricating such a sample [11]. In the past few years, a variety PhCs of good quality were fabricated, which have enabled one to conduct various novel experiments in relation to the unique and

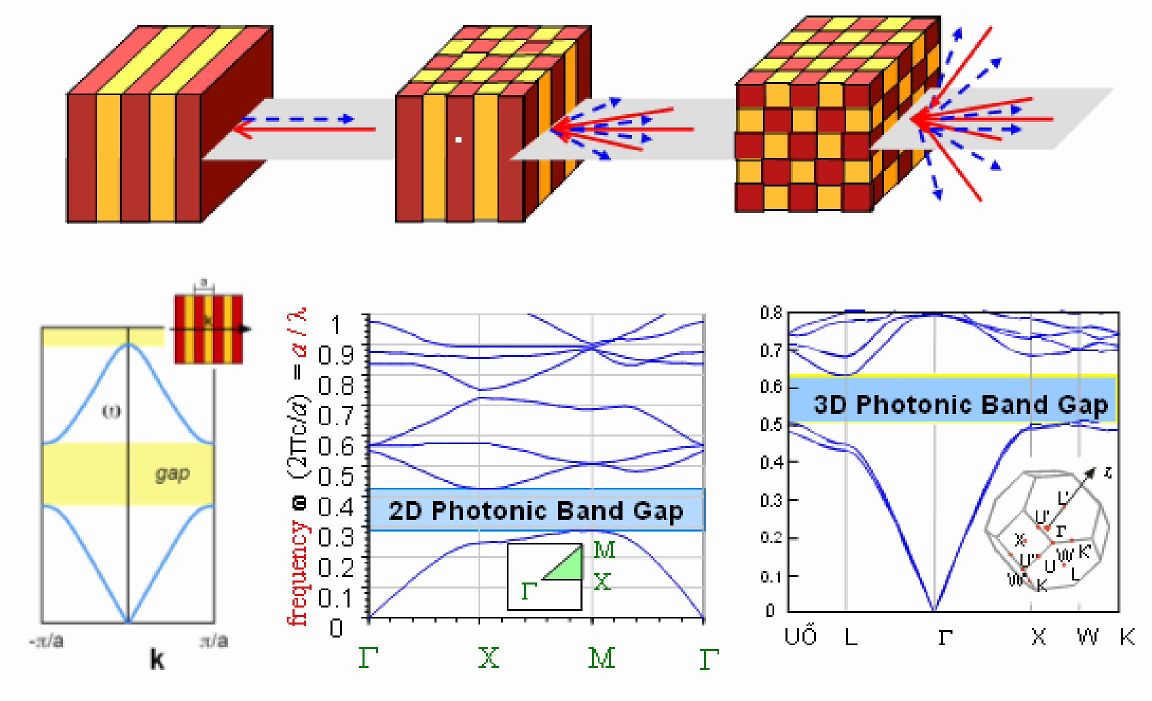

Fig. 1.1.1 Examples of the schematic and band diagram of 1-D, 2-D, 3-D periodic structures [6].

distinguished characteristics of the photonic band structures (PBSs). By making good use of those characteristics, a number of new physical phenomena and novel optoelectronic devices have been anticipated or proposed. As a result, many attractive devices have been developed, with some being already commercially available. For the descriptions of the fundamentals and applications of PhCs, please see section 1.3.

1.2 Overview of one dimensional periodic structures — gratings

Optical gratings may be of the surface-relief (corrugated) type with periodic variation in surface of a dielectric or conducting materials, or may be of the planar (slab) type with periodic modulation in the permittivity (or equivalent index of refraction) or in the conductivity (or equivalent absorption), or a combination of these. The related work in this doctoral research was mainly focused on the planar (slab) gratings.

1.2.1 Grating theories

The analysis of diffraction by spatially periodic media has a long history. Numerous methods with various assumptions have been used to analyze the diffraction characteristics, such as the order, direction and amplitude of the diffracted electromagnetic wave. A thorough review of those theoretical treatments was given by T. K. Gaylord in reference [3]. The common methods of analyzing diffraction by grating are the modal approach (sometimes referred to as Floquet, Floquet-Bloch approach) and the coupled-wave approach (occasionally called coupled-mode approach). Both of these approaches can produce the exact formulations without approximations. In fact, these formulations are completely equivalent in their full rigorous forms. They are merely alternative mathematical representations of the total electromagnetic field inside the grating region, and associated with each representation is a different physical perspective. With some specific assumptions which apply to different real cases accordingly, these complicated rigorous treatments can be reduced to various approximate theories, such as two-wave modal theory, two-wave second-order coupled-wave theory, multi-wave coupled-wave theory, two-wave first-order coupled-wave theory (Kogelnik theory), optical path method, Raman-Nath theory, and amplitude transmission theory. Each simplified theory is only valid within its appropriate limits. For details, please refer to reference [3].

The most obvious feature of the diffraction by gratings is the appearance of multiple propagating backward- and forward-diffracted orders that typically exist outside the grating region, as illustrated by the wave-vector diagram in Fig. 1.2.1. The total normalized electric field in region 1 and region 3 can be expressed as

$$E_1 = \exp(-j\vec{k}\cdot r) + \sum_{i=-\infty}^{\infty} R_i \exp(-j\vec{k}_{1i}\cdot\vec{r}) \quad , \qquad (1.2.1)$$

$$E_3 = \exp(-j\vec{k}\cdot r) + \sum_{i=-\infty}^{\infty} T_i \exp(-j\vec{k}_{3i}\cdot(\vec{r} - d\hat{z})) \quad , \qquad (1.2.2)$$

where Ri and Ti are the normalized amplitude of the i-th reflected and transmitted wave in region 1 and region 2, respectively, d is the thinness of the grating region, $\vec{k}$ represents the wave vector, and i is the integer to label the order of space-harmonic component of the field. To ensure the phase matching condition, each i-th component in region 1 and 3 should be phase matched to the i-th component inside the grating, namely, region 2. Thus we have

$$n_1 \sin\theta_i' = n_1 \sin\theta - i(\lambda/\Lambda)\sin\phi \quad , \tag{1.2.3}$$

$$n_3 \sin\theta_i'' = n_1 \sin\theta \; - i(\lambda/\Lambda)\sin\phi \quad , \tag{1.2.4}$$

where n1 and n3 are the indices of refraction of region 1 and 3, respectively. Λ and Φ are the period and the slanted angle of the grating, θ, θ', and θ" are the angles for incidence, backward and forward diffractions, respectively. Fig. 1.2.1 intuitively visualizes that the

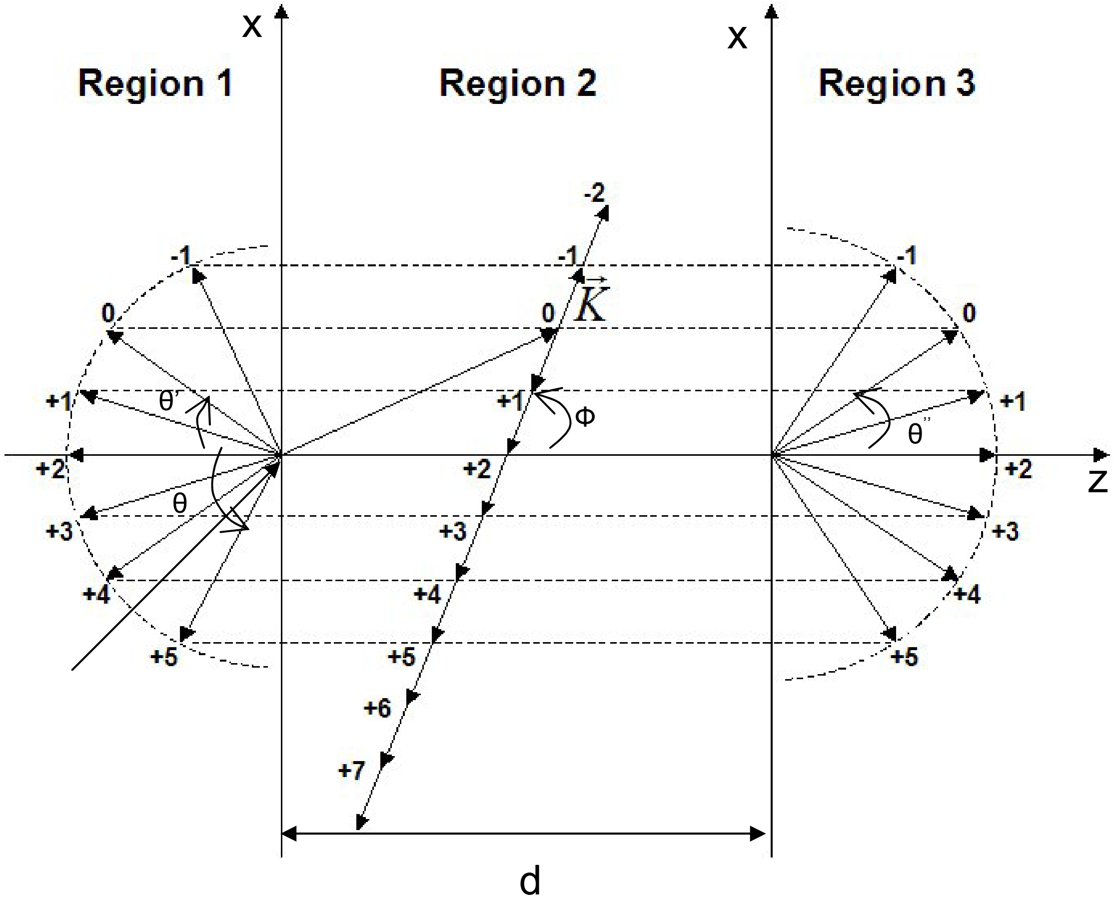

Fig. 1.2.1 Wave vector diagram illustrating phase matching of the space-harmonic components of the total electromagnetic field inside the grating (region 2) with the propagating backward-diffracted orders (region 1), the

propagating forward-diffracted orders (region 3), and the evanescent waves outside the grating [44].

incident homogeneous plane wave may be divided into many diffracted inhomogeneous plane waves that have directions given by equation (1.2.3) and (1.2.4), and the $i = 0$ inhomogeneous plane wave corresponds to the refracted incident wave. Actually, for each order of backward or forward-diffraction in region 1 and 3, it may be either propagating wave or evanescent wave. As exhibited by the horizontal dashed lines in Fig. 1.2.1, the i-th space-harmonic component inside the grating region produces a phase matched i-th field, respectively, in region 1 and 3. Outside the grating region, the field whose wave vector can be literally drawn on the semicircle in region 1 or 3 is a propagating wave, otherwise an evanescent wave.

Solving the rigorous coupled-wave equations is sometimes unnecessarily tedious and time-consuming. Therefore, there has been lots of work carried out on the approximate theories of grating analysis. There are a large number of possible approximations and assumptions that can be made. From the rigorous theory along with a series of fundamental assumptions and simplifications, the exact formulations can be reduced to a variety of approximate theories. In some cases, the simplifications even allow the solutions in analytical forms to be obtained. By neglecting the second derivatives and the boundary effects of the field amplitudes in the wave equation, the rigorous theory is simplified to the first-order coupled-wave theory. Studies have shown that this simplified theory gives accurate results in transmission gratings when the grating modulation is small, which is actually the scenario for most real applications. Under this assumption, the occurrence of diffraction can be categorized into either in the “Raman-Nath regime” or in the “Bragg regime”. The criteria for the regimes of diffraction behavior were discussed in references [12-13]. Diffraction in the Raman-Nath grating is usually taken as being synonymous with “thin” grating diffraction or the presence of multiple grating diffracted orders with diffraction efficiency η_i given by

$$\eta_i = J^2{}_i(2\gamma) \quad , \tag{1.2.5}$$

where i is the integer representing the diffracted order. J_i is integer order ordinary Bessel functions of the first kind, and γ is the grating strength parameter which is given by

$$\gamma = \pi \Delta n d / \lambda \cos\theta \ , \tag{1.2.6}$$

where Δn is the amplitude of the refractive index change, d is the thickness of the grating, λ is the free-space wavelength, and θ is the angle of incidence inside the grating region. Raman-Nath regime is usually defined as diffraction occurs when

$$Q'\gamma \leq 1 \quad , \tag{1.2.7}$$

where Q' is defined as [13]

$$Q' = Q / \cos\theta = 2\pi\lambda d / n_0 \Lambda^2 \cos\theta \, . \tag{1.2.8}$$

In contrast, diffraction in the Bragg regime is usually taken as being synonymous with "thick" grating diffraction or the presence of a single diffracted wave with diffraction efficiency η_1 given by

$$\eta_1 = \sin^2 \gamma \ . \tag{1.2.9}$$

Bragg regime diffraction occurs when

$$Q'/2\gamma \geq 10 \, , \tag{1.2.9}$$

and the incidence should also be at or near the Bragg angle. Both diffractions have importance practical applications in modern optical technology. Their broad applications will be reviewed later.

1.2.2 Fabrication of gratings

In the early days of the surface-relief grating, the grating grooves were usually formed by using a ruling engine or replication technologies. However, the resolution, quality, and expense are all critical issues which limit the resulting gratings for practical applications. The invention and development of laser made it possible to produce the grating by optical inference. The grooves of the grating can be formed by laser recording on photosensitive materials, followed by a chemical development process. The spacing of the fringes is determined by the angle of intersection of the beams and by the wavelength of light. Since the position of the grooves is determined by the conditions of interference, a grating made in this way will be free from the random and periodic errors presenting in a grating from a ruling engine. The grooves of the grating can be also formed on a photographic film by a series processing steps such as exposure, development and fixing. Such photographic gratings serve a role of particular importance in optical information processing systems.

There are many methods to achieve slab gratings [15]. The fabrication techniques are drastically different depending on the material properties, working mechanism and application of gratings. For example, acousto-optic grating consists of a transparent medium (e.g. a liquid or a transparent crystal) into which acoustic waves can be launched by a piezoelectric transducer. Magneto-optic grating consists of a two-dimensional array of magneto-optic elements in the form of individually isolated means on an epitaxially grown magnetic garnet film, mounted on a transparent nonmagnetic backing substrate. Liquid-crystal thin-film grating exploits the ability to change refractive index by means of applied electric fields. Usually those fields are applied between the glass plates that contain the liquid crystal material using transparent conductive layers (indium tin oxide film) coated on the inside of the glass plates. All of the aforementioned examples are actively controlled slab gratings. For passive slab gratings, good examples are the holographic gratings recorded by two-laser-beam interference on dry photopolymers such as Dupont photopolymer or wet processed Dichromated gelatin (DCG) films. Because Dupont-photopolymer-based holographic-volume gratings and liquid-crystal thin-film gratings are among the major topics explored in this doctoral research, details about the fabrications for both gratings will be presented in section 2.1.2 and section 4.3, respectively, in the context of the discussions on the correspondingly developed optical devices.

1.2.3 Applications of gratings

Applications of gratings are broad and varied, which extend widely into fields of acoustic-optics, integrated optics, holography, optical data processing, and spectral analysis. Good examples include [3]: acoustic wave generation, ambiguity processing, analog-to-digital conversion, antennas, associative storage, beam coding, beam coupling, beam deflection, beam splitting, coherent light generation, convolution processing, correlation processing, data processing and optical logic, data storage, diagnostic measurements, displays, distributed feedback, filtering, head-up displays, holographic optical elements, imagine amplification, image processing, incoherent-to-coherent converter, instrumentation, interferometry, lenses, mode conversion, modulation, monochromator, multi-port storage, multiple beam generation, multiplexing, de-multiplexing, optical testing, pattern recognition, phase conjugation, pulse shaping and compression, Q-switching, mode locking, resonator mirror, signal processing, solar concentration, spatial light modulators, spectral analysis, and switching. In this doctoral research, a considerable portion of efforts have been devoted to exploring the practical applications of diffraction gratings (1-D periodic structures) for laser beam de-multiplexing and laser beam steering. A comprehensive description will be reported in chapters 2, 3 and 4.

1.3 Overview of two dimensional (2-D) and three dimensional (3-D) periodic structures — photonic crystals (PhCs)

Photonic crystals (PhCs) are a new class of artificial optical materials composed of periodic dielectric structures with different permittivity and feature size on the order of optical wavelengths. They are put into two categories, 2-D and 3-D, depending on the dimensionality of the stacks. PhCs provide a lot of unique and interesting properties, such as the formation of photonic band gap (PBG), slow group velocity, super-prism effect, control over spontaneous emission rates etc. [6-9], which promise to provide revolutionary solutions to the miniaturization of integrated photonic circuit. In this section, we will briefly review the fundamentals and applications of PhCs.

1.3.1 Fundamentals of photonic crystals: Maxwell's equations, Bloch-Floquet theorem, Photonic band gap (PBG), Localized defect state.

To learn the basics of photonic crystals, we should start with the Maxwell's equations. The Maxwell's equations in UGS-Gaussian system are shown as follows [6, 7]

$$\begin{aligned}
&\nabla \bullet \vec{H}(\vec{r},t) = 0,\\
&\nabla \times \vec{H}(\vec{r},t) = \frac{4\pi}{c}\vec{j} + \frac{1}{c}\frac{\partial(\varepsilon(\vec{r})\vec{E}(\vec{r},t))}{\partial t} = 0,\\
&\nabla \bullet \varepsilon(\vec{r})\vec{E}(\vec{r},t) = 4\pi\rho,\\
&\nabla \times \vec{E}(\vec{r},t) = -\frac{1}{c}\frac{\partial(\vec{H}(\vec{r},t))}{\partial t} = 0,
\end{aligned} \tag{1.3.1}$$

where E and H are the electrical and magnetic fields, ε is the permittivity, μ is the permeability, t is the time, and r is the displacement to origin, c is the speed of light in vacuum, j .is the free current density, ρ is the free charge density. In general, both E and H are complicated functions of time and space. But we can separate out the time dependence by expanding the fields into a set of harmonic mode

$$\begin{aligned}
&\vec{H}(\vec{r},t) = \vec{H}(\vec{r})e^{i\omega t},\\
&\vec{E}(\vec{r},t) = \vec{E}(\vec{r})e^{i\omega t},
\end{aligned} \tag{1.3.2}$$

because of the linearity of the Maxwell's equation. By plugging Eq. 1.3.2 into the Maxwell equation only in the case where no free charges and currents are available, we have relation between the E and H as

$$\begin{aligned}
&\nabla \times \vec{H}(\vec{r}) - \frac{i\omega}{c}(\varepsilon(\vec{r})\vec{E}(\vec{r})) = 0,\\
&\nabla \times \vec{E}(\vec{r}) + \frac{i\omega}{c}\vec{H}(\vec{r}) = 0.
\end{aligned} \tag{1.3.3}$$

An equation entirely expressed in H is obtained by eliminating E

$$\vec{\nabla} \times (\frac{1}{\varepsilon(\vec{r})}\vec{\nabla} \times \vec{H}) = \frac{\omega^2}{c^2}\vec{H}. \tag{1.3.4}$$

This become as Hermitian eigen-alue problem with the eigen-value proportional to $(\frac{\omega}{c})^2$.

This master equation determines the modes H and E given the specific $\varepsilon(\vec{r})$ and ω.

In PhCs, the permittivity ε is a periodic function of position, which can be expressed as

$$\varepsilon(\vec{r}) = \varepsilon(\vec{r} + \vec{a}). \tag{1.3.5}$$

The Bloch-Floquet theorem tells us that for a Hermitian eigen-problem whose operators are periodic function position, the solution can always be chosen of the form $\exp(i\vec{k}\cdot\vec{r})$. By applying this theorem, we have

$$\vec{H}(\vec{r}) = \exp(i\vec{k}\cdot\vec{r})\vec{H}_{n,\vec{k}}(\vec{r}) \ , \tag{1.3.6}$$

$$\vec{H}_{n,\vec{k}}(\vec{r}+\vec{R}) = \vec{H}_{n,\vec{k}}(\vec{r}) \, ,$$

where $\vec{H}_{n,\vec{k}}$ is the periodic function of position. By substituting Eq. 1.3.6 into the master equation, Eq. 1.3.4, we have

$$(\vec{\nabla}+i\vec{k})\times\frac{1}{\varepsilon}(\vec{\nabla}+i\vec{k})\times\vec{H}_{n,\vec{k}} = -\frac{\omega_n(\vec{k})^2}{c^2}\vec{H}_{n,\vec{k}} \tag{1.3.7}$$

Since $\vec{H}_{n,\vec{k}}$ is the periodic function of position, we need only consider the eigen-problem over the unit cell of the periodicity. The eigen-frequency ω_n is a discrete value because this is an eigen-problem within a finite domain. When ω_n is plotted as the function of wave vector k, we get the frequency band structure of the crystal, which is analogous to the electron energy band structure in the semiconductors. Because the ω_n is a discrete value, there will be difference of ω_n between two bands at a fixed wave vector k. To obtain a full photonic band gap (PBG), the gaps at all k must overlap in some frequency range. The reason why a PhC with high index contrast can be used to obtain such a full 'gap' is that the large difference in ε usually causes large enough gaps in different directions to ensure an overlap among them. The propagation of light is inhibited in all directions inside 3-D PBGs whereas it is forbidden in a 2-D plane inside 2-D PBGs. If the periodicity of PhCs is broken by some introduced defects, typically either point defects or line defects, some defect-supported modes that lie inside the PBG will be produced and localized in the vicinity of the defects. These modes are called localized modes. A point defect is simply a defect of finite extent in all direction, which forms a micro-cavity and thus supports a resonant mode. The strong localization and the high cavity Q value of the point-defect mode inside PhCs allow for a fast and strong spontaneous emission of the active material. Conversely, a line defect is a defect that extends periodically with infinite extent in one axial direction and with finite extent in the lateral directions. It introduces guided-mode bands inside PBG and forms a waveguide in either 2-D or 3-D PhCs. Unlike traditional index-guided waveguides, however, a photonic-crystal waveguide cannot radiate laterally even in the presence of disorder or additional defects. In other words, light can only be scattered forward or backwards. In turn, it forms an effective one-dimensional system in which many simple resonant phenomena can be explored.

1.3.2 Fabrications and applications of photonic crystals

Experimental progress has been made in parallel with extensive theoretical studies. Nanotechnology has been widely used for the fabrication of 3-D PhCs with a full PBG in the optical region. Many techniques have been investigated [8], such as dry etching technique, wafer-fusion technique, self-organization of nano-sphere, infiltration of a high refractive index material into opal crystals, one-by-one manipulation technique, alto-cloning technique, interference pattern exposure, scanning exposure of a focused light beam, and etc. A vast majority of the experimental work has been carried out to develop 2-D PhC slabs because of their simplicity in fabrication, compared with 3-D PhCs, and the significance in realization of novel integrated photonic devices. 2-D slabs are usually composed of a thin film of semiconductor with an arrangement of holes, which is sandwiched between materials with low refractive indices. A strong optical confinement in the vertical direction can be achieved within the slab due to the available large index contrast. This structure can be realized by various competing manufacturing technologies, such as e-beam lithography, dry etch, selective growth, anodic oxidation and so on [8]. Point defect laser oscillation by photo-pumping under low temperature in the 2-D PhC slab was demonstrated by Scherer et al. [15] and Lee et al. [16]. Following this pioneering work, low threshold room temperature operation has been achieved in various modified structures. 2D band-edge- effect-based lasers [17] and PhC LED with high light extraction efficiency [18] were also reported. Among all the investigations of 2-D PhC slab, line-defect photonic crystal waveguides (PCW) have attracted the most attention. This is because of the superior guiding performance and unique dispersion property of the PCW, which enable the realization of ultra-compact photonic integrated circuit. Many efforts have been devoted to the development of cost-effective line-defect PCWs on silicon-on-insulator (SOI) wafers using well established silicon VLSI technologies. In this doctoral research, we investigated the slow group velocity of the PCW. Great efforts have been made to develop ultra-compacted thermo-optic and electro-optic silicon modulators based on PCWs. Please see chapter 4 and 5 for details of the correlated work.

1.4 Research motivations s and contributions

This doctoral research is aimed at investigating some of the physics and applications of periodic structures for building block elements in the optical communication and interconnection systems. Particular research emphasis was placed on the exploitation of innovative periodic-structure-based optical and photonic devices featuring better functionality, higher performance, more compact size and easier fabrication. My research was specifically targeted to seek novel and effective solutions to some long-standing technical problems, which are associated with the researched laser- beam-controlling devices, such as the limited wavelength coverage of coarse WDM devices, small bandwidth of highly dispersed dense WDM devices, low deflection efficiency of high-resolution liquid-crystal laser-beam steerers, slow switching speed, large device size and high power consumption of silicon optical modulators, and etc. The major contributions of my doctoral work include:

- A polymer volume grating-based four-channel coarse wavelength division multiplexer (CWDM) for inter- and intra-satellite optical communication application was reported for the first time. This compact four-channel WDM device working at 0.83μm, 1.06μm, 1.34μm and 1.55μm was designed to build a complete optical link between two satellites, where wavelengths of 0.83μm and 1.55μm are used for data stream channels, 1.06μm and 1.34μm are used for inter-satellite and intra-satellite connection. It was for the first time reported that a WDM device can cover such a large wavelength range in a single substrate. Wavelength shifts due to Doppler Effect, temperature variations and radiation effects in space can be adequately accommodated in our designed device structure.
- A phase-compensation scheme was proposed and demonstrated to overcome the intrinsic tradeoff between the dispersion and the bandwidth of a volume grating. Its

application to a volume-grating-based dense-wavelength-division-multiplexing (DWDM) device was explored. To achieve phase compensation of the Bragg condition, a wavelength-dependent incident angle for a dispersion-enhanced holographic grating at 82 ^{o} is generated through a pre-staged volume hologram at 45 ^{o}. The 3dB dispersion bandwidth is increased by 5 times by using such a device configuration. A 21-channel DWDM device centered at 1555 nm with 200 GHz spacing is demonstrated within its 3dB bandwidth.

- A liquid-crystal (LC)-based high-resolution switchable grating was proposed by using a double-sided structure, where striped electrodes are patterned on both sides of the LC cell. A unique biasing configuration was employed to successfully minimize the distortion of the LC director profile due to the fringing-field effects under two-dimensional electric fields. A first order diffraction angle of 14.5^{o} with a diffraction efficiency of 33% for transmission light at 1.55 μm was experimentally achieved. This result approached the theoretical upper limit of 33.8% for a sinusoidal phase grating. The device efficiency was enhanced by 80 times compared to a conventional single-sided device.
- Ultra-compact thermo-optically-tuned photonic crystal waveguide (PCW) silicon-on-insulator Mach-Zehnder interferometers (MZIs) have been proposed and fabricated. A novel thermal design was employed to improve the device switching performance. Both steady-state and transient thermal analyses were performed to evaluate the thermal performance of the thermo-optic MZIs. A switching time less than 20 μs has been experimentally achieved, which clearly demonstrated the speed advantage using the new heating approach. The active length of the PCW based MZIs was 80 μm, nearly one order of magnitude shorter than the conventional silicon waveguide based MZIs.
- A silicon Mach-Zehnder interferometer (MZI) modulator featuring p-i-n-diode-embedded photonic crystal waveguides has been fabricated. Electrical simulations have been performed to design and analyze the device. The device interaction length was reduced by one order of magnitude compared to the conventional rib waveguide based MZI modulators owing to the slow group velocity exhibited by photonic crystal

waveguides (PCWs). High-speed optical modulation at 1 Gbit s^{-1} in the 1.55 μm wavelength region was experimentally demonstrated under an optimized driving signal. To our knowledge, it is the fastest speed ever achieved for a p-i-n diode based integrated silicon MZI modulator.

1.5 Dissertation arrangement

This dissertation is arranged as follows. Chapter 1 gives an introduction of the fundamentals, including physics, theory and applications, of one-dimensional and two-dimensional periodic optical structures. Chapter 2 reports a polymer volume grating-based four-channel coarse wavelength division multiplexer (CWDM) for inter- and intra-satellite optical communication application. The design details and experimental demonstration of a single-substrate-based CWDM device featuring extremely large wavelength coverage are presented. Chapter 3 describes a novel phase-compensation scheme. Its application in the highly dispersed volume based DWDM devices and the resultant improvements in device performance are also presented. Chapter 4 is focused on the demonstration of a high-efficiency and high-resolution liquid crystal beam steering device. A novel double-sided device structure along with a unique biasing configuration to solve the electrical fringing-field effects, which determines the performance of high-resolution liquid-crystal-based optoelectronic devices, is proposed. Extensive simulations and experimental implementations are discussed as well. Chapter 5 describes a new device concept of incorporating photonic crystal waveguide into conventional Mach-Zehnder interferometer modulators. An ultra-compact thermo-optically tuned silicon modulator employing this new concept was theoretically simulated and experimentally demonstrated. Chapter 6 discusses a high-speed p-i-n diode based ultra-compact photonic crystal electro-optic silicon modulator. Details of the extensive electrical simulations and experimental trials are included. Recommendations for future work are addressed as well. Chapter 7 summarizes the entire dissertation.

Chapter 2

1-D periodic-structure-based device (I): Holographic-grating-based four-channel coarse wavelength-division-multiplexing (CWDM) device for optical satellite communications

2.1 Introduction

2.1.1 Research motivation

The concept of space-based free-space optical communications among satellites was developed in the early 1960s [19]. However, there was no system demonstration until 2001 by ASTRIUM [20] due to the complexity of ultra-precise beacon acquiring, tracking and pointing technology. For data rates above 1Gbit s^{-1}, optical intersatellite links (ISLs) outperform conventional RF links in terms of high data rate, huge transmission capacity, low power consumption, small size and light weight. While space-ground links have been, and will continue to be dominated by RF links due to severe atmosphere and weather interference at optical frequencies, global optical backbone networks, i.e., space-based optical ISLs are believed to be the future replacements of their microwave counterparts [21]. Inter-satellite optical communication requires three wavelengths to complete the simplest point-to-point data transfer between two satellites. One laser beam is used as an information carrier, a second laser beam is used as a tracking and pointing beacon, a third laser beam works for intra-satellite communication. A lot of the earlier work was done based on 0.8 μm technologies with which the research about the free space optical communications started [22]. However, current plans call for continuous investigations of medium bit rate (300 Mbit s^{-1}) systems using 0.8 μm technology and new investigations of high rate (1.2 Gbit s^{-1}) systems using 1.5 μm technology, which is now available due to terrestrial fiber systems development [23], [24].

Coarse wavelength-division-multiplexing (WDM) technology, which is developed for storage access networks (SANs), finds its great potential for applications in the space-based optical communication system. The data bit rate independence of the WDM technology [25] makes it even more attractive in space-based application because it permits excellent upgrading compatibility of the current on-board network. In this chapter, a coarse photopolymer volume holographic grating based WDM device is proposed and developed. Our proposed four-channel CWDM device which covers both 0.83μm and 1.55 μm data stream channels works properly in the current optical satellite medium bit rate systems based on 0.8 μm technology and its good performance can also be maintained in the future high bit rate system using 1.5 μm technology. This broad-band four-wavelength CWDM is designed to provide two data streams at 0.83μm and 1.55μm, an inter-satellite tracking channel at 1.06μm, and an intra-satellite communication channel at 1.34μm.

2.1.2 Two-wave first-order coupled-wave theory

Volume holographic grating is a “thick” grating that usually works in the Bragg regime. Light diffraction in such a thick holographic grating occurring at or near the Bragg angle leads to efficient wave-front reconstruction, and thus provides important applications in a variety of optical systems. As discussed earlier (in chapter 1, section 1.2.1), various approximate theories have been developed to simplify the analysis of gratings with good accuracies under some specific assumptions that apply to the investigated systems. The two-wave first-order coupled-wave theory, which neglects second derivatives, boundary effects and higher orders wave ($i \neq 0,1$), was first applied to holographic grating by Herwig Kogelnik [26]. His paper published in 1969 is widely referenced to analyze the holographic gratings, and this theory is commonly called the “Kogelnik theory”. His theory is based on a few assumptions:

(1) The spatial modulation of the refractive index and the absorption constant is of a sinusoidal form.

(2) The holographic grating is thick and the monochromatic light incident on the grating is at or near the Bragg angle. Therefore, only two waves obeying the Bragg condition at least approximately are retained, other diffraction orders are neglected.

(3) The same average dielectric constant is assumed for the region inside and outside the grating boundaries, which means that all second derivatives of the field amplitudes from the rigorous coupled-wave equations and their correspondent boundary conditions are eliminated from the derivation of this theory.

The substantial recognition received by Kogelnik theory is in part because it provides analytical solutions for a comprehensive coverage of (1) phase, absorption, and mixed gratings; (2) on-Bragg and off-Bragg incidence; (3) pure transmission and pure reflection in general slanted fringe gratings; (4) both TE-mode and TM-mode polarization.

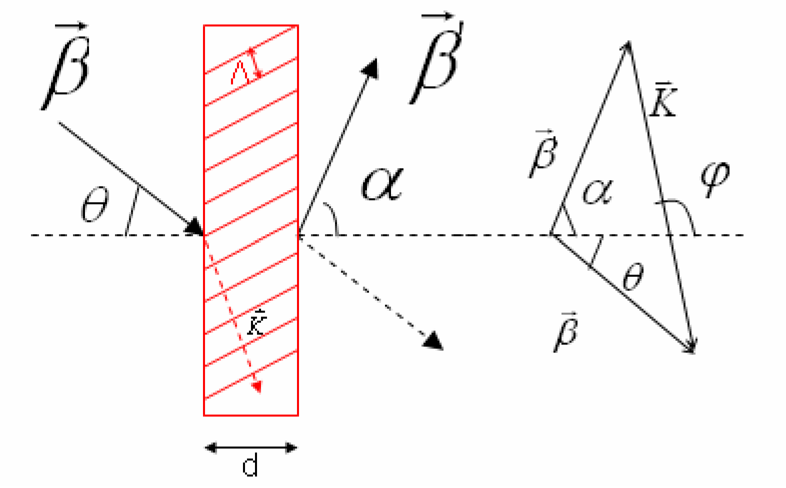

Fig. 2.1.1 Vector diagram for Bragg regime diffraction.

For transmission holographic grating, the analytic expression of the diffraction efficiency of a transmission volume grating for TE-mode is given by

$$\eta = \sin^2(\upsilon^2 + \xi^2)^{1/2} / (1 + \xi^2 / \upsilon^2), \qquad (2.1.1)$$

$$\upsilon = \frac{\pi \Delta n d}{(c_R c_S)^{1/2}}, \qquad (2.1.2)$$

$$\zeta = -\Delta\lambda K^2 d / 8\pi n c_{S_s}, \qquad (2.1.3)$$

$$c_R = \cos\theta, \tag{2.1.4}$$

$$c_S = \cos\theta - \frac{K}{\beta}\cos\varphi, \tag{2.1.5}$$

$$K = \frac{4\pi n}{\lambda_0}\cos(\varphi - \theta), \tag{2.1.6}$$

$$\beta = \frac{2\pi n}{\lambda}. \tag{2.1.7}$$

where θ is the designed incident angle inside the holographic grating, λ_o is the designed wavelength in air, φ is the slant angle of volume grating, d is the sickness of the grating, K is the grating vector, n is the average refractive index modulation of the recording medium, and Δn is the maximum index modulation of the photopolymer which can be controlled by exposure dosage. All of these parameters are illustrated in Fig 2.1.1. For TM mode, most equations above are valid except a change on υ to υ', which becomes $\upsilon' = -\upsilon\cos 2(\theta - \varphi)$.

2.1.3 Volume holographic grating formation on Dupont's photopolymer

DuPont's photopolymers for holographic recording offer significant advantages over conventional holographic recording medium such as dry-processing capability, long shelf life, good photo-speed, and large index modulation [27, 28]. These photopolymers are not a single material, but consist of a polymeric binder, photo-initiator, polymerizable monomers, sensitizing dyes, and occasionally other ingredients such as plasticizers and surfactants. These compositions are manufactured by dissolving ingredients in a suitable organic solvent, typically a mixture of methylene chloride and methanol, and casting the solution onto a clear solid film support of poluethylene terephthalate (Mylar) using conventional web coasters equipped with either a doctor knife or extrusion die along with an in-line drier and lamination station. A cover sheet of thin Mylar is laminated to the slightly tacky coatings after drying. The cover sheet protects the soft, tacky photopolymer layer from dust and handling. It can be removed prior to imaging, allowing the material to be laminated to glass, plastic or other substrates.

The formation of the volume holographic gratings in photopolymer films can be briefed as follows [27]. The monomer inside the photopolymer films starts to polymerize in regions exposed to bright interference fringes during the holographic recording. As conversion of monomer to photopolymer occurs, fresh monomer diffuses in from neighboring dark regions, thus setting up concentration and density gradients that result in refractive index modulation. The decrease in molecular volume associated with converting monomer to polymer is probably a major factor in drawing additional un-reacted monomer into the polymerization region. As exposure and polymerization proceed, the initial highly viscous composition gels and hardens, diffusion is then suppressed, and further hologram recording stops. At this point, the hologram image consists of photopolymer-rich regions that monomer diffused into and binder-rich regions that it diffused away from, probably with some residual un-reacted monomer distributed throughout. The hologram is now stable toward further exposures. Sometimes, a final simple heating process can help enhance the index modulation through additional diffusion and distribution of components between the photopolymer-rich and binder-rich regions of the hologram. A detailed description of the recording steps can be found in reference [29].

2.1.4 Setup for recording Dupont photopolymer based volume holographic gratings

DuPont photopolymer HRF 600X001-20 (20 μm thick) made by DuPont (DuPont Holographic Materials, Wilmington, Delaware) was used as the recording medium for volume hologram recording. The hologram was fabricated by a two-beam interference method using the setup shown in Fig. 2.1.2. The 532 nm line from a Verdi laser was used as the light source for exposure. An electrically timed shutter was employed to accurately control the exposure time. The S-polarization (E perpendicular to plane of incidence) laser beam was first split into two beams with equal power by a beam splitter. A half-wave plate in conjunction with a polarizing beam splitter was used to adjust the intensity of one beam and maintain the polarization of the adjusted beam as well. To eliminate the inevitable involved scattering noise, a pinhole was situated at the focal point for an objective lens for each beam to perform the spatial filtering. Two collimating objective lenses were employed to collimate the focused laser beams into plane waves, and expand them to be much larger than the recording area, which guaranteed the uniformity of the formed grating structures. A reflection mirror was mounted on a rotational stage to bend one laser beam towards the recording stage. A glass holder was mounted on a 3-D translational/rotational recording stage. The glass was painted dark to reduce the Fresnel reflection that may cause interference noise during the hologram construction. Recording angles of two beams can be adjusted by tuning the rotational angles of the mirror and recording stage. For the fabrication of hologram, dry photopolymer films were laminated onto a substrate (BK-7 or quartz). The protection Mylar cover was removed just prior to the recording. The device substrate was placed against the glass holder with some index-matching liquid sealing in between. Two finely adjusted laser beams interfered and created an image with a periodic pattern, which in turn exposed the photopolymer and led to an internal spatial index modulation.

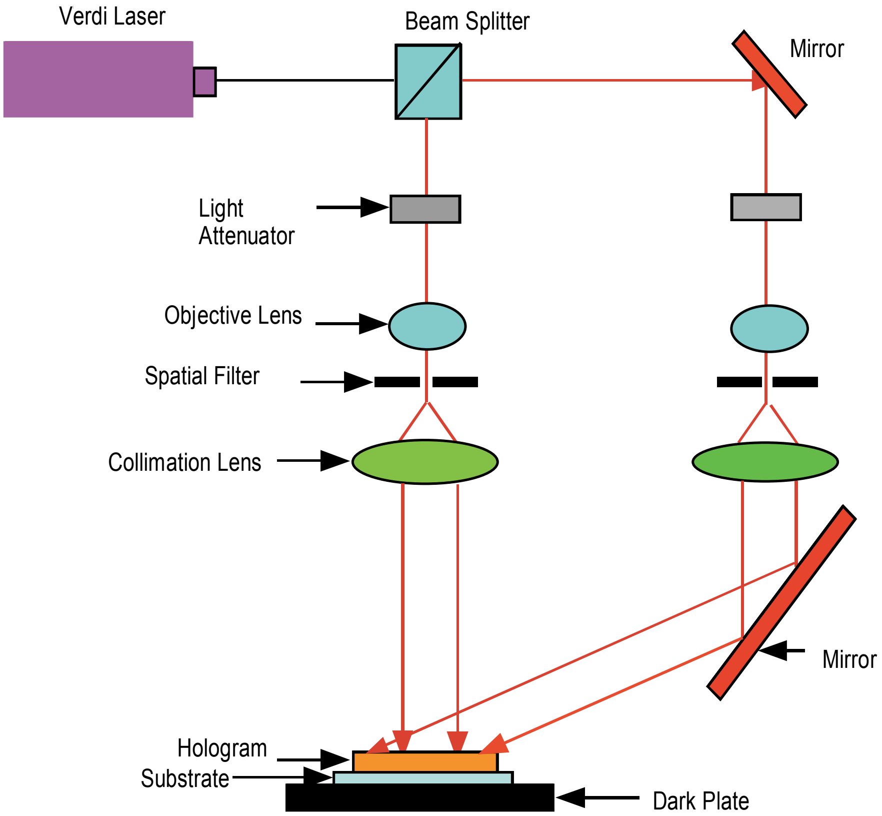

(a)

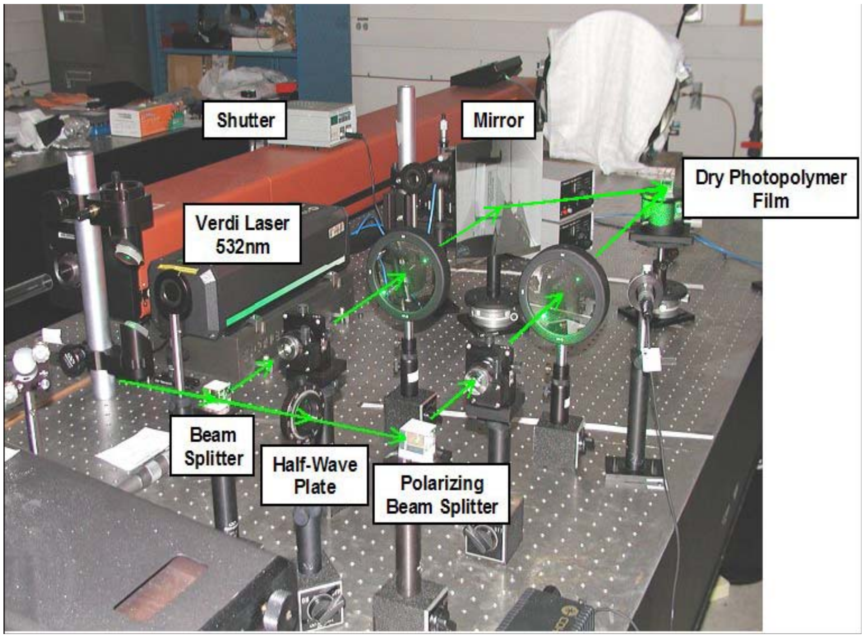

(b)

Fig. 2.1.2 Setup for holographic recording: (a) schematic (adapted from [30]); (b) real on-site shoot (adapted from [31]).

2.2 Design of volume holographic gratings for four-channel CWDM device

2.2.1 Design of device structure

The schematic and the real device picture of the four-channel CWDM device using four photopolymer-based holographic gratings in conjunction with substrate-guided waves are shown in Fig. 2.2.1 and Fig. 2.2.2, respectively. An aluminum-coated beveled edge was used to couple optical signals into the wave-guiding plate with a bouncing angle larger than the critical angle of total internal reflection (TIR) of the glass substrate [32]. Four volume holographic gratings were recorded to provide surface-normal fan outs for four different wavelengths, i.e. 0.83 μm, 1.06 μm, 1.34 μm and 1.55 μm. Independent zigzag guided beams of their designated wavelengths were selectively coupled out from one of the four outputs at their Bragg angles. The wavelength separation and channel spacing for our CWDM can be designed depending on different requirements to the targeted applications. In this work, a beveled edge was designed at the input end to maximize the coupling of the optical signal into the glass substrate. The beveled edge was coated with aluminum film with reflection efficiency higher than 99%. The wedge angle was designed at 22.5 ^{o} to router normal incident signals into the wave-guiding plate shown in Fig. 2.2.1 with a TIR bouncing angle at 45 ^{o}. In this work, 4-mm-thick optically flat glass plate was used as the wave-guiding plate for all four wavelengths. To facilitate the output coupling and packaging, physical separation of the adjacent channels was designed to be 8mm. The total length of this device was 4cm.

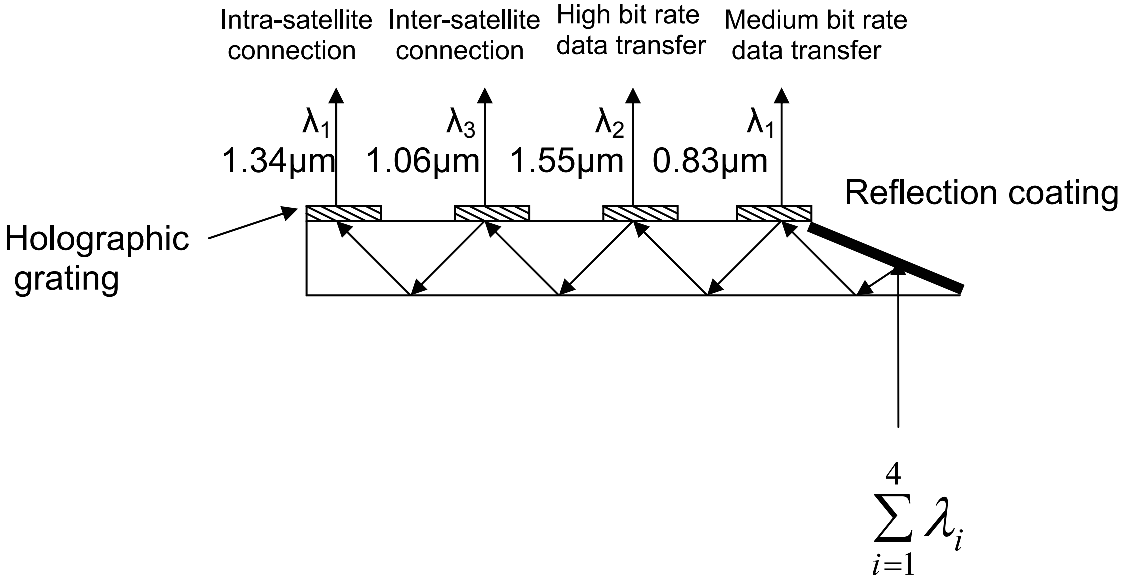

Fig. 2.2.1 Schematic of four–channel CWDM device using four photopolymer-based holographic gratings in conjunction with substrate-guide waves.

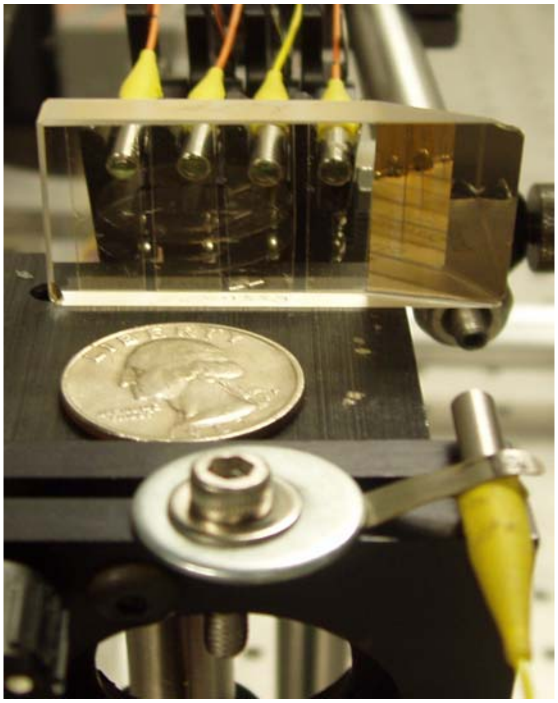

Fig. 2.2.2 Device picture of photopolymer volume-holographic-grating-based four–channel CWDM device.

Diffraction efficiency of a transmission volume grating can be calculated by using couple mode theory [26], which we have introduced in section 2.1.2. As in equation 2.1.1 to 2.1.6, θ is the designed incident angle for holographic grating which is 45 ^{o} for all wavelengths, λo is the designed channel wavelength, φ is the slant angle of volume grating, n is the average refractive index modulation of the recording medium (DuPont HRF 600X001-20 photopolymer), which is close to 1.51. Δn is the maximum index modulation of the photopolymer that can be controlled by exposure dosage. Signal beams at λo can be coupled out efficiently through their correspondent holographic gratings, which are designed to satisfy Bragg condition at 0.83µm, 1.06µm, 1.34µm and. 1.55µm, respectively. The thickness (d) of HRF 600X001-20 photopolymer is 20 µm. In principle, 100% channel efficiency can be achieved if Δn is optimized to the required values for different channels. In our design, index modulations of 0.018, 0.023, 0.028 and 0.031 for TE mode and 0.026, 0.032, 0.04, 0.045 for TM mode are required to achieve

100% efficiency for channels at 0.83μm, 1.06μm, 1.34μm and 1.55μm. The simulation results are shown in Fig 2.2.3. It is clearly 100% channel efficiency can be achieved for each channel if the index modulation is chosen properly. It is also seen that four wavelengths at 0.83μm, 1.55μm, 1.06μm, and 1.34μm can be easily separated by the designed CWDM. Any wavelength selective device used on board of a satellite must be able to accommodate the wavelength shifts due to Doppler effect, temperature variations and radiation effects in space [33]. Therefore, wide bandwidth is always preferred for a WDM in space-based optical application.

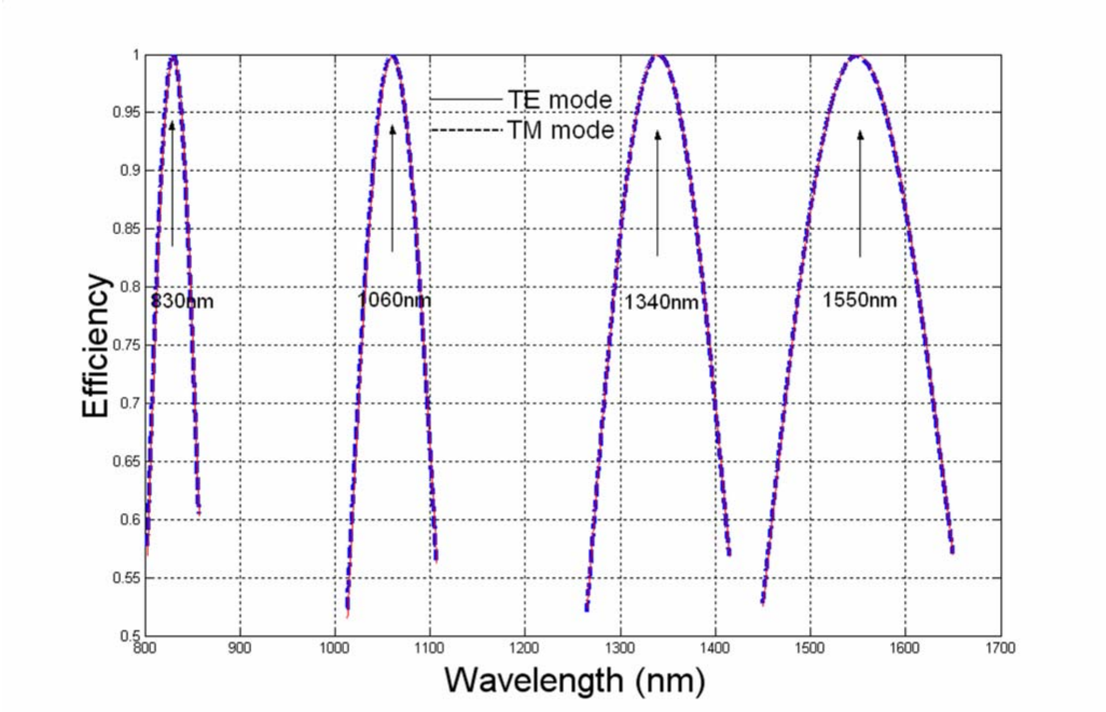

Fig. 2.2.3 Simulation results of diffraction efficiency versus wavelength for both the TE and TM waves at incident angle of 45 °, for photopolymer films with thickness of 20μm. Refractive index modulations (Δn) of 0.018, 0.023, 0.028, 0.031 for TE mode and 0.026, 0.032, 0.04, 0.045 for TM mode are used for channels at 0.83μm, 1.06μm, 1.34μm and 1.55μm, respectively.

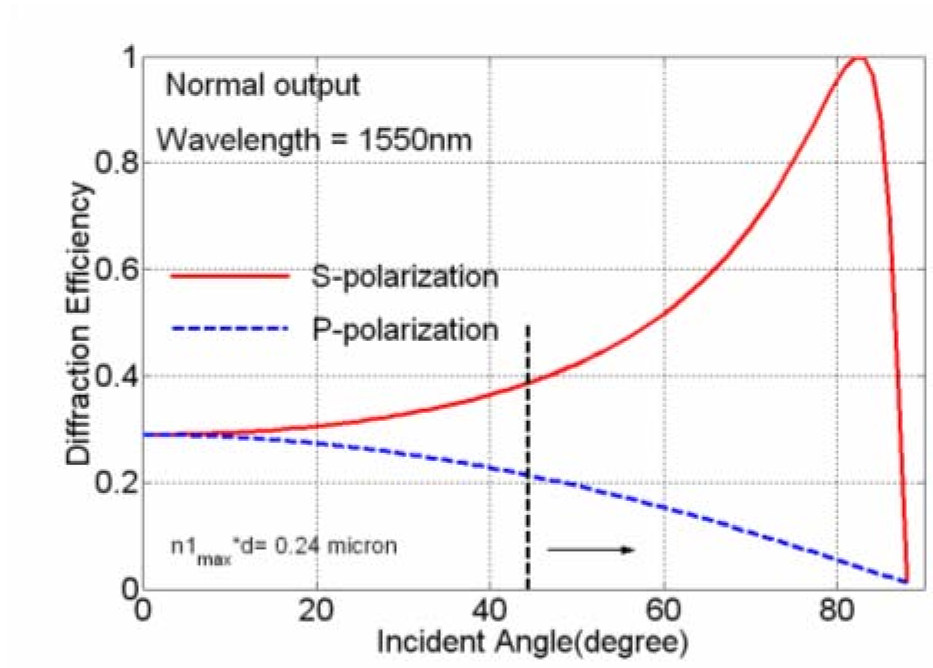

Fig. 2.2.4 Simulation of the diffraction efficiency of the volume grating with surface normal output as a function of the incident angle, for both TE(S)-wave and TM(P)-wave.

One may be curious why we design the grating incident angle at 45° rather than at any other angles. There are a few factors determining the choice of the incident angle. First, device size is always a major consideration because a small and light device is highly preferred for on-board applications. The device length (L) is calculated to be L=N*2*t*tan (θ) based on its geometry structure shown in Fig 2.2.1, where t is the thickness of the glass substrate and N is the channel number. It is obvious that the device length decreases with the incident angle. It means a small incident angle favors a smaller device size. Moreover, as can be found in Fig. 2.2.4, a small incident angle is favored to minimize the polarization dependent loss (PDL). In addition, it is shown by simulation that 3dB bandwidth of the volume holographic grating increases when designed incident angle decreases for surface normal channels. Obviously, all aforementioned considerations require a small incident angle in the design. However, this incident angle should be at least larger than total internal reflection (TIR) angle, which is 42° at the interface of air and glass, to support the guided-wave inside the glass plate. We chose 45^{o} as a balance value to reach the solution to these issues.

2.2.2 Recording parameter calculation

There are two important parameters involved in the holographic recording; one is the recording angle and the other one is the power ratio between two interfered beams. Fig. 2.2.5 shows the vector diagram of the constructive and reconstructive waves under the Bragg condition for the volume grating with a surface-normal output. For holographic gratings, both the construction and reconstruction waves satisfy the Bragg condition, which give

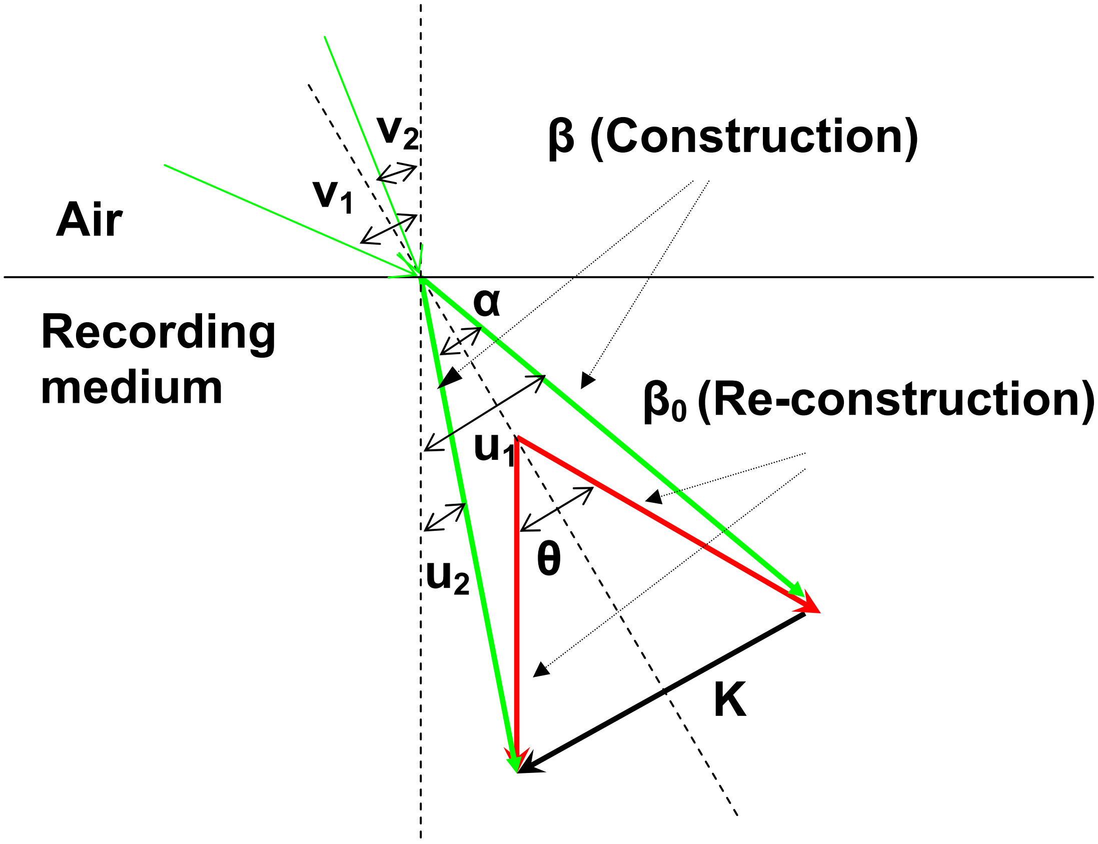

Fig. 2.2.5 Vector diagram of the constructive and reconstructive waves under the Bragg condition.

$$\beta \cdot \sin\frac{\alpha}{2} = \beta_0 \cdot \sin\frac{\theta}{2} = \frac{K}{2} = \frac{1}{2}\frac{2\pi}{\Lambda}, \qquad (2.2.1)$$

where θ is the incident angle of the reconstructive wave which is 45 °, α is the angle between two constructive waves, Λ is the period of grating constants of the constructive and reconstructive waves inside recording medium. In turn, recording angles inside and outside the recording medium of two constructive beams u_1, u_2, v_1 and v_2 can be calculated as, β and β_0 are propagation

$$u_1 = \frac{\theta}{2} + \frac{\alpha}{2}, \tag{2.2.2}$$

$$u_2 = \frac{\theta}{2} - \frac{\alpha}{2}, \tag{2.2.3}$$

$$v_1 = \sin^{-1}(n \cdot \sin(u_1)), \tag{2.2.4}$$

$$v_2 = \sin^{-1}(n \cdot \sin(u_2)), \tag{2.2.5}$$

where n is the refractive index at the wavelength of constructive of the recording medium. In our recording, the wavelength of the constructive beam is 532 nm, and its corresponding n is about 1.52. The equalized amplitude of electrical field of two interfered beams inside the recording film enables maximum light contrast between the dark and light regions of the interference pattern, which in turn enhances the efficiency of the modulation of refractive index. It is therefore important to adjust the power ratio between two interfered beams to equalize the amplitude of their electrical fields inside the recording film for. For S-polarization (E perpendicular to plane of incidence) wave, using the Snell's law and boundary conditions, we can express the ratio of the amplitude of the transmitted and incident electrical fields for two interfered waves as

$$\frac{E_1^{'}}{E_1} = \frac{2\sin u_1 \cos v_1}{\sin(u_1 + v_1)}, \tag{2.2.6}$$

$$\frac{E_2^{'}}{E_2} = \frac{2\sin u_2 \cos v_2}{\sin(u_2 + v_2)}. \tag{2.2.7}$$

To make $E_1^{'} = E_2^{'}$, we have the power ratio of the incident beam as

$$\frac{I_2}{I_1} = (\frac{E_2}{E})^2 = (\frac{2\sin u_2 \cos v_2}{\sin(u_2 + v_2)} / \frac{2\sin u_1 \cos v_1}{\sin(u_1 + v_1)})^2 . \tag{2.2.8}$$

The calculated results of the recording angle, power ratio and grating period for each CWDM channel is listed in Table 2.2.1.

	Wavelength of the reconstructive beams (nm)			
	830	1060	1340	1550
v_1 (°)	65.28	57.20	52.03	48.68
v_2 (°)	12.68	17.53	21.19	22.77
u_1 (°)	36.7	33.57	31.24	30.05
u_2 (°)	8.3	11.43	13.76	14.95
I_2/I_1 (%)	42.2	59.0	68.83	133.43
Λ (μm)	0.72	0.92	1.16	1.35

Table 2.2.1 Calculation of the recording angle, power ratio and period of volume holographic gratings.

2.3 Device fabrication and packaging

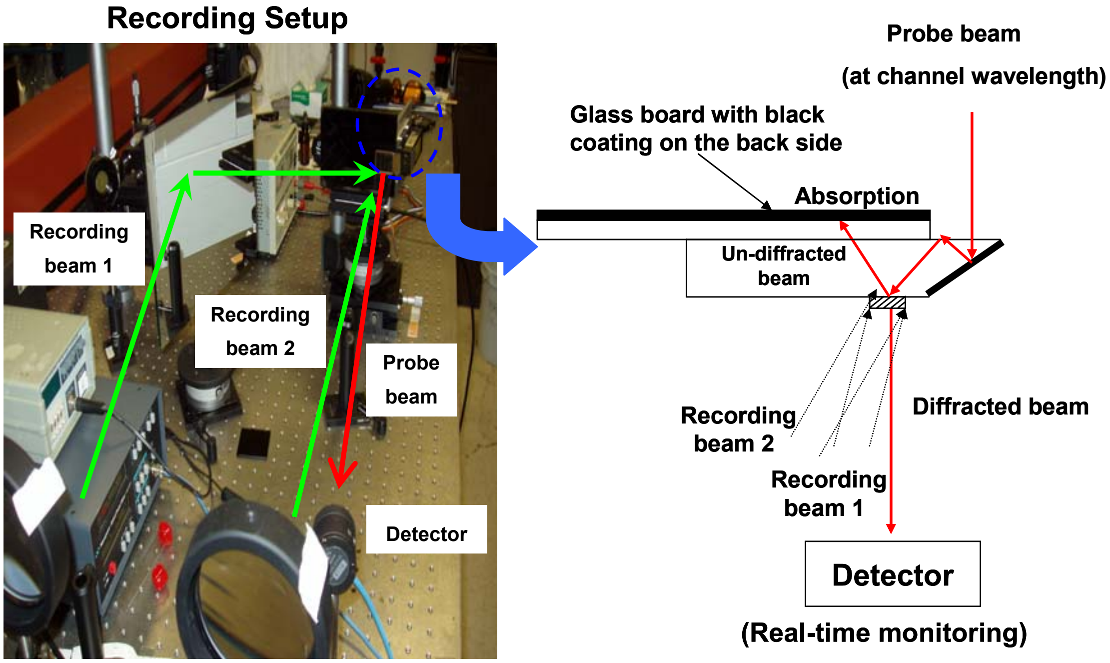

Fig. 2.3.1 The monitoring setup for hologram recording.

532nm line from a 0.5 W Verdi laser is employed in the holographic recording. We monitored the diffraction efficiency for each wavelength channel in a real-time manner during the recording. A photo-detector was used to measure the real-time diffraction efficiency of probe beams from the grating under process. Exposure time was optimized depending on the targeted diffraction efficiency for each channel. The monitoring setup is depicted in Fig. 2.3.1. PolarOnyx, Inc. packaged the five channel (one demo channel at 632nm was added) volume holographic grating based CWDM device[35]. The extra packaged losses for the packed device, shown in Fig. 2.3.2, are less than 0.4 dB.

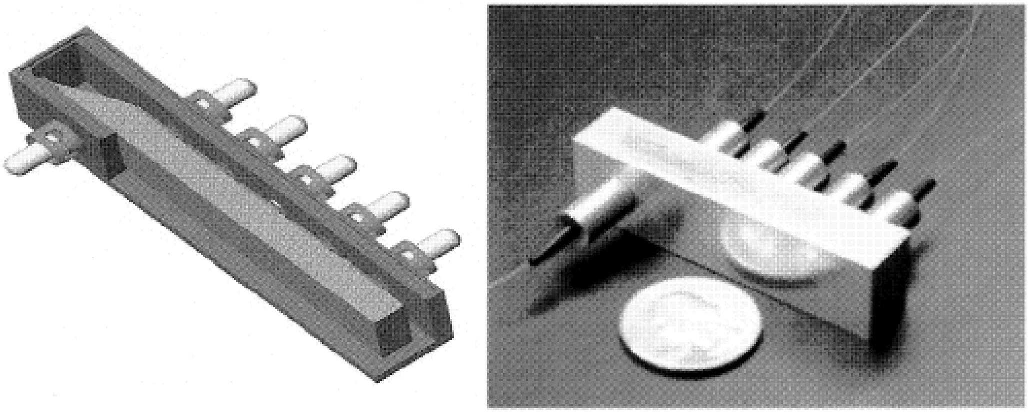

Fig. 2.3.2 A packaged polymer coarse WDM photonic interconnects (right) and its assembly drawing (left) [35].

2.4 Device Characterization

The fabricated four-channel CWDM is shown in Fig 2.2.2. The dimension of this device is 40mmX20mmX5mm. The scaling capability of this device makes it promising in space-based application where reduction in the mass and volume to be boosted into orbit is always a big concern. Fig. 2.4.1 shows an experimental demonstration of the four-channel CWDM operating at 0.83μm, 1.06μm, 1.34μm and. 1.55μm. The image is taken by an infrared camera under the randomly polarized input optical signals. A TV lens with focal length of 25mm was used to enable the responding area of camera to accommodate all the four fan outs. It is seen from Fig. 2.4.1 that four channels are completely separated while good mode qualities are maintained. Diffraction efficiency of each channel is plotted in Fig.2.4.2. This device is polarization sensitive. For TE wave, channel efficiencies at 0.83μm, 1.06μm, 1.34μm and 1.55μm are 55%, 40%, 35% and 45%, respectively. With the achievable maximum refractive index modulation of recording medium fixed, the difference in the efficiency for each channel can be simulated by couple mode theory [26]. A comparison between the experimental and theoretical simulation results indicates that the maximum index modulation of the recording medium achieved in our experiment is 0.012~0.14. For TM wave, channel efficiencies are 45%, 30%, 25%, 30%, respectively. The polarization dependence of the diffraction beam is due to the different boundary conditions between the TE and TM waves, which can be analyzed in details by the couple mode theory [26].

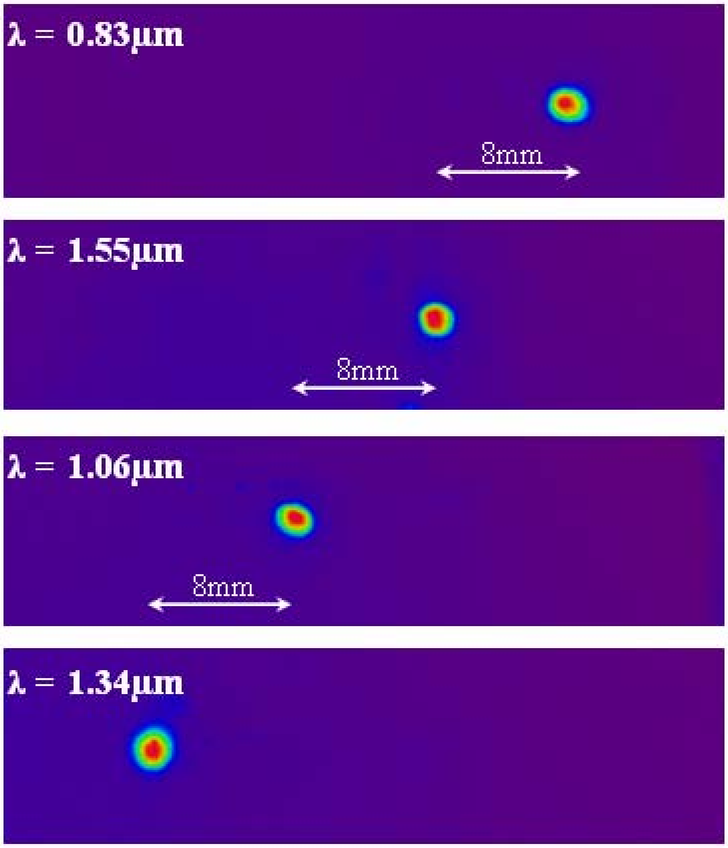

Fig. 2.4.1 IR images of the light spots for CWDM working at 0.83μm, 1.06μm, 1.34μm and. 1.55μm.

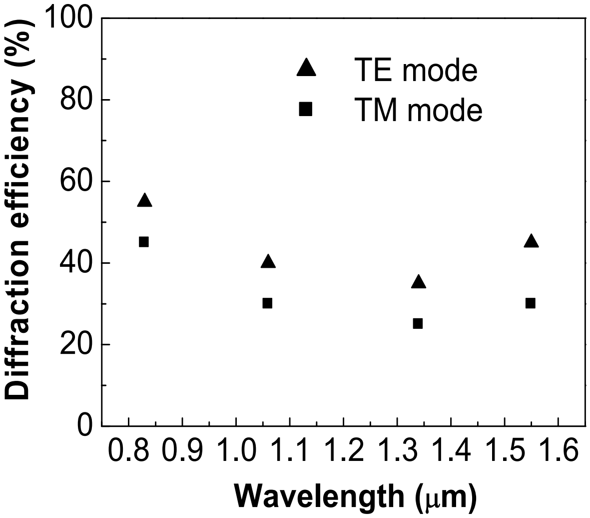

Fig. 2.4.2 Measured diffraction efficiency of each channel for both the TE and TM waves.

2.5 Summary

In this chapter, we briefly covered the coupled wave theory and the principle of volume grating formation in Dupont photopolymer. A new application of CWDM for optical inter-satellite links was introduced. A four-channel CWDM was designed and then fabricated particularly for the applications in both current medium bit rate (300Mbit s^{-1}) system based on 0.8 μm technology and future high bit rate (1.2Gbit s^{-1}) system based on 1.5 μm technology. This broad-band four-wavelength CWDM provides two data streams channels at 0.83μm and 1.55μm, one inter-satellite tracking channel at 1.06μm, and one intra-satellite communication channel at 1.34μm. A multilayer structure of holographic grating based WDM device that covers channels from 780nm to 1550nm was reported previously [34]. However, it is for the first time that a WDM device is designed and fabricated to cover such a large wavelength range in a single substrate. Surface-normal fan outs and 8mm physical separation between adjacent channels are designed to facilitate the output coupling and packaging. The features of small size and lightweight make this CWDM device quite attractive for space-borne applications due to the requirements of low weight and volume.

1-D periodic-structure-based device (II):

Holographic-grating-based twenty-one-channel dense wavelength-division-multiplexing (DWDM) device

3.1 Research motivation and design challenges

Volume holograms are a highly efficient angular dispersive element. They have been identified as an attractive solution to build wavelength-division multiplexers (WDMs) [36-38]. Volume holographic grating-based WDMs with a surface-normal configuration, which consist of a pair of transmission volume holographic gratings and a wave-guiding substrate, have been extensively investigated for their advantages of coupling and packaging [39-41]. A schematic of a conventional device configuration is shown in Fig. 3.1.1.

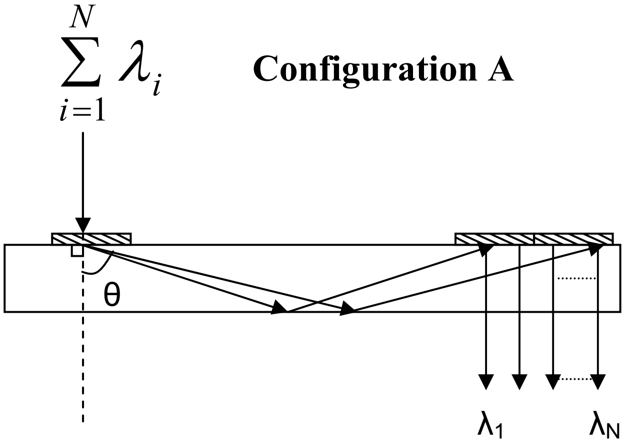

Fig. 3.1.1Schematic of a holographic-grating-based DWDM device with a conventional surface-normal configuration.

The normally-incident optical signals are collimated and diffracted into a wave-guiding substrate by an input grating with wavelength-dependent angles. These optical signals can be separated when traveling through the substrate by their wavelength-dependent bouncing angles. At the outputs, they are coupled out by another surface-normal volume grating with a predetermined lateral shift in the positions of their fan-outs. These spatially separated optical signals are later received by a detector array directly, or are coupled into a fiber bundle-array via a gradient index (GRIN) lens. For these devices, channel numbers are determined by the angular dispersion capacity, the efficiency bandwidth of the grating and the physical size of the wave-guiding substrate. Many limitations are encountered in such a design, however. The dispersion of a volume holographic grating is given as [42],

$$\frac{\Lambda}{\sin\varphi}(\sin\alpha + \sin\theta) = \frac{m\lambda}{n}, \qquad m = 0, \pm1, \pm2, \ldots, \tag{3.1.1}$$

where Λ is the grating period, φ is the grating angle, λ is the light wavelength in vacuum, n is the refractive index of the grating material, and α and θ are the incident and diffraction angles of the input signal. For the conventional surface-normal configuration shown, the diffraction angle changes with the input signal wavelength as

$$\frac{d\theta}{d\lambda} = \frac{\sin\alpha + \sin\theta}{\lambda\cos\theta}, \tag{3.1.2}$$

which can be derived from equation 3.1.1. For the surface-normal grating, the dispersion capacity is proportional to tan θ if $\alpha = 0$ or proportional to sin α if $\theta = 0$. This means the dispersion capability increases with the designed incident or diffraction angles in a surface-normal configuration. However, it is found in Fig. 3.1.2 that its 3dB efficiency bandwidth decreases with the incident or diffraction angle for both s-wave and p-wave. The intrinsic tradeoff between the dispersion capacity and the efficiency bandwidth of a volume holographic grating presents a serious hurdle in designing practical devices. A surface-normal broadband grating with a diffraction angle at 45°, which is very close to the total internal reflection angle, was designed and fabricated for the application of DWDM devices [39, 40]. Within that structure, however, multiple bounces of the signal within the substrate are required to achieve enough lateral channel separation. This is because the small angular dispersion capacity of the grating has such a small diffraction angle. The approach of multiple reflections of signal beams within a substrate will not only deteriorate the mode quality of the signals, but will also broaden the beam size which in turn increases the cross talk between adjacent channels.

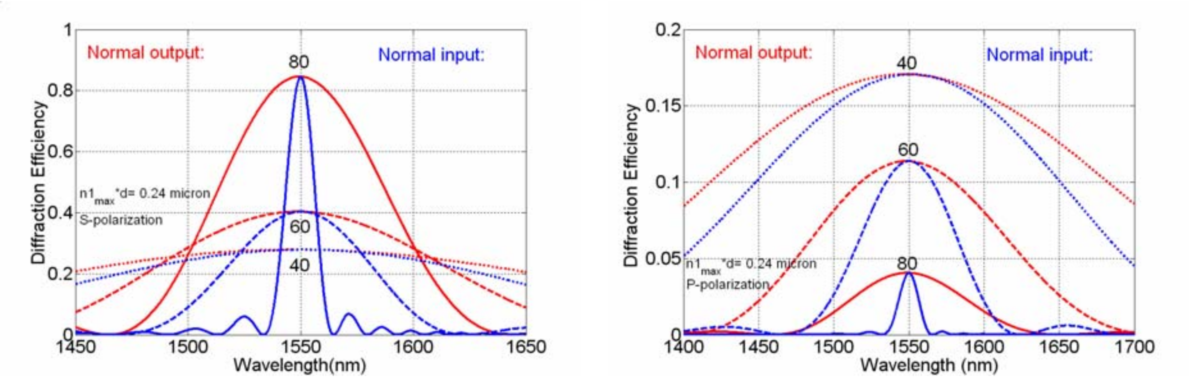

(a) (b)

Fig. 3.1.2 Simulations of the diffraction efficiency against the wavelength for both (a) S-wave; and (b) P-wave in a conventional surface-normal configuration.

3.2 Solution: innovative phase-compensation scheme

We came up with a novel scheme to overcome this intrinsic tradeoff by generating a wavelength-dependent incident angle for a dispersion-enhanced holographic grating through a pre-staged volume hologram, as illustrated in Fig. 3.2.1. The resultant effect is an enhancement of the de-multiplexing capacity of the DWDM device. The 3dB bandwidth of a dispersion-enhanced grating is broadened by 5 times. Our proposed scheme is a universal solution to the intrinsic tradeoff between the dispersion capability and the efficiency bandwidth of a volume grating. Its application can also be extended to other devices which are based on the dispersion of a volume grating, such as a true time delay module for a phase array antenna system [43].

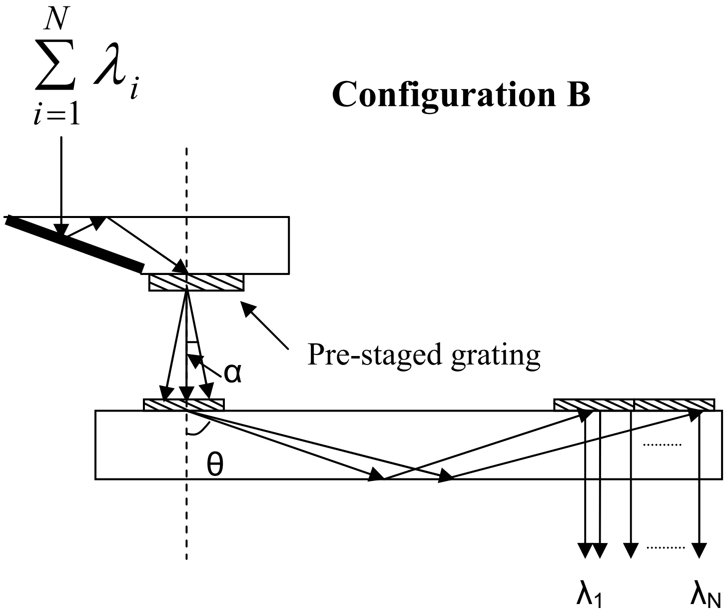

Fig. 3.2.1 Schematic of a holographic grating based DWDM device with a pre-staged volume holographic grating.

It can be derived from equation 3.1.2 that for the propagation of a one-bounce distance, the lateral shift in the position of the fan-outs is given by,

$$\frac{dL}{d\lambda} = \frac{2d \times \frac{d\theta}{d\lambda}}{(\cos\theta)^2}, \tag{3.2.1}$$

where d is the thickness of the substrate. The simulation of this lateral shift is shown in Fig. 3.2.2, where a substrate thickness of 7 mm and the center wavelength at 1555 nm are used for the calculation. The lateral dispersion capacity is very dependent on the designed diffraction angle of the grating. The larger the diffraction angle, the bigger the dispersion capacity will be. For the conventional configuration A, the lateral dispersion increases from 0.42 mm/nm to 3.31 mm/nm when the designed diffraction

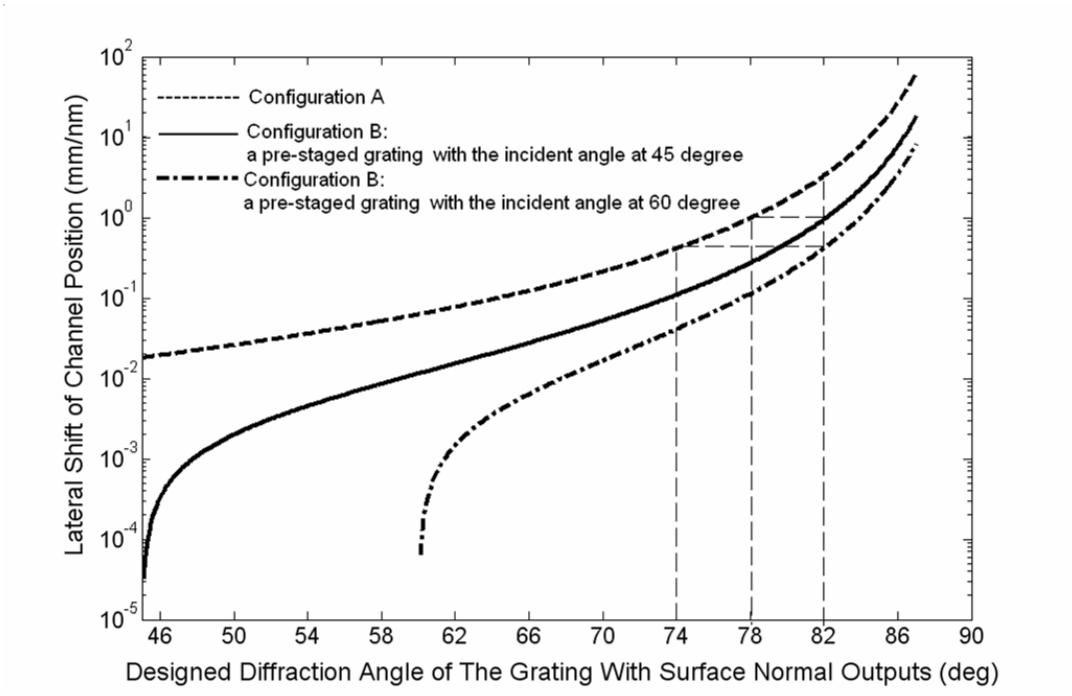

Fig. 3.2.2 Lateral shift of the channel position as a function of the designed diffraction angle of a surface normal volume grating.

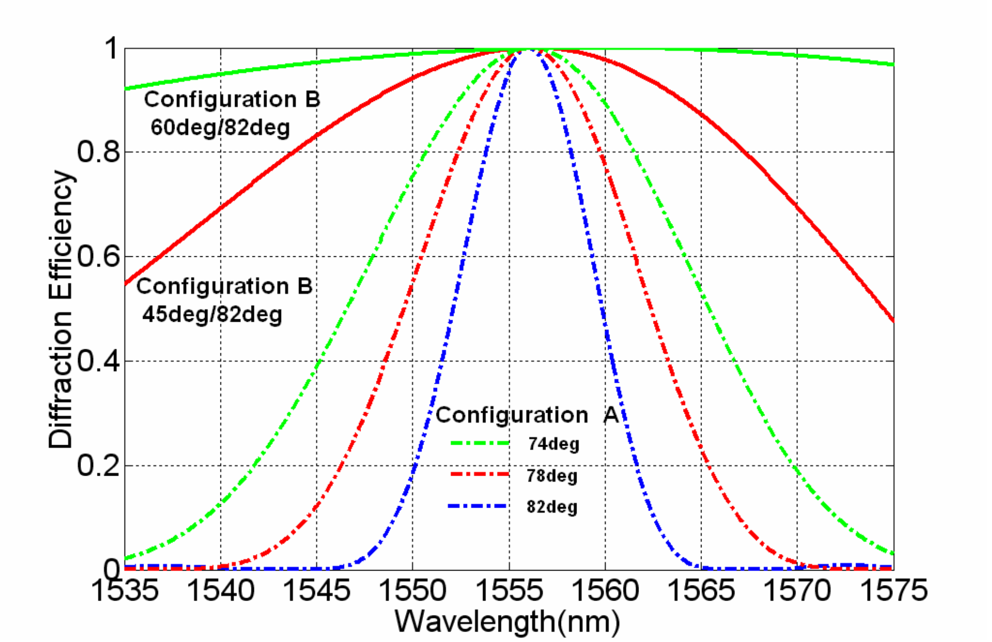

Fig. 3.2.3 Diffraction efficiency as a function of wavelength for both configuration A and B.

angle changes from 74^o to 82^o. Obviously, the dispersion capacity can be enhanced by increasing the designed diffraction angle of the grating. The diffraction efficiency bandwidth of a transmission volume hologram can be simulated by using coupled wave theory [26]. Simulation results of the diffraction efficiency as a function of wavelength for both configuration A and B are shown in Fig. 3.2.3. It is clearly seen that the grating pass-band decreases with diffraction angle. For an 82^o grating, the 3dB bandwidth only covers 8 nm centered at 1555 nm. However, for a 74^o grating, the 3dB bandwidth increases to 19 nm. The tradeoff between the dispersion capacity and the efficiency bandwidth presents a huge challenge to the design of a volume grating-based DWDM device. The advantage of combining two discrete volume holograms in $45^o/82^o$ or $60^o/82^o$ configurations is clearly indicated in Fig. 3.2.3. To achieve a broad efficiency bandwidth of a dispersion-enhanced volume grating, the incident angle of the input signal must be changed from α_o to $\alpha_o + \Delta\alpha$ when the input wavelength changes from λ_0 to $\lambda_0 + \Delta\lambda$. This phase compensation condition can be derived from Bragg Condition [26]. Mathematically, it is represented as

$$\frac{d\alpha}{d\lambda} = \frac{1}{2\Lambda n\cos(\frac{\alpha+\theta}{2})} = \frac{\tan(\frac{\alpha+\theta}{2})}{\lambda_o}. \qquad (3.2.2)$$

The phase compensation for a dispersion-enhanced grating with a large diffraction angle can be achieved by using a pre-staged grating. As shown by the configuration B in Fig. 3.2.1., an aluminum-coated beveled edge is used to change the direction of a normally-incident signal to a specific incident angle for the pre-staged grating. The signal at the Bragg wavelength of the pre-staged grating is designed to be coupled out surface-normally. The angular dispersion of this pre-staged grating provides a wavelength-dependent incident angle to the cascaded dispersion-enhanced grating which is required to achieve phase compensation. Perfect phase compensation can be achieved only when $\left|\frac{d\theta_1}{d\lambda}\right| = \left|\frac{d\alpha_2}{d\lambda}\right|$, where θ_1 is the designed diffraction angle of the pre-staged grating and α_2 is the designed incident angle of the cascaded dispersion-enhanced grating. For a dispersion-enhanced grating which has a surface-normal input and a designed diffraction angle of 82°, a perfect phase-compensation can be provided by a pre-staged grating which has an incident angle of 60.4° and a surface-normal output. Similarly, the phase mismatch can be partially compensated by a pre-staged grating which has a designed incident angle smaller than 60.4°, namely, $\left|\frac{d\theta_1}{d\lambda}\right| < \left|\frac{d\alpha_2}{d\lambda}\right|$. Both simulations have confirmed the bandwidth broadening of the dispersion-enhanced grating, which is attributed to this phase compensation scheme. In Fig. 3.2.3, simulations show the efficiency curve can be flattened significantly by using a $60.4^{\circ}/82^{\circ}$ configuration. If a 45° pre-staged grating is used, the 3dB bandwidth of configuration B increases up to 40 nm compared with 8nm of configuration A (without the pre-staged grating). However, one side effect occurs for configuration B. The configuration with phase compensation reduces the dispersion capacity of the original dispersion-enhanced grating. The lateral channel separation for configuration B can be derived from equation 3.1.1 and 3.1.2. The simulation results are shown in Fig. 3.2.2. Compared with the original dispersion-enhanced grating at 82° in configuration A, the lateral channel shift decreases from 3.30 mm/nm to 0.95 mm/nm and 0.42 mm/nm for configuration B with pre-staged grating angles at 45° and 60.4°, respectively. However, their lateral dispersion capacities are still large, which are comparable to the original dispersion-enhanced grating with diffraction angles at 78° and 74°, where their original 3dB bandwidths are only 13 nm and 19 nm, respectively. By using our $45^{\circ}/82^{\circ}$ and $60.4^{\circ}/82^{\circ}$ configurations, much broader bandwidths are achieved while the high dispersion capacity of the grating is still maintained. The calculation results are summarized in table 3.2.1 for the purpose of comparison. To resolve 200 GHz (~1.6 nm) DWDM channels with low cross talk, the $45^{\circ}/82^{\circ}$ configuration is chosen for our DWDM device considering both the efficiency bandwidth and the dispersion capacity. Its 3dB bandwidth, which is shown in Fig. 3.2.3, covers wavelength from 1535 nm to 1575 nm.

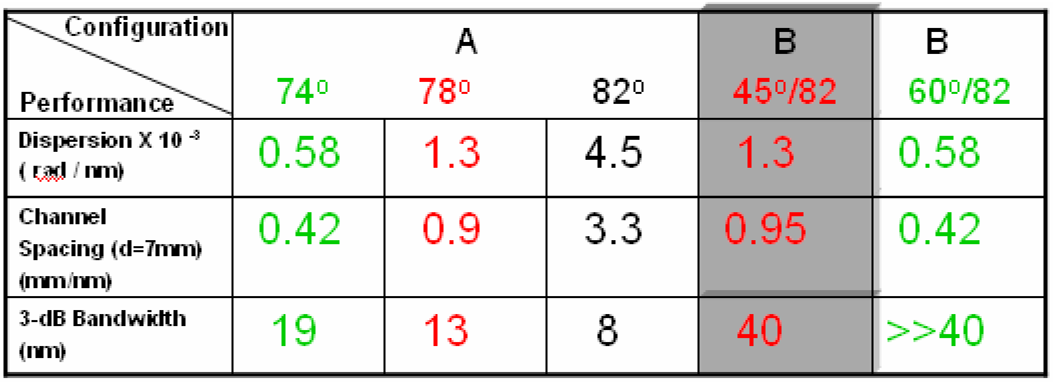

Configuration / Performance	A			B	B
	74^0	78^0	82^0	$45^0/82$	$60^0/82$
Dispersion X 10^{-3} (rad / nm)	0.58	1.3	4.5	1.3	0.58
Channel Spacing (d=7mm) (mm/nm)	0.42	0.9	3.3	0.95	0.42
3-dB Bandwidth (nm)	19	13	8	40	>>40

Table 3.2.1 Comparison of dispersion and 3-dB bandwidth of various device structures.

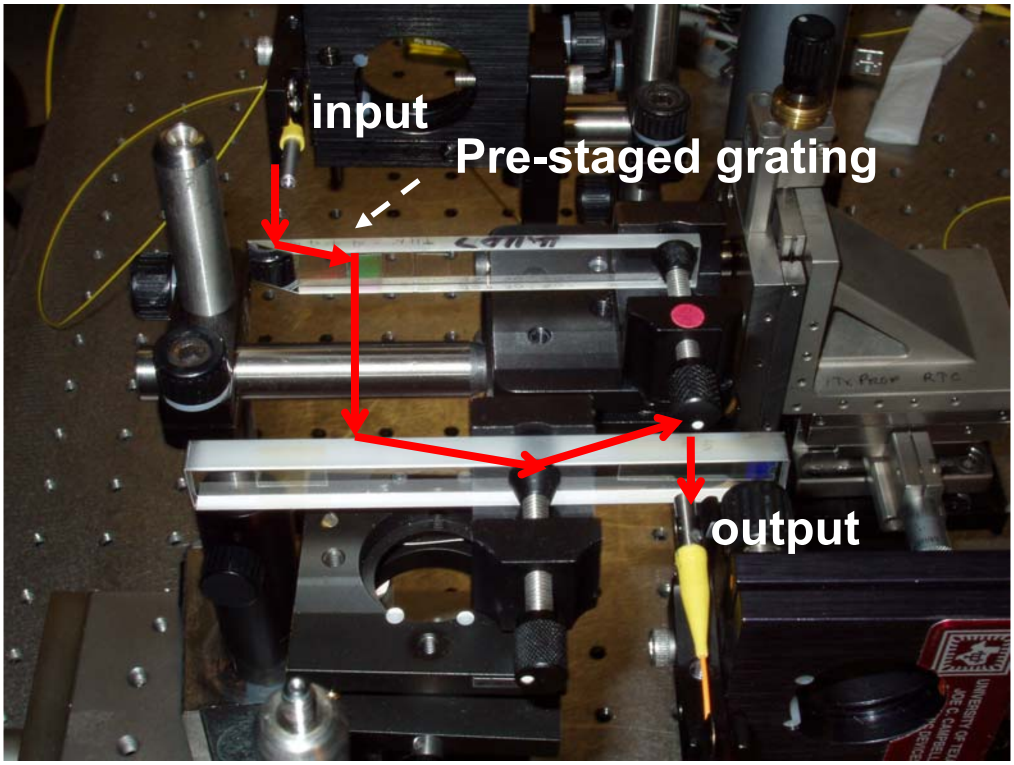

Fig. 3.3.1 Photograph of the developed holographic-grating based DWDM device.

3.3 Device fabrication

The 532 nm line from a 0.5 W Verdi laser was employed in the holographic recording. We used a prism coupler to couple the recording laser beam into the photopolymer film under the phase matching condition because the slanted angle of the second-stage grating is very large and requires recording angles larger than the total internal refraction angle. The developed DWDM device is shown in Fig. 3.3.1.

3.4 Device characterization

The pre-staged grating was recorded and characterized as shown in Fig. 3.4.1, for

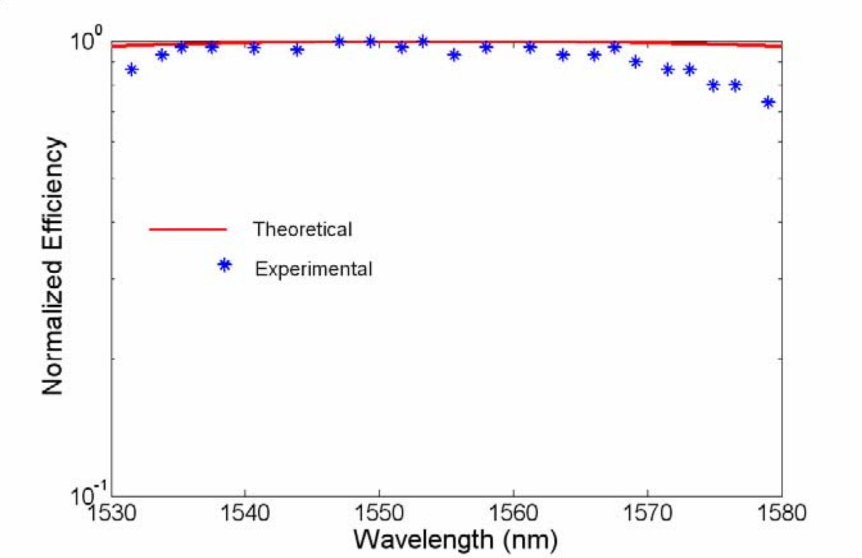

Fig. 3.4.1 Theoretical calculation and experimental characterization of the diffraction efficiency versus wavelength for the pre-staged 45° grating.

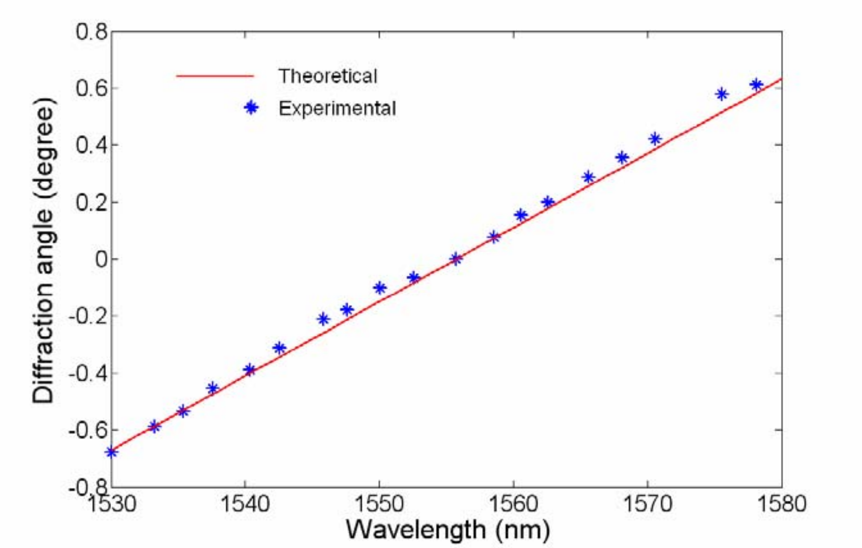

Fig. 3.4.2 Wavelength-dependent deviation angles from the pre-staged 45° grating.

the 45° pre-staged grating, less than a 0.2dB reduction in the channel efficiency from 1535 nm to 1575 nm, with respect to the peak efficiency at 1555 nm, is experimentally confirmed. The measurement results of the wavelength-dependent output angles of the pre-stage grating are quite consistent with the theoretical predictions. All of the optical signals are coupled out and incident to the next stage grating with fairly uniform intensities. We also measured the wavelength-dependent deviation angles from the pre-staged grating. It is shown in Fig 3.4.2 that the maximum deviation angle with respect to the surface-normal direction is measured to be $\pm 0.52^{o}$ for channels at 1535 nm and 1575 nm, which perfectly matched the theoretical calculation. The channel efficiencies of the TE mode beam for both configuration A and configuration B were measured and plotted in Fig. 3.4.3. The experimental data and theoretical predictions are in good agreement. The output spectra for both configurations are measured by an optical spectrum analyzer. As shown in Fig. 3.4.4., our device covers 21 channels

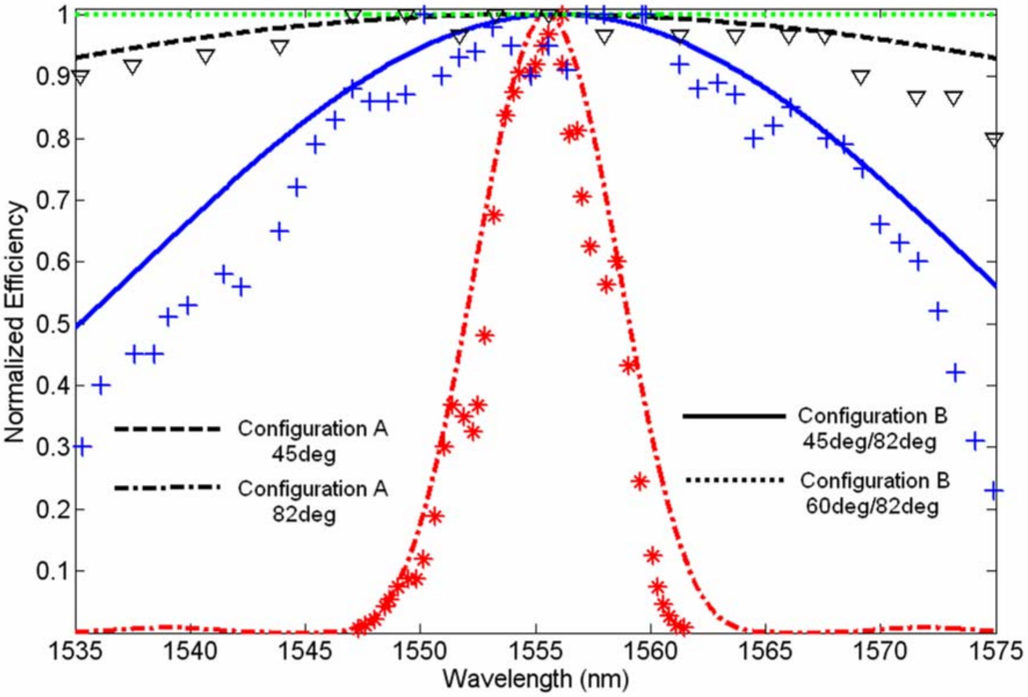

Fig. 3.4.3 Simulations and experimental results of the diffraction efficiency of the surface normal volume grating in configuration A and configuration B.

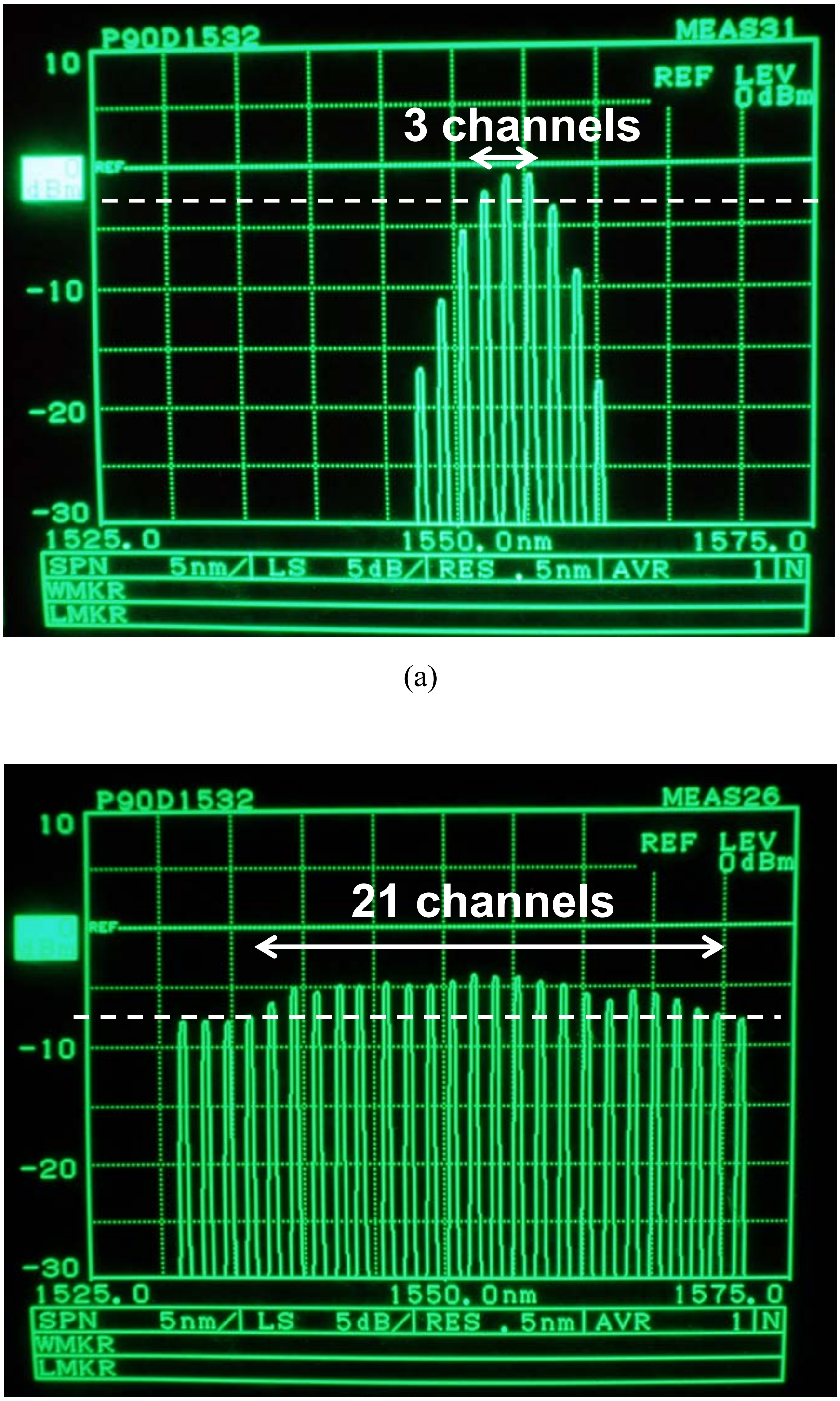

(a)

(b)

Fig. 3.4.4 Output spectra measured by an optical spectrum analyzer. (a) Configuration A: dispersion enhanced grating using a diffraction angle at 82°, (b) Configuration B: the 45° /82° configuration.

with 200 GHz spacing within the 3dB bandwidth while the conventional configuration can only accommodate 3 channels with the same spacing. More than 40 channels with 100 GHz spacing can be achieved by this DWDM device as long as the incident signals are well collimated to have a spot size smaller than 500 μm at the output. Our device has a peak efficiency of 40% and a large polarization dependent loss (PDL). This is mainly due to the relatively low refractive index modulation (0.012) that we can achieve with Dupont photopolymer. However, simulations show that a peak efficiency of 95% and the PDL less than 0.4dB can be achieved by our proposed structure as long as the refractive index modulation can reach 0.15 for a given photopolymer thickness of 20 μm. This index modulation can easily be achieved in dichromated gelatin (DCG) [44].

3.5 Summary

In this chapter, we reported a universal solution to solve the intrinsic tradeoff between the dispersion capacity and the efficiency bandwidth of a volume holographic grating. By using a pre-staged grating in front of a dispersion-enhanced grating, a huge enhancement of the 3dB efficiency bandwidth can be achieved due to the phase compensation of the Bragg Condition. In this work, the phase-compensation scheme is demonstrated by using the $45^o/82^o$ configuration. A 21-channel DWDM device centered at 1555 nm with 200 GHz spacing is achieved within a 3dB bandwidth. All results were measured with a TE mode.

Chapter 4

1-D periodic-structure-based device (III): Liquid-crystal-based high-resolution switchable Raman-Nath grating

4.1 Introduction

4.1.1 Liquid crystal and Liquid crystal cell

Liquid crystal (LC) is an intermediate state of matter between a crystalline solid and an amorphous liquid. It can be thought of as a liquid in which an ordered arrangement of molecules exists. The molecules composing such material are sharply anisotropic. They can be visualized as ellipsoids, with a single long axis about which there is circular symmetry in any transverse plane. These molecules can stack next to one another in various ways, with different geometrical configurations defining different general types of LCs. Adjacent molecules are not rigidly bound to one another, and they can rotate or slide with respect to one another under the application of mechanical or electrical forces, thus exhibiting some of the properties of a liquid. However, there are constraints on the geometrical organization of collections of molecules, and these constraints introduce some properties normally associated with solids.

Three classes of liquid crystal are of particular interest in optics. They are nematic, smectic, and cholesteric. They are are classified by the different molecular orders or organizational constraints. I restrict my introduction of the material properties to only the nematic LCs because my research on LC gratings is based on this type of LC. For nematic LCs, the molecules throughout the entire volume of the material favor a parallel orientation, with random located centers within that volume. A LC cell usually consists of two glass plates, coated with transparent conductive layers (indium tin oxide films) and thin alignment layers (often polyimide). It is possible to impose boundary conditions on the alignment of nematic liquid crystal molecules contained between two glass plates by polishing soft alignment layers coated on those plates with strokes in the desired alignment direction. The small scratches associated with the polishing operation establish a preferred direction of alignment for the molecules that are in contact with the plate, with their long direction of alignment with the scratches. The application of an electric field across two glass plates can induce an electric dipole in each liquid crystal molecule, and can interact with any permanent electric dipoles that may be present. If, as is usually the case, the dielectric constant of a molecule is larger in the direction of long axis of the molecule than normal to that axis, the induced dipoles have charges at opposite ends of the long direction of the molecule. Under the influence of the applied fields, the torques exerted on these dipoles can cause the liquid crystal molecules to change their natural spatial orientation.

Since nematic LCs do not have the extra constraints of smectic and cholesteric materials, a sufficiently large applied voltage will cause molecules that are not in close proximity to the alignment layer to rotate freely and to align their long axes with the applied field. Thus the arrangement of the molecules within the nematic LC cell will change under sufficient applied filed to the arrangement, in which the vast majority of the molecules have their long axis aligned with the field, i.e., pointing in a direction normal to the glass plates. The change in the orientation of the molecules also changes the optical properties of the cell. To avoid permanent chemical changes to the nematic LC material, cells of this type are driven by AC voltage, typically with frequencies in the range of 1 KHz to 10 KHz and with voltages of the order of 5 volts. Note that because the dipole moment of a nematic liquid crystal is an induced moment rather than a permanent moment, the direction of the moment reserves when the applied field reverse in polarity. Thus the direction of the torque exerted by the field on the molecules is independent of the polarity of the applied voltage, and they align in the same direction with respect to the applied field, regardless of polarity.

4.1.2 Research motivation and challenges

Programmable liquid-crystal (LC) based gratings have been reported for a variety of applications including projection displays, beam steering, beam slitting, beam filtering, optical switching and interconnects [45-49]. Binary LC phase gratings were extensively studied for their great capability in beam deflecting as well as their compactness and low cost fabrication [49-54]. Current efforts have been focused on high-resolution (grating pitch size is comparable to LC cell thickness), two-level and multilevel LC gratings due to their great potentials for achieving more switching ports in the optical network and larger beam deflection tuning ranges. Investigations of the fringing-field effect, which severely degrades the phase modulation depth of the high-resolution LC grating, were solution has yet been found.

The developed binary LC phase gratings are classified into three categories. The simplest and most widely used one consists of a continuous ground plane or a dielectric reported by a few groups [47, 50, 55, 56]. However, to our knowledge no efficient layer, a sandwiched nematic LC layer, and a counter-plane which is periodically patterned with striped electrodes [45, 50, 51]. Fig. 4.1.1 (a) and (b) illustrates two basic device structures a sandwiched nematic LC layer, and a counter-plane which is periodically patterned with striped electrodes [45, 50, 51]. Fig. 4.1.1 (a) and (b) illustrates two basic device structures in this category. As shown In Fig. 4.1.1(a), homogenous (or planar) alignment is employed in a LC cell where the biasing voltage is applied between the ground plane and

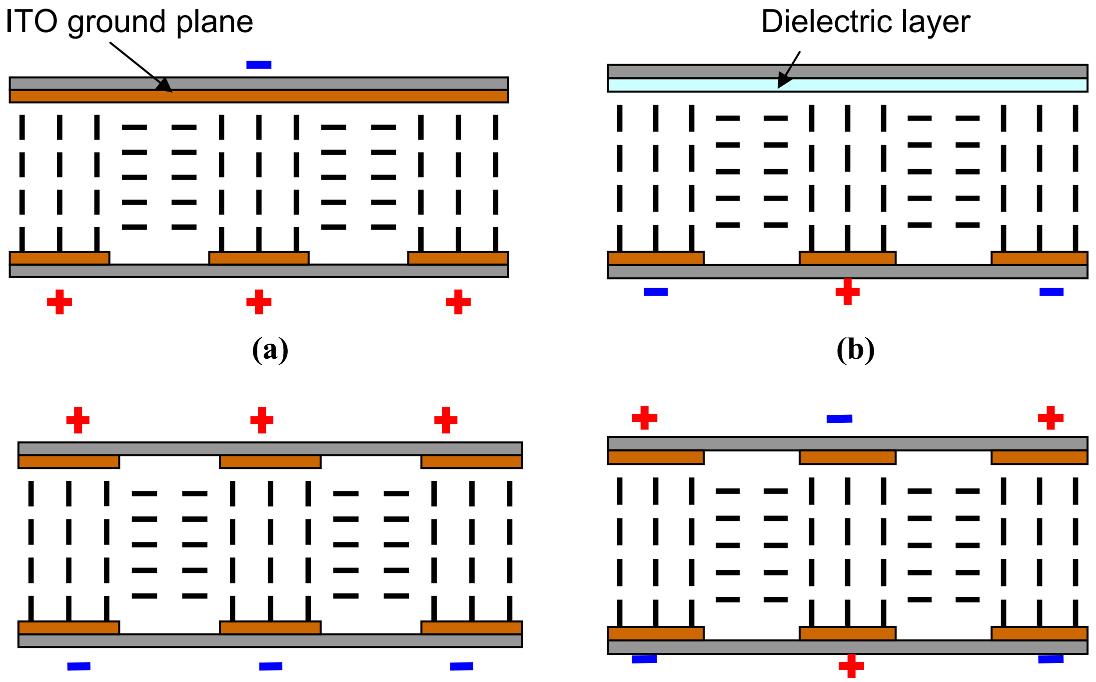

(a) **(b)**

Biasing Configuration A
(c)

Biasing Configuration B
(d)

Fig. 4.1.1 Schematics of LC phase gratings:(a) Conventional single-sided structure topped with a ITO ground plane, (b) Conventional single-sided structure topped with a dielectric layer, (c) Novel double-sided structure in the biasing configuration A, (d) Novel double-sided structure in the biasing configuration B.

striped electrodes. The LC layer is initially aligned such that the director axis lies either entirely perpendicular or parallel to the direction of the grating vector, depending on the polarization status of the incoming beam. When the voltage is applied, vertical electric fields are generated. These fields are strong in the central regions above the striped electrodes, but weak in the lateral regions between adjacent electrodes. Ideally, the LC molecules in the central regions tend to align themselves along the field lines while those in the lateral regions are little disturbed and remain with their initial orientation. Thus, a binary spatial phase modulation is created for the incident light that is polarized in a specific direction. However, in reality, the phase modulation departs from a binary profile due to the fringing fields from the edges of the striped electrodes. These fringing fields extend into the lateral region and deform the LC director axis, which makes the resulting phase profile mostly sinusoidal. Especially in high-resolution LC gratings, where the pixel spacing is small, the overlap of the fringing fields from the adjacent openings significantly reduces the modulation capacity and thus limits the diffraction efficiency of the device.

A method to increase the resolution was reported where an interdigitated structure, utilizing lateral (fringing) fields rather than transverse (vertical) fields were used to align LC.[51, 57]. As is shown in Fig. 4.1.1 (b), LC is initially treated with a homeotropic (or vertical) alignment and the biasing voltage is applied between adjacent striped electrodes instead of between the counter-electrical planes. Fringing fields are actually used to reorient the LC director along the field lines. The LC director in the central region above the striped electrode is expected to maintain its original direction, provided the electrode is relatively wide and the electric field is weak. However, when the grating period and the electrode width reduce, the LC director profile is deformed in an unfavorable way. In addition, the electric field in the lateral region is not usually strong enough to completely penetrate the LC layer. Therefore, the modulation capacity of this device is still insufficient to achieve high device efficiency because the effective modulation layer in such a device is much thinner than the actual thickness of the LC cell. This is particularly true for long working wavelengths in the near-infrared (IR) and IR regions. From the above discussion, it can be concluded that the devices structures shown in Fig. 4.1.1 (a) and (b) are inefficient to implement high-spatial-frequency LC gratings.

Efforts have been made to solve this problem by developing the second and the third type of binary LC gratings [46, 52, 54]. For the second type of LC phase gratings, index matching polymer grooves are used to isolate the LC regions and define the grating period. However, unlike the first type grating that can be programmed to scan the beam deflection angle, the deflection angle of this type of device is fixed. It can only provide on or off operations of diffraction at a given angle depending on the pitch size of the polymer groove. The third type of LC phase grating is usually constructed by using dual-alignment techniques. The alignment layer is patterned and the adjacent LC domains are initially aligned perpendicular to each other. When the device is in the off state, both TE and TM waves get diffracted because both experience the index modulation. When the device is in the on state, the vertical electric fields reorient the LC director uniformly along the field lines. The diffracted beams are completely extinguished because the previously existed phase modulation disappears. The same problem associated with this type of LC grating is that it is un-programmable. An even more serious problem occurs when it is developed for high-spatial-frequency applications. There is always an unavoidable twist deformation between the adjacent LC domains. This ‘twisted wall’ is usually thick and limits the spatial resolution of the grating. It turns out that none of these three major types of binary LC phase grating can function as a reconfigurable beam deflector that has a large tuning angle and sufficient diffraction efficiency. When the beam deflector works at a long wavelength such as wavelengths in the near infrared (IR) and the IR regions, the high diffraction efficiency is even harder to achieve due to the insufficient phase modulation depth, which is inversely proportional to the wavelength.

4.2 Device modeling

We have proposed a double-sided device structure to solve effectively the problem of the low phase modulation depth in high-resolution LC gratings working at 1.55 μm. The schematics of the proposed device configurations are shown in Fig. 4.1.1 (c) and (d). Unlike the conventional structure, where the electrodes are patterned only on one side of the device, our structure has electrode pixels patterned on both the top and bottom sides. By using biasing configuration (A), shown in Fig. 4.1.1 (c) , where all of the pixels on the top side are grounded while all of those on the bottom side are applied by the same voltage, a smaller lateral leakage of the electric fields between adjacent pixels is expected since the transverse fields are more confined between the opposite discrete electrodes. Further improvement can be achieved by using biasing configuration (B), shown in Fig. 4.1.1 (d), where the biasing voltages are applied between the adjacent electrodes lying in the same plane and applied between the facing electrodes in the opposite plane. This biasing scheme simultaneously develops a lateral electric field between adjacent electrodes and a vertical electric field between opposite electrodes. The lateral fields and the transverse fields minimize the distortion of the LC director profile. The lateral fields help maintain the initial alignment of the LC director in the horizontal direction between adjacent pixels and the transverse fields force the LC director above the pixels to align vertically. It is confirmed both theoretically and experimentally that this scheme provides an efficient solution to the fringing-field effects in high-resolution LC gratings. With each grating pixel dynamically addressed by a multi-channel electric switch, an efficient beam steering device with large scanning angles can be achieved using the device configuration presented here.

We used a simulation tool called LCD Master (Shintech Ltd., Japan) to simulate the LC director profile of the devices. This simulator has been shown to be accurate in simulating the LC phase gratings under two-dimensional electric fields [45, 50, 58, 59]. A finite-element algorithm is used in the program to calculate the director distribution through minimizing the LC free energy in the Frank-Oseen model [60]. The free energy (elastic energy) can be written as a quadratic function of the curvature strain tensor, which can be written

$$F = \frac{1}{2}k_{11}(\nabla \cdot \vec{n})^2 + \frac{1}{2}k_{22}(\vec{n} \cdot \nabla \times \vec{n})^2 + \frac{1}{2}k_{33}(\vec{n} \times \nabla \times \vec{n})^2 \quad . \tag{4.2.1}$$

Equation of motion of the director is given by

$$\gamma \frac{\partial n_i}{\partial t} = \frac{d}{dx_j}\left(\frac{\partial F}{\partial n_{i,j}}\right) - \frac{\partial F}{\partial n_i} + \alpha n_{i,} \tag{4.2.2}$$

, where $k_{11,}$ $k_{22,}$ and k_{33} are the splay, twist, and bend elastic constants, respectively. $\vec{\mathrm{n}}$ is an unit vector that represent the orientation of the LC molecule. We used a three-layer structure consisting of top electrodes, LC layer, and bottom electrodes for the simulation. The input parameters for simulating the LC material E7 (Merck) include elastic constants of $k_{11} = 11.1$ pN, $k_{22} = 17.1$ pN, $k_{33} = 9$ pN; dielectric constants of $\varepsilon_s = 19.0$, $\varepsilon_p = 5.2$; and viscosity of $\gamma = 0.038$ Pas. A few assumptions were taken in the calculation: (1) strong anchoring at the substrate surfaces; (2) pre-tilt angle at 3^o, twist angle at 0^o; (3) periodic boundary.

Phase modulation profiles for a normally-incident TE wave (p-wave) under various biasing conditions are obtained by using the simulated unit vector $\vec{n}(z)$ distribution of the LC director. The x component and y component of $\vec{n}(z)$ equals sin θ(z) and cos θ(z), where θ(z) is the angle between the propagation direction (z direction) and the director direction $\vec{n}(z)$. The effective index experienced by the TE wave, the phase modulation profile along the grating direction, and the phase modulation depth are given by

$$n_{eff}(\theta) = \frac{n_e \cdot n_o}{({n_o}^2 \sin^2\theta + {n_e}^2 \cos^2\theta)^{1/2}}, \tag{4.2.3}$$

$$\phi(x) = \frac{2\pi}{\lambda}\int_0^d n_{eff}(z)dz \quad , \tag{4.2.4}$$

$$\Delta\phi = \phi(x)_{\max} - \phi(x)_{\min}, \tag{4.2.5}$$

where n_e and n_o are extraordinary and ordinary refractive indices of the LC material, and d is the thickness of the LC layer.

A thin phase-grating analysis is performed to simulate the far field diffraction pattern by using fast-Fourier-transfer (FFT) algorithm [14]. The director profiles for the conventional single-sided structure (shown in Fig. 4.1.1 (a)) and the novel double-sided structure in the biasing configuration A and B (shown in Fig. 4.1.1 (c) and (d)) were simulated. High-resolution LC gratings with a pitch size p_0=6 μm, electrode width of 3 μm and LC thickness of both 5 μm and 8 μm were simulated in this work. For each structure, simulations were performed under various biasing voltages varying from 1V to 10V. Some examples of the director profiles and phase modulation profiles of the 5-μm-thick LC grating are shown in Fig.4.2.1 and Fig.4.2.2, respectively. Fig. 4.2.1 (a) shows the director profiles for a conventional single-sided structure, illustrated in Fig. 4.1.1(a),

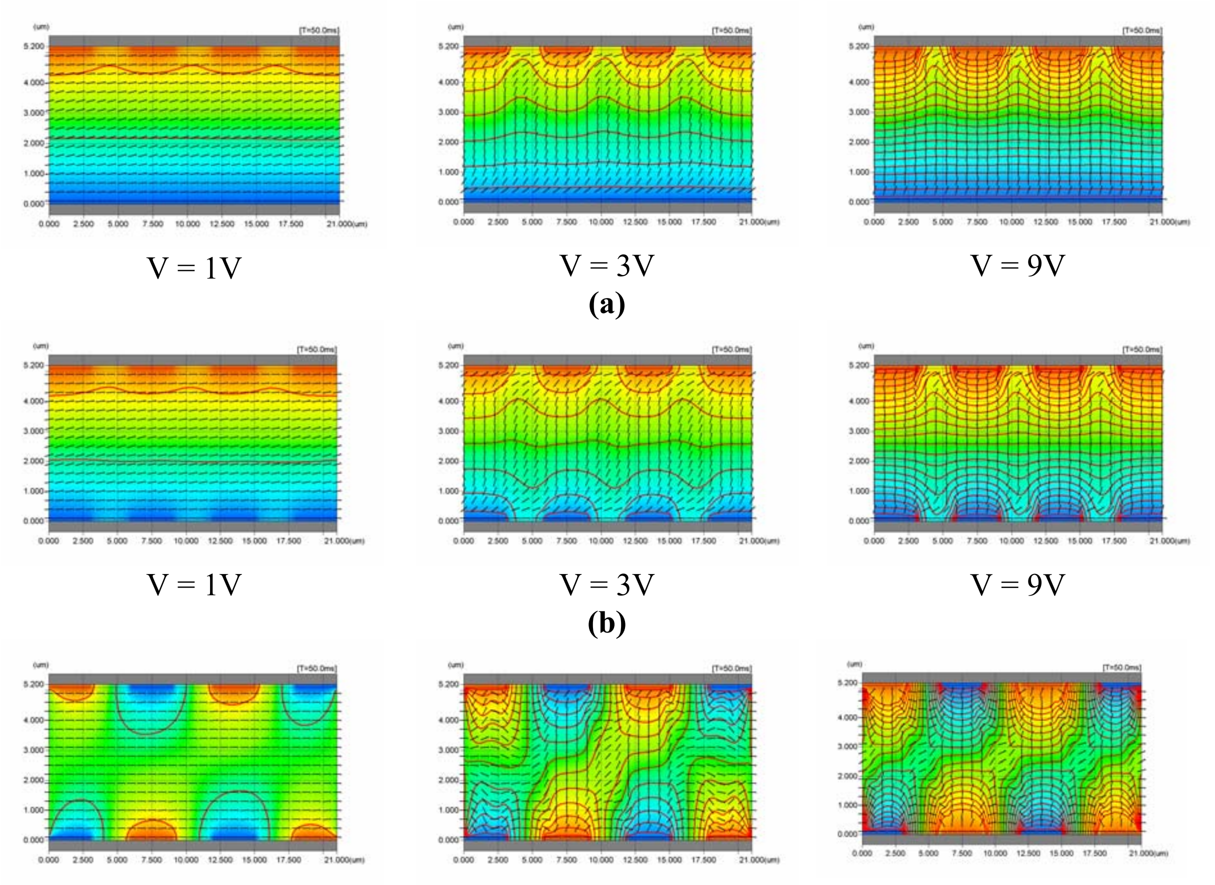
V = 1V V = 3V V = 9V

(a)

V = 1V V = 3V V = 9V

(b)

V = 1V V = 5V V = 9V

(c)

Fig. 4.2.1 LC director profiles under different biasing voltages for (a) Conventional single-sided structure, (b) novel double-sided structure in the biasing configuration A, (c) novel double-sided structure in the biasing configuration B.

under basing voltages at 1V, 3V and 9V. When the applied voltage is very low, the electric filed is not strong enough to switch on the LC director. As the voltage increases, LC molecules in the central regions between the facing electrodes begin to rotate towards the direction of the electric field. As expected, the LC director in the lateral region is deformed undesirably by the fringing fields, which reduces the available phase modulation depth. The situation is even worse when the voltage increases continuously. Fringing fields become so strong that most of the directors in the lateral region are

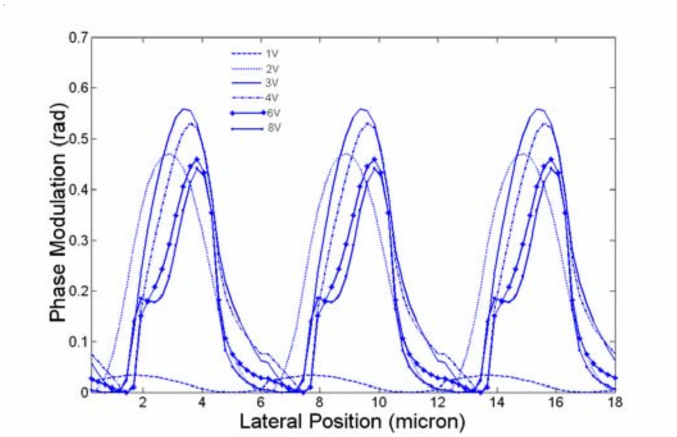

(a)

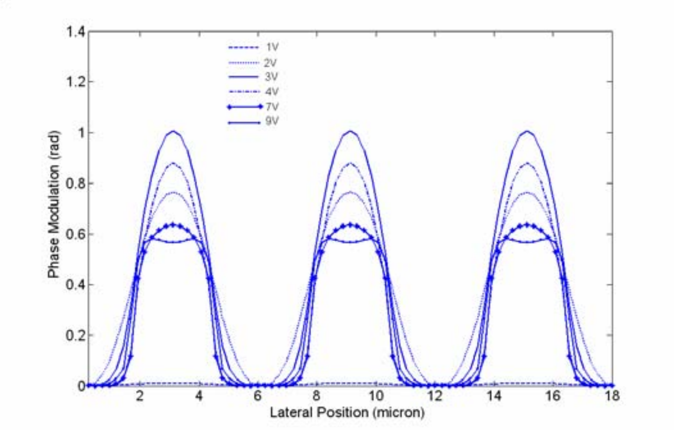

(b)

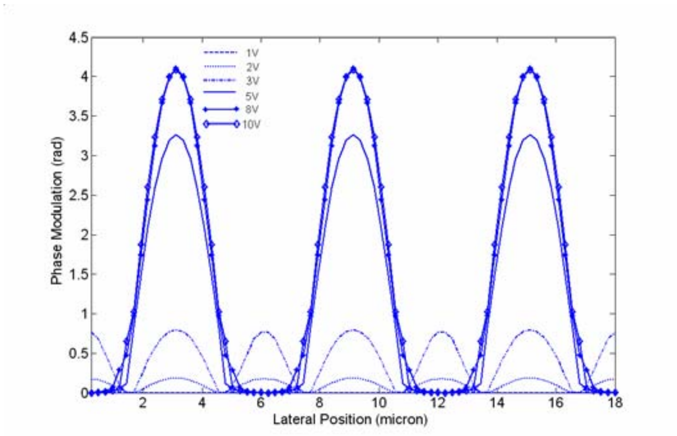

(c)

Fig. 4.2.2 Phase modulations for normally incident light at 1.55μm (TE) through LC phase gratings under different biasing voltages: (a) single-sided structure, (b) double-sided structure in the biasing configuration A, (c) double-sided structure in the biasing configuration B.

oriented vertically. In this case the phase modulation depth is further reduced.

The improvements for the fringing- field effect in our double-sided structure are shown in Fig. 4.2.1 (b) and (c). Some examples of the phase modulation for both structures are shown in Fig. 4.2.2. It is evident that our double-sided structure can achieve much larger phase modulation depth than the single-sided structure. As seen in Fig. 4.2.2, the phase modulation for these high-spatial frequency gratings departs from

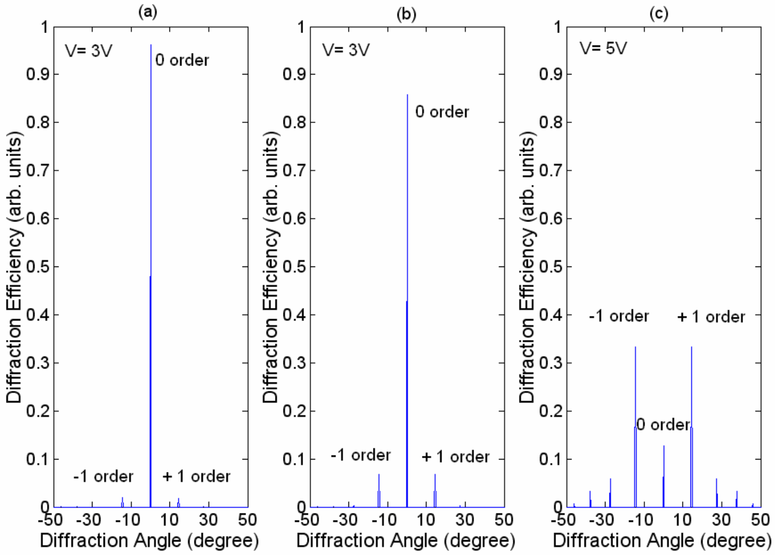

Fig. 4.2.3 Far-field diffraction patterns of normally incident light at 1.55μm for the maximum first order diffraction: (a) single-sided structure, biased at 3V, (b) double-sided structure in the biasing configuration A, biased at 3V, (c) double-sided structure in the biasing configuration B, biased at 5V.

the ideally binary profile. They are more close to sinusoidal phase gratings. The diffraction of a sinusoid phase grating is given by first-order Bessel function [14]. The theoretical upper limit for the efficiency of the first order diffraction is about 34% when the phase modulation depth reaches 1.17 π. The maximum phase modulation depths for both structures are listed in Table 4.2.1. High diffraction efficiency is expected when using the double-sided structure in the biasing configuration B since the 1.17 π phase-shift can be covered. Simulation shows the maximum first order diffraction efficiency for the conventional structure is only ~2%. However, by using our new double-sided structure, efficiency increases to ~6 % in the biasing configuration (A) and ~34 % in the biasing configuration B. Their far-field diffraction patterns are shown in Fig.4.2.3. The zero-order diffraction is efficiently suppressed by the first-order diffraction in our double-sided structure, which is clearly presented in Fig. 4.2.3 (c). Simulated results of the director profile for a 5 μm thick cell under the optimized voltage, which provides the maximum phase modulation depth, for various configurations are shown in the third column of Fig. 4.2.1. It is observed that the modulation in the conventional single-sided structure is very weak. The LC director in the lateral region is severely

	Theoretical predictions			Experimental results	
	Maximum phase shift (rad)	Maximum efficiency	efficiency Enhancement (times)	Maximum efficiency	efficiency Enhancement (times)
Single-side	0.54	~ 2%	1	~ 0.4%	1
Double-side A	1.01	~ 6%	3	~ 2%	5
Double-side B	4.15	~ 34%	17	~ 33%	80

Table 4.2.1 Theoretical predictions and experimental characterizations of the device performance.

distorted from its desired orientation in the horizontal direction due to the fringing fields. For this conventional structure, the simulation indicates that the best modulation condition occurs under a low biasing voltage of 3V since a larger voltage introduces even stronger fringing fields. A slight improvement can be observed in the double-sided structure in biasing configuration (A). However, the director distribution is still far from the ideal profile. A much more efficient director modulation can be obtained in biasing configuration (B) by choosing the right biasing voltage. Fig.4.2.4 presents the corresponding phase modulation of the transmitted TE wave under the optimized biasing voltages.

For the 5 μm thick LC cell, the maximum phase modulation depths for the single-sided structure and the double-sided structures in configuration (A) and (B) are 0.54 rad, 1.01 rad, 4.15 rad, respectively. One can find the phase profiles are mostly sinusoidal, where the far-field diffraction pattern can be simplified as the first-order Bessel function [14]. The theoretical upper limit of the first order diffraction is 33.8 % when the phase modulation depth reaches 3.67 rad (1.17 π). As shown in Fig. 4.2.4, this required 1.17 π phase-shift can be fully covered by configuration (B). It is also shown by

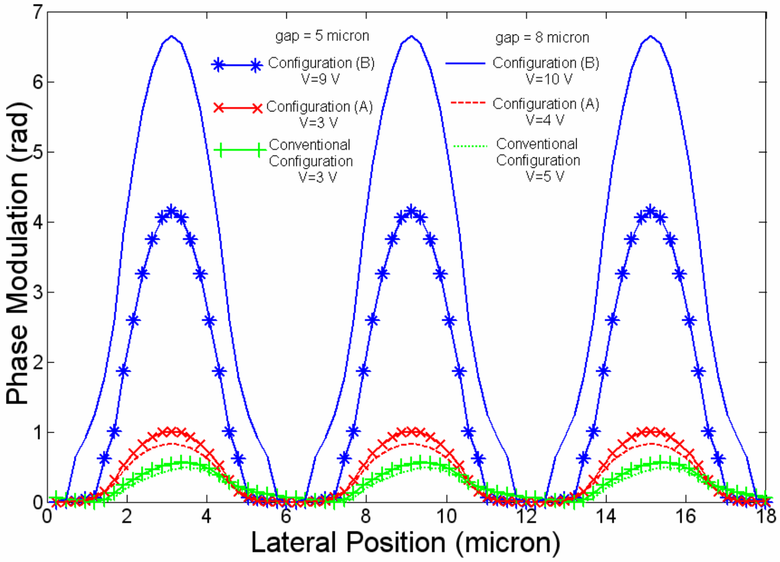

Fig. 4.2.4 Simulated phase modulation of the transmitted TE wave under the optimized biasing voltage for the single-sided and double-sided structures with LC layers of 5 μm and 8 μm, respectively.

Fig. 4.2.4, that the modulation depth for both the conventional single-sided structure and double-sided structure in configuration (A) decreases when the LC thickness increases. This effect is common for a high-resolution LC grating since the fringing-field effect usually increases with the cell thickness [47, 50, 51, 57]. However, the phase modulation depth of configuration (B) increases to 6.65 rad when the LC thickness increases to 8 μm. This is because the fringing-field effect has been efficiently suppressed in this unique design. This makes the device more attractive for working in the long wavelength near-IR and IR regions, where the large phase modulation depth is usually even harder to achieve. A thin phase-grating analysis is performed to simulate the far-field pattern by using the Fast-Fourier-Transfer (FFT) algorithm [14]. The simulated maximum first order diffraction efficiencies (not shown here) are ~2% and ~6 % for the single-sided structure and double-sided in configuration (A), respectively. In configuration (B), it increases to ~34 % which is close to the theoretical upper limit of a sinusoidal phase grating.

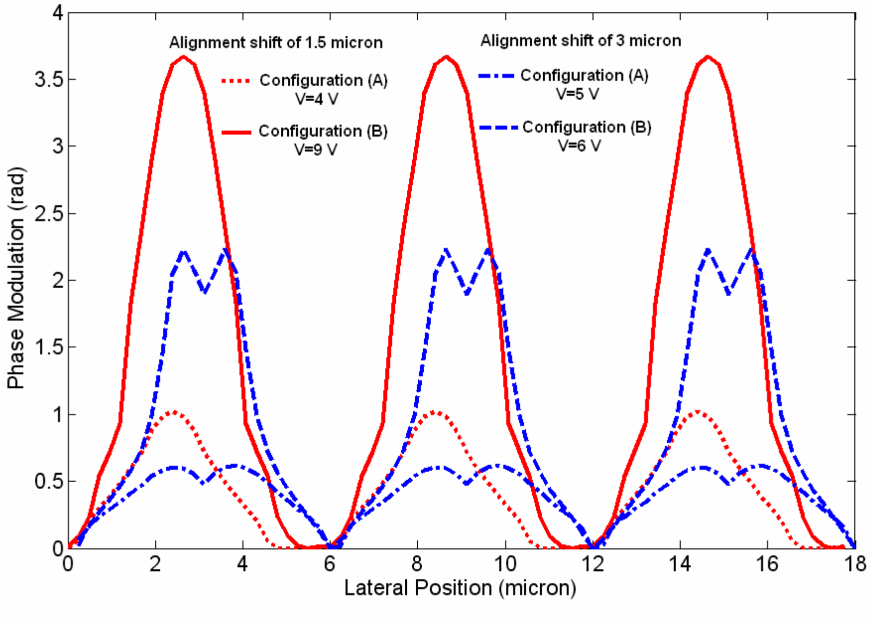

Fig. 4.2.5 Simulated phase modulations for double-sided structures in biasing configurations (A) and (B) with electrode misalignments of 1.5 μm and 3 μm, respectively.

The alignment tolerance of the electrode pixels was also investigated. Simulation results of the maximum phase modulation for the double-sided structures, where the top and bottom electrodes are misaligned by lateral shifts of 1.5 μm and 3 μm, are shown in Fig. 4.2.5. Compared with the phase modulation of the accurately aligned structure shown in Fig. 4.2.4, a slight degradation of the phase modulation is observed for the device with a misalignment of 1.5 μm. When the lateral misalignment increases to 3 μm, which is the maximum value of the possible misalignment in our structure, the phase modulation of configuration (B) is still much higher than the single-sided structure. The simulated far-field pattern shows that a maximum first order diffraction efficiency of 22% can be achieved in our double-sided structure with a misalignment of 3 μm, which is much larger than the simulated maximum efficiency of 2% for the conventional single-sided device.

4.3 Device Fabrication

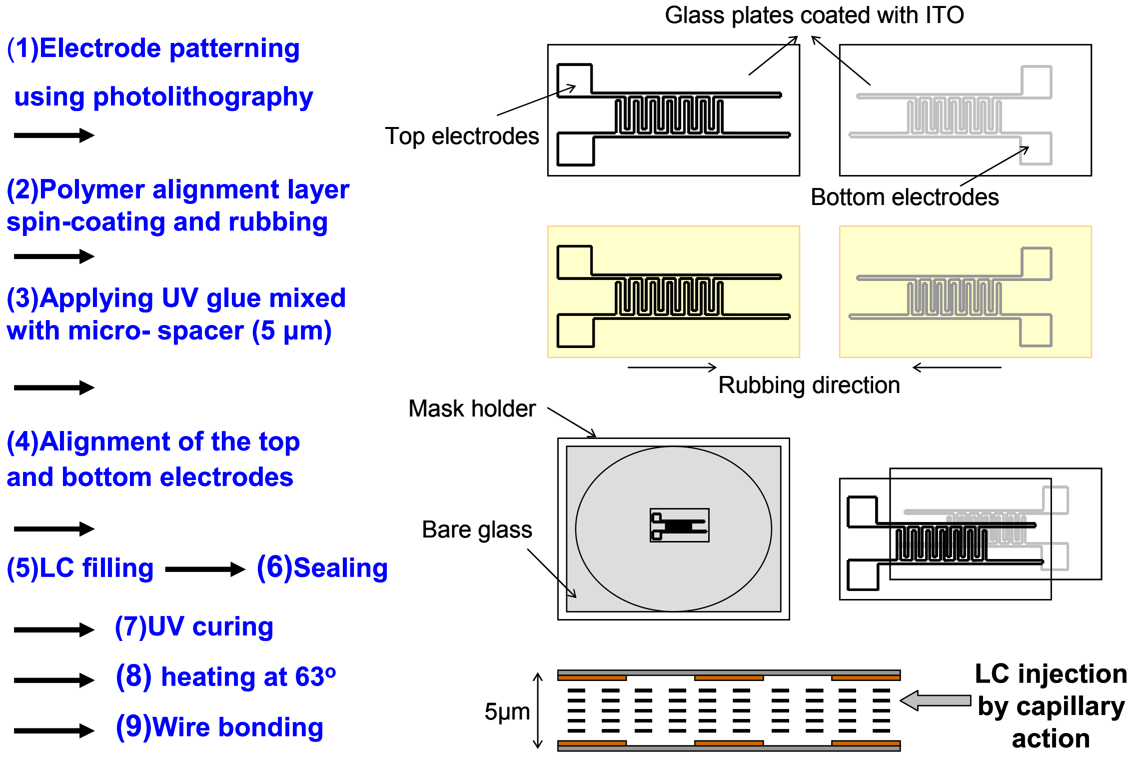

Fig. 4.3.1 Fabrication flow of the double-sided devices.

Both the single-sided and double-sided devices (with and without lateral misalignment) were fabricated. The fabrication flow of the double-sided devices is illustrated in Fig. 4.3.1. The details of the fabrication steps are provided as follows.

Process flow includes:

(1) Electrode patterning
(2) Alignment layer coating and rubbing
(3) Cell assembling
(4) Liquid crystal filling
(5) Cell sealing
(6) Cell heating

(1) Electrode patterning:

Material: ITO coated glass

Vendor: Delta Technologies

Sheet resistance (RS): 70 - 100 ohms,

Nominal Transmittance: >87%

Nominal Coating Thickness: 150 - 300 Angstroms

Substrate Thickness: 1 mm

(a)Lithography:

a. ITO cleaning:

   20% by weight solution of ethanolamine in deionized water, ultrasonic 15 minutes.

b. ITO baking: 150^{o} C for 30 minutes.

c. Photoresist coating:

   Primer: Spin speed =4000 rpm t =10 seconds

   AZ5209: Spin speed =4000 rpm t=30 seconds

   Pre-bake=90^{o} C for 10 minutes

d. Exposure: 30 seconds

e. Hard-bake: 120^{o} C 30 minutes

f. Develop: 30~35 seconds

(b)ITO etching:

i. Preparing etching solution:

$HCl : H_2O : HNO_3$= 4:2:1 by volume and a few drops of detergent to wetting the ITO surface.

The concentration of HCL is 36.5%-37.5% and that of HNO_3 is 70%.

ii. Etching: at R.T. for about 2 minutes

iii. Neutralization: 10% aqueous solution of Na_2CO_3

(2) Alignment layer coating and rubbing:

Material: PI-2556 (polyimide)
Vendor: HD Microsystems
Adhesion promoter: VM-652
Nominal Coating Thickness: ~100 nm

Coating Flow:

(a) Dilution of PI-2556 with N-Methyl-2-Pyrrolidone by volume ratio of 2:1.

(b) Application of Adhesion Promoter VM-652:
  Dispense
  Hold for 20 seconds
  Spin dry for 30 seconds
  Heating on hot plate at 120^{o} C for 60 seconds

(c) Polyimide coating:
  Spin speed =5000 rpm   t =60 seconds
  Soft bake on hot plate
  120^{o} C for 30 seconds followed by 150^{o} C for 30 seconds

Rubbing:

Rubbing material: Fine puff rubbing cloths
Rubbing distance: 1 meter
Rubbing direction: parallel to grating direction.

Fig. 4.3.2 shows AFM images of the rubbed and un-rubbed polyimide surfaces.

(3) Cell assembling:

Spacer: 5 micron micro-rod
Glue: Norland UV Sealant 91

(a) Mix spacer with UV-glue
(b) Clean surface by nitrogen gun
(c) Print two glue line onto the patterned substrate by a gold wire around the LC cell
(d) Push a planar ITO glass plate on to the bottom substrate with glue on it
(e) Tap the glue line firmly all the way around so as to make sure of even pressure
(f) UV curing : Intensity density = 20 mW/ mm
Time = 4 min

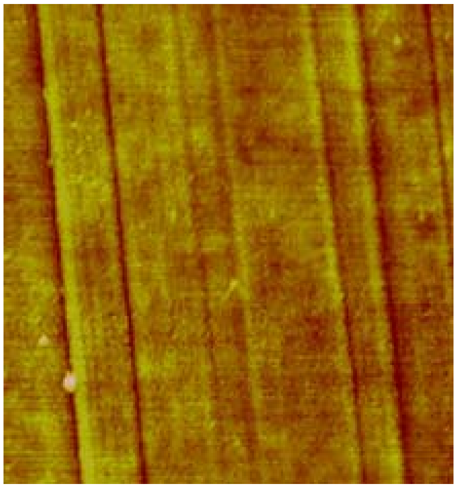

(a)

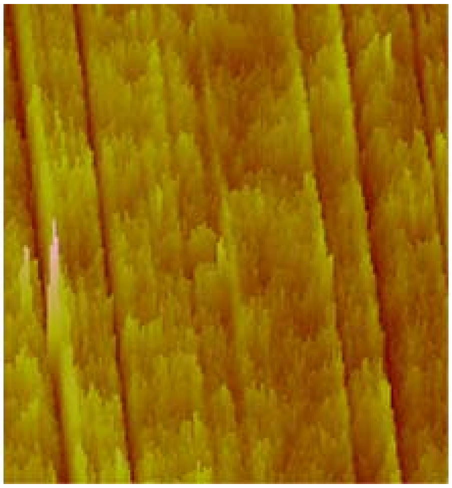

(b)

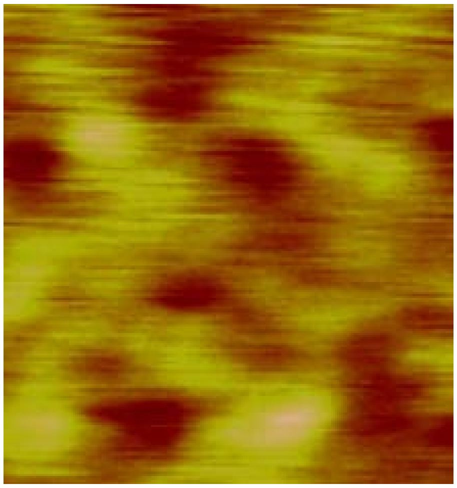

(c)

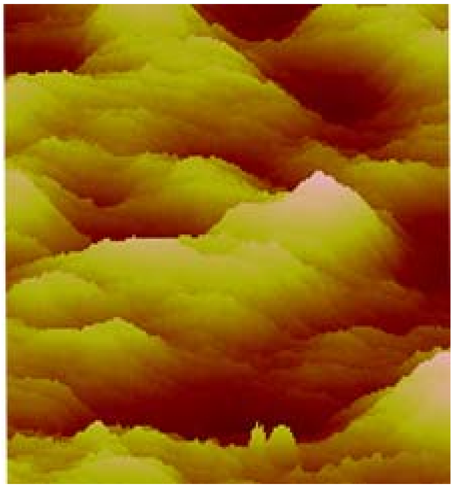

(d)

Fig. 4.3.2 Image dimension =2μm X 2μm. (a) Top view of the rubbed polyimide; (b) 45° angle view of the rubbed polyimide;(c) top view of the un-rubbed polyimide;(d) 45° angle view of the un-rubbed polyimide.

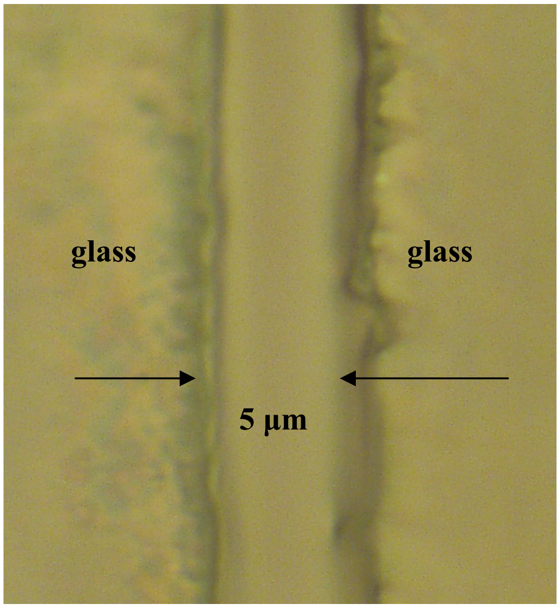

Fig. 4.3.3 Microscope image of the 5-μm-thick cell gap.

(4) Liquid crystal filling:

LC material: Merck E7 (positive dielectric anisotropy)
Filling method: capillary action

(5) Cell sealing: apply glue to the perimeter of the LC cell and cure for 4 minutes

(6) Cell heating: 61° C for 1 minute

Figure 4.3.4, taken through the microscope of the aligner, shows the accurate alignment of the top and bottom striped electrodes.

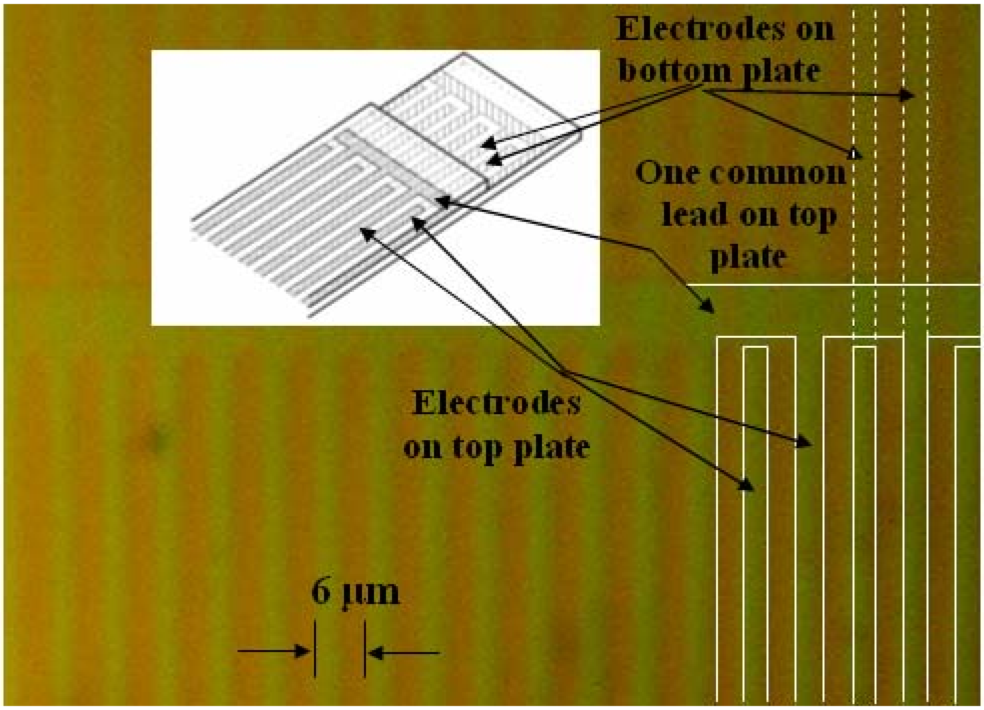

Fig. 4.3.4 Top view of the accurately aligned electrodes. Each plate has two groups of interdigited electrodes, each group being connected by a common lead. The frames are added for visual guide. The bottom plate is shifted toward the top of the picture to show the electrodes on the bottom plate, which have a less vivid green color than the ones on the top.

4.4 Device Characterization

A 1.55 μm laser was used for the optical characterization. A linear polarizer was placed between the laser and device to control the polarization of the incident beam. The primary diffraction of the device, i.e., the first order diffraction at 14.5°, for the single-sided and double-sided structures (with and without lateral misalignment) in biasing configuration (A) and (B) were characterized. A TE wave of 1.55 μm was used for the optical characterization. A function generator provided an AC voltage at 150 Hz. The diffraction intensity is normalized to the transmission intensity of the grating when there is no biasing voltage applied. Fig. 4.4.1 plots the measurement results. Compared with the single-sided structure, which has a maximum diffraction efficiency of 0.4%, the diffraction efficiency of the double-sided devices is greatly enhanced. For the double-sided structure with precise electrode alignment, the maximum diffraction efficiencies in biasing configuration (A) and (B) are 4.5% and 33%, respectively. Both results match well with the simulated results of 6% and 34%. An 80-time enhancement

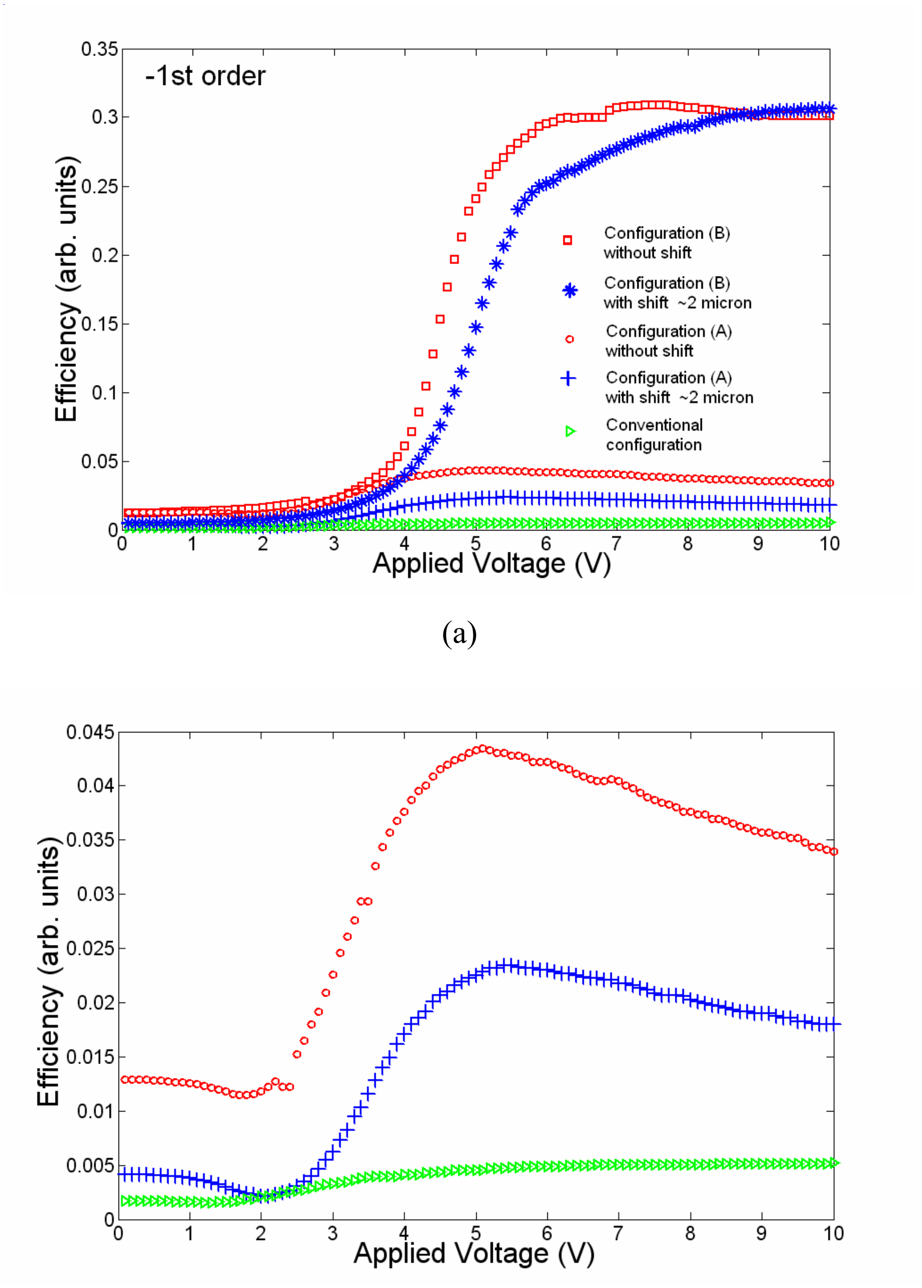

(a)

(b)

Fig. 4.4.1Measured values of the first order diffraction efficiencies of the conventional single-sided structure and the proposed double-sided structures, with and without electrode misalignments.

of the diffraction efficiency of the newly designed structure, with respect to the conventional single-sided structure, is experimentally confirmed. The influence of electrode misalignment on the device efficiency was experimentally studied. When there is a 2 μm lateral shift between the opposite electrodes, the diffraction efficiency of configuration (A) decreases by half, which is clearly shown in Fig. 4.4.1 (b). However, no significant reduction of the efficiency occurs in configuration (B). This can be explained by the simulated phase profiles under electrode misalignments, which are shown in Fig. 4.3.4. As shown in Fig. 4.4.1, a misalignment of 2 μm can be fully compensated by increasing the biasing voltage from ~7V to ~9V, which considerably relaxes the alignment stringency in device assembly.

4.5 Summary

In conclusion, we have proposed and fabricated a two-level LC grating working at 1.55 μm. By applying a unique biasing configuration to a double-sided structure, the distortion of the LC directors due to the fringing-field effect is significantly suppressed, which leads to a much larger phase modulation depth and higher diffraction efficiency. A diffraction efficiency of 33% at the first order diffraction angle of 14.5^o was experimentally achieved. The efficiency has been enhanced 80 times compared with the conventional structure and approaches the theoretical limit. Experiments have confirmed that no significant performance degradation occurs under an electrode misalignment of 2 μm. For the current device to work as a programmable grating, a common method is to selectively activate a subset of electrodes, whose pitch p is a multiple of the fundamental pitch p_0. Our structure ensures that the programmed state with the smallest p ($=p_0$) and therefore the worst fringing-field effect has high phase modulation depth, the other states are generally better, which was confirmed by simulations.

Chapter 5

2-D periodic-structure-based device (I):

Thermo-optically-tuned photonic-crystal-waveguide-based silicon-on-insulator MZI modulators

5.1 Introduction

5.1.1 Research motivation

The driving force behind the development of silicon photonics is the monolithic integration of optics and microelectronics. Silicon remains the dominant material for microelectronics ever since the invention of the integrated circuit. It is well known that silicon is transparent in the range of optical telecommunication wavelengths, and has a high refractive index that allows for fabrication of high-index-contrast micro- and sub-micro-photonic structures. Silicon-on-insulator (SOI) has been identified as a promising material for integrated optoelectronics. Complementary metal oxide semiconductor (CMOS) circuits fabricated on SOIs benefit from the reduced parasitics and absence of latch-up problem, which enable high-speed and low-power electrical operations. On the other side, SOI provides strong optical confinement for the telecommunication wavelengths, which offers an ideal platform to realize integrated photonic wave-guiding devices. Optical integrated switches and modulators are key components for photonic integrated circuits.

The Mach-Zehnder interferometer (MZI), which converts a phase modulation to an amplitude modulation, is the most extensively studied modulator structure because of its superior optical performance, such as high extinction ratio and large bandwidth of the operating wavelength. A Thermo-optically-tuned MZI modulator/switch is considered an attractive device for low-cost and low-frequency applications [61-63]. Among many available material systems, silicon is a great choice for implementing thermo-optic (TO) MZI modulators operating at 1.5μm. One reason is that silicon is transparent at this communication wavelength. Additionally, the TO coefficient in silicon is approximately

$1.86\ X10^{-4}\ K^{-1}$, which is two times greater than polymers and twenty times greater than SiO_2 and Si_3N_4. The final reason that silicon is a good choice is because the thermal conductivity of silicon is 100 times higher than SiO_2, and therefore provides a comparatively fast switching speed.

Despite the steady trend towards the scaling down of the silicon microelectronic devices, little progress has been made in the miniaturization of silicon optical devices. Most active silicon optical devices have remained comparatively large, in the range of hundreds of microns to a few millimeters [62-64]. This is due to intrinsically weak interactions between light and other external fields exhibited by silicon material. Photonic crystal (PhC) is a new material system that presents a huge potential for developing ultra-compact optical devices [66-69], because of its unique properties such as photonic band gap and slow light group velocity [6-9]. Optical waveguides based on photonic crystal line defects, the so-called line-defect photonic crystal waveguides (PCWs), have been demonstrated to provide a few orders of magnitude larger dispersion than conventional waveguides [70-72]. Such an extraordinary dispersion capability has a profound impact on the phase velocity change over a segment of photonic crystal waveguides. By locally controlling the external fields such as thermal and electrical fields over the PCW region, a tremendous amplification of optical response to the variation of material property is achievable due to the high spectral dispersion of the PCW. This improvement results in a significant reduction in the size and power consumption of the PCW-based optoelectronic devices. When PCWs are incorporated in a MZI, they lead to a significant enhancement of the phase modulation efficiency, which may result in a ten or hundred-fold reduction in the modulator electrode length.

5.1.2 Slow group velocity of photonic crystal waveguides

As introduced in Chapter 1, tremendous research efforts have been made to investigate 2-D PCWs because of their significance in realization of novel integrated photonic devices. PCWs are essentially 1-D defects created inside a photonic crystal. The simplest PCW is formed by removing a row of “atoms”. As light is totally reflected by photonic crystal walls (the claddings of the waveguide) for a certain frequency, the light will be confined in the line defect region and form a guided mode. As illustrated in Fig.

5.2.1 (a), one of the most useful features of PCW is the extremely low group velocity or high spectral dispersion at its transmission band edge. This unique property of PCWs has been carefully demonstrated and characterized experimentally [68, 70, 73, 75]. Excellent agreement between theoretical prediction and experiment dispersion curve has been confirmed with careful design and fabrication.

Consider a typical dispersion relation for a PCW mode shown in Fig 5.1.1. If the refractive index of the waveguide core material (*i.e.* silicon) varies by an amount of Δn, the dispersion curve will shift vertically by an amount $\Delta\omega_0$. For a fixed frequency of light, the propagation constant β_{pc} of PCW changes as $\Delta\beta_{pc} = \frac{d\beta_{pc}}{dw}\Delta w_0$, which grows significantly whenever the group velocity $(\frac{d\beta_{pc}}{dw})^{-1}$ approaches zero, e.g. on the right-most segment of dispersion curve in Fig. 5.1.1. Such an extraordinary growth of $\Delta\beta_{pc}$ directly leads to a significant enhancement of phase modulation efficiency because the

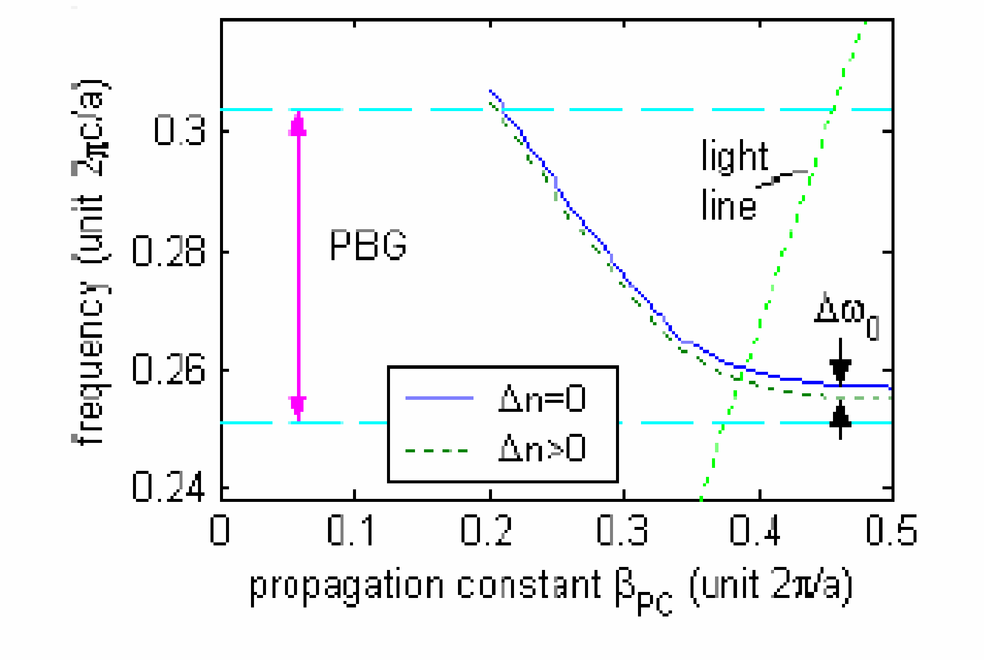

Fig. 5.1.1 Photonic crystal waveguide dispersion relation, used to illustrate the principle of enhancing modulation efficiency through highly dispersive photonic crystal waveguide [65].

phase change is related to the change of propagation constant and waveguide length L as Δ φ=Δ βpc X L . Therefore, a much shorter PCW can produce the same phase change as a long conventional waveguide due to the significant increase of Δ β pc. The short device length is a beneficial feature for many other device performance considerations. Propagation loss for PCWs has been a concern for some applications that employ a long PCW segment. With the advance of nano-fabrication technology, the propagation loss for PCWs has been controlled to below 0.5 dB/mm [76]. The proposed device has a short PCW of a few tens of microns in length, resulting in a low propagation loss.

5.2 Optical simulations of line-defect photonic crystal waveguides

It has been discovered that the dispersion curve of the guided mode in PCW can be made as flat as desired with an appropriate design [70-72]. At the flat band regions, the guided modes demonstrate extraordinary high dispersion, and hence the extremely small group-velocity ($d\omega / dk$), which makes it possible to shrink the size of time-delay /phase-shift devices significantly [65, 68, 71, 77-79]. To get a clear idea how slow group velocity in silicon PCWs can dramatically increase the induced phase shift by a small change in the refractive index of silicon, we have simulated photonic bands and dispersion curves of a silicon line-defect PCW of a specifically designed PhC structure.

The band diagram for the TE-like polarization in a silicon PhC slab was simulated using the plane wave expansion method. The selected structure is a 230-nm-thick silicon PhC slab immersed in a low-dielectric material with a refractive index of 1.45. A defect-line PCW is generated by removing the central row of the low-dielectric material along the Γ-K direction of a hexagonal lattice, as illustrated in Fig. 5.2.1 (a). The lattice constant and hole diameter are 400nm and 220nm, respectively. Fig. 5.2.1(b) shows two sets of dispersion curves of the designed silicon PCW, one with a silicon refractive index (n) of 3.46, and the other with a small variation of refractive index (Δn) by - 0.001. Two guided modes (line-defect modes) appear in a widely opened photonic band gap (PBG). The dispersion curves of these guided modes are very flat close to the edge of the Brillouin zone, which indicates an extremely small group velocity ($d\omega / dk$) of the PCW at the band edge of the defect mode. As seen in the magnified view of this slow group-velocity region, shown in the inset of the Fig. 5.2.1 (b), a small perturbation of the refractive index causes a little vertical shift of the dispersion curve.

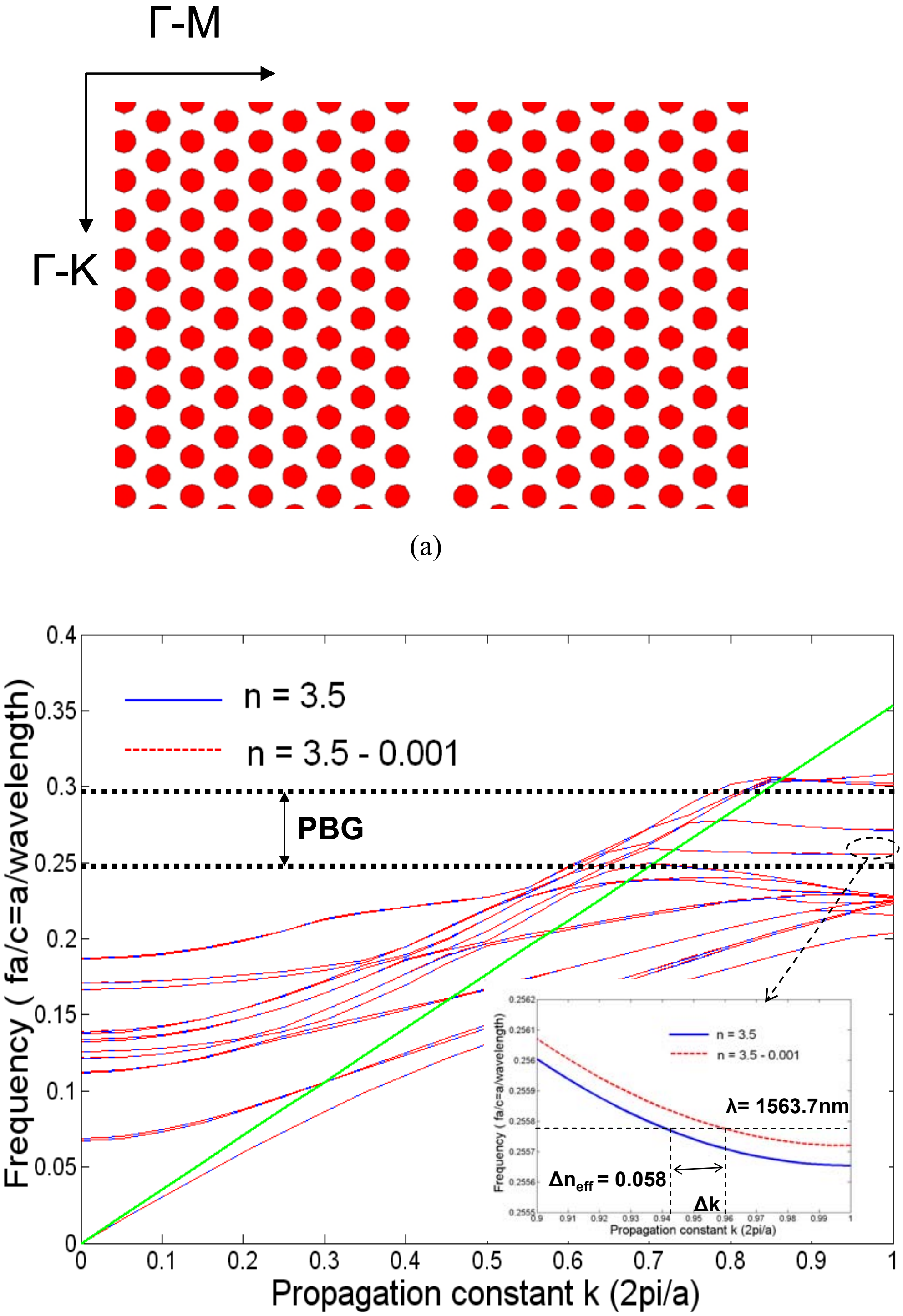

(a)

(b)

Fig. 5.2.1 (a) Schematic of the line-defect photonic crystal waveguide; (b) Theoretical dispersion curves of the line-defect photonic crystal waveguide.

However, this small shift can lead to a drastically different change in the wave vector of the propagating light, depending on the local group velocity. For example, given a constant operation wavelength λ = 1536.7 nm, illustrated by the horizontal dotted line, a perturbation of material's refractive index (Δn) by 0.001 would cause a substantial change of the wave vector, which in turn results in a large change in the effective index change of PCW by 0.058. This unique phenomenon tremendously impacts the phase modulation for phase-shift devices, such as MZI modulators. It is well established that the required interaction length to obtain a π-phase shift for a guided wave in MZIs is given by:

$$L_{\pi} = \frac{\lambda}{2\Delta n_{eff}} . \tag{5.2.1}$$

The change of the effective refractive index Δn_{eff} for conventional dielectric waveguides is approximately equal to the induced change of the material's refractive index Δn. In contrast, the Δn_{eff} of PCWs is usually tens or hundreds, or even thousands, of the Δn. Equation 4.2.1 states that a significantly enhanced Δn_{eff} in PCW enables a huge shrinkage of the device length of MZI modulators. In this chapter, we report an ultra-compact silicon photonic crystal thermo-optic (TO) MZI modulator which reaps the unique technical benefit offered by PCWs.

In our proposed TO MZI, we placed the metal heater on one side of the PCW, as shown in Fig. 5.2.2 (a). Decreasing the lateral distance between the heat source and the optical confinement region largely facilitates the heat exchange. However, a large amount of absorption loss occurs when the optical field is in proximity to the metal heater. Knowing the optical mode profile of the PCW will help reach a balance and solve both issues. The optical mode profile of a carefully designed PCW was simulated by the plane wave expansion method. Fig. 5.2.2 (b) and (c) show the top view and surface plot of the magnetic field density profile of the PCW mode. It is obvious that most energy is confined within the central line-defect region and becomes evanescent into the adjacent photonic crystals on both sides. A more than 40dB decrease of optical energy is obtained 1.5 µm away from the line defect on each side of the PCW. This simulation indicates that optical loss due to the metal absorption is negligible as long as the metal heater is at least 1.5 µm away from the line-defect region. In our designed structure, 15 columns of air-holes with diameter of 400 µm are defined on each side of the line-defect to achieve a great optical confinement. An aluminum metal heater was placed on one side of the active PhC region, which is around 5.2 µm away from the central position of the line-defect. This gives an adequate margin in space to avoid extra optical absorption losses.

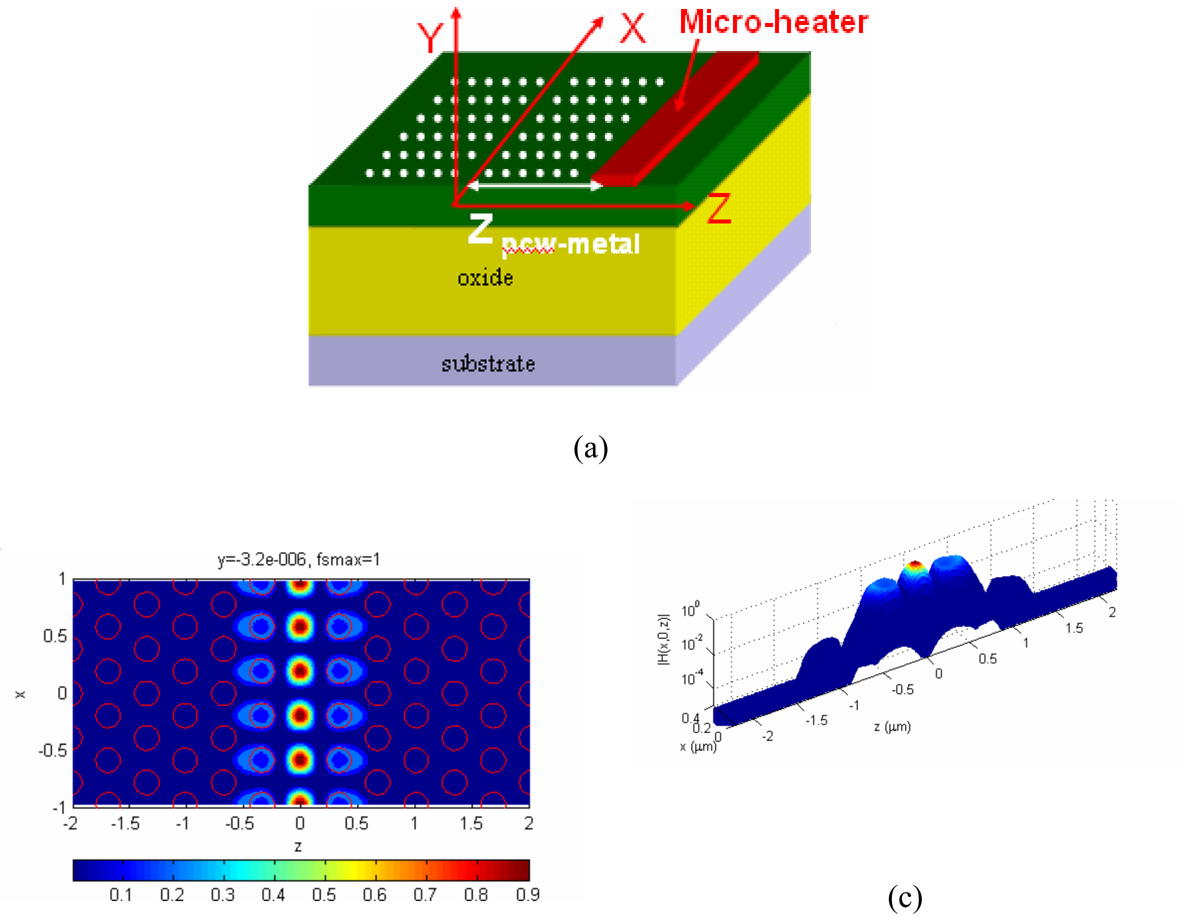

(a)

(b)

(c)

Fig. 5.2.2 Optical simulations of a photonic crystal waveguide (a) The device structure; (b) Top view of the mode field (contour plot) in the x-z plane; (c) Surface plot of the mode field in the y-z plane.

5.3 Thermal design of thermo-optic (TO) silicon photonic crystal modulators

Size reduction by one order of magnitude has been demonstrated for a silicon thermo-optic (TO) Mach Zehnder interferometer (MZI) based on photonic crystal waveguide (PCW) [80]. The reported PCW based TO MZI employed a traditional thermal design, illustrated in Fig. 5.3.1 (a) and (b), where a resistive heating element was designed to sit

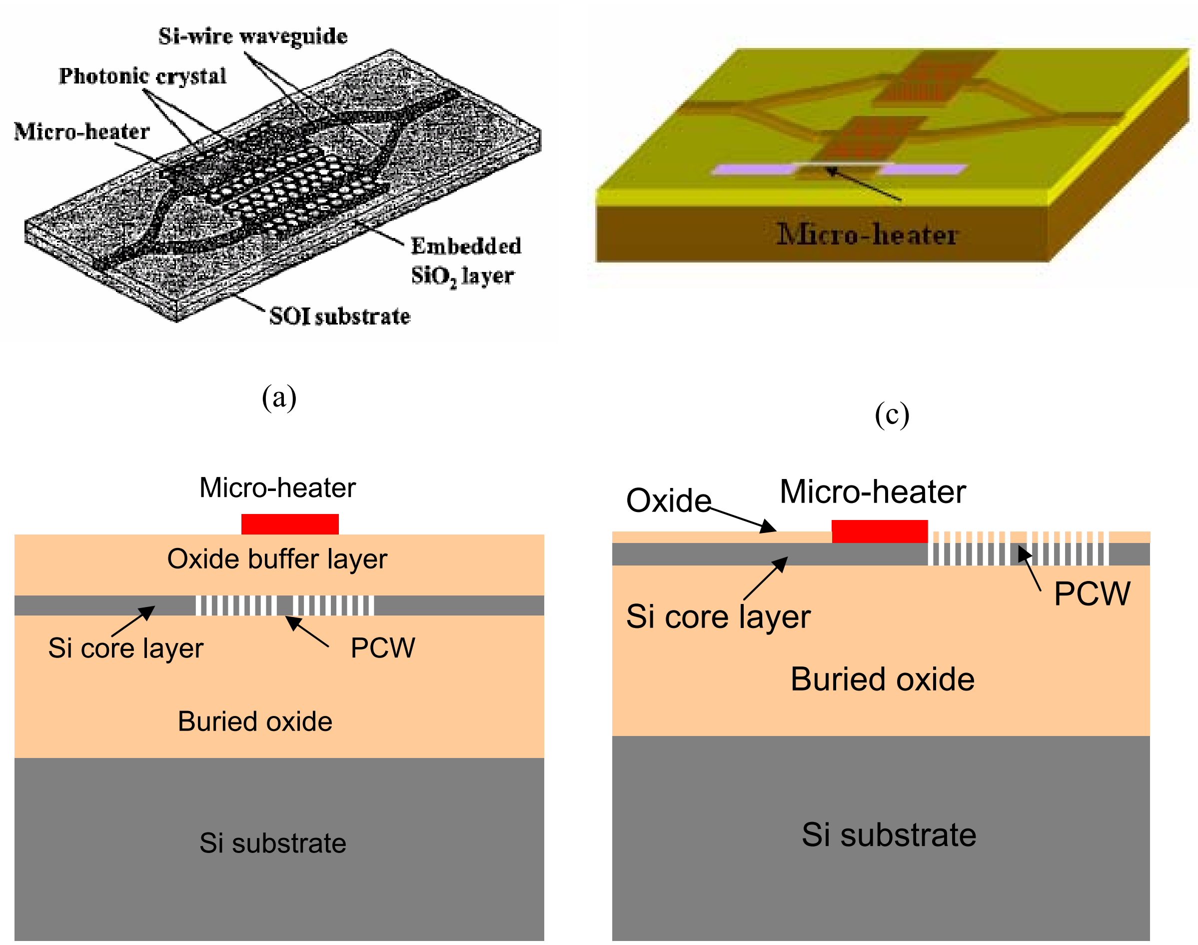

(a) (c)

(b) (d)

Fig. 5.3.1 Schematics diagrams of PCW based SOI thermo-optic MZI. (a) Perspective view of a previously reported structure [81] (b) cross-sectional view of the structure in (a); (c) Perspective view of our thermo-optic structure (d) cross-sectional view of the structure in (c).

on top of the active region of the MZI. In such a device configuration, a SiO_2 layer varying from a few hundred nanometers to a few microns in thickness must be inserted between the thin-film metal heater and the silicon waveguide, providing reliable electrical and optical isolations as well as an adequate mechanical support for the metal heater. However, this SiO_2 layer is considered an undesirable thermal buffer, which hampers the efficiency of the heat exchange between the heater and the silicon waveguide due to the much lower thermal conductivity of SiO_2 compared with that of silicon. Consequently, this constitutes the true speed-limiting factor for the TO MZIs. However, to deposit an oxide buffer layer on top of the silicon core layer could be problematic in the fabrication of PCW based devices. This is because the deposited SiO_2 could partially block the air holes of the PCWs [66], and may unexpectedly change the designed transmission properties or increase the propagation loss of PhC devices.

We will present a new thermal design where the resistive metal heater is designed to be in direct contact with the silicon core layer. We deposited the micro-heater at a location closely adjacent to the active PCW region other than on top of the waveguide. The perspective and cross-sectional schematics of our device are shown in Fig. 5.3.1(c) and (d), respectively. Compared with the conventional oxide buffered structure, the direct contact between the micro-heater and the silicon core layer allows a more efficient heat transfer from the heat source to the actively controlled PCW region due to the high thermal conductivity of silicon, which is 100 times larger than that of SiO2. In addition, the buried oxide (BOX) layer of silicon-on-insulator (SOI) wafers functions as a vertical thermal barrier, which further facilitates lateral heat exchange between the heater and the wave-guiding region. This novel thermal design is expected to bring various advantages such as high speed, low power consumption and less complication in device fabrication.

Both steady-state and transient thermal analyses have been performed to assess the thermal performance of our TO SOI MZIs. ANSYS, a commercial finite element engineering software package, was used to model the temperature distribution across the device active region and evaluate the rise/fall time of the TO devices. The layout of the thermal simulation followed the same dimensions as the TO MZIs we fabricated. The simulated structure is illustrated in Fig 5.3.1(d). The device was designed on an SOI wafer consisting of a 0.26 μm-thick silicon top layer, a 2 μm-thick buried oxide layer and a silicon substrate. An 80 nm-thick oxide layer was thermally grown on top of the silicon core layer, which served as the etching mask for silicon in reactive ion etching. A 160 μm X 20 μm cross-sectional area of silicon substrate was chosen in the simulations to ensure a valid room-temperate boundary condition at the bottom and the left / right side of the device. The third dimension of the device was assumed infinite in a two-dimensional thermal analysis. Each layer of the device structure was meshed independently. The maximum meshing size was restricted to less than 0.02 μm to ensure the accuracy of the simulation results. An 8 μm-wide by 250 nm-thick aluminum micro-heater was placed on top of the silicon core layer. The micro-heater was separated from the center of the active PCW by 5.2 μm. A 5 μm-wide air trench was added on the silicon core layer 40 μm away from the resistive heater to provide thermal isolation between the active arm and passive arm. The resistively generated heat was mostly transported away from the micro-heater through the silicon core layer rather than dissipating in the ambient air because of the extremely large thermal conductivity of silicon versus air [82]. We ignored the small portion of heat transferred away by the air above the device and assumed the insulated boundary condition at the top surface of the device. The temperature profile across the device under a heating power of 70 mW is shown in Fig. 5.3.2(a). A temperature rise of 9 ^{o}C at the center of the PCW active region was observed. We can do a simple calculation for the required device length to achieve π phase shift in a MZI using a formula $\Delta\phi = \frac{2\pi}{\lambda}(\frac{dn_{eff}}{dT})\ \Delta TL$, where $\Delta\phi$ is the phase shift of guided-wave, n_{eff} is the effective refractive index of the waveguide, λ is the wavelength of the light signal, ΔT is the temperature variation, and L is the length of the active arm of the MZI. For a 9 ^{o}C rise in temperature, the required length of the active arm in a conventional silicon waveguide based MZI was 460 μm as $\frac{dn_{eff}}{dT}$ of the conventional waveguide is almost equal to the material TO coefficient, which is of a typical value of 1.86 X 10^{-4} K^{-1} in silicon. However, we will see that a significant size reduction of the device has been experimentally realized by incorporating highly dispersive PCWs into MZI structures. Transient thermal analysis was also performed with a calculation time increment of

0.1μs. The temperature rise sampled at the center of the active PCW versus time was plotted in Fig. 5.3.2(b). Our simulation showed the temperature rise time of the

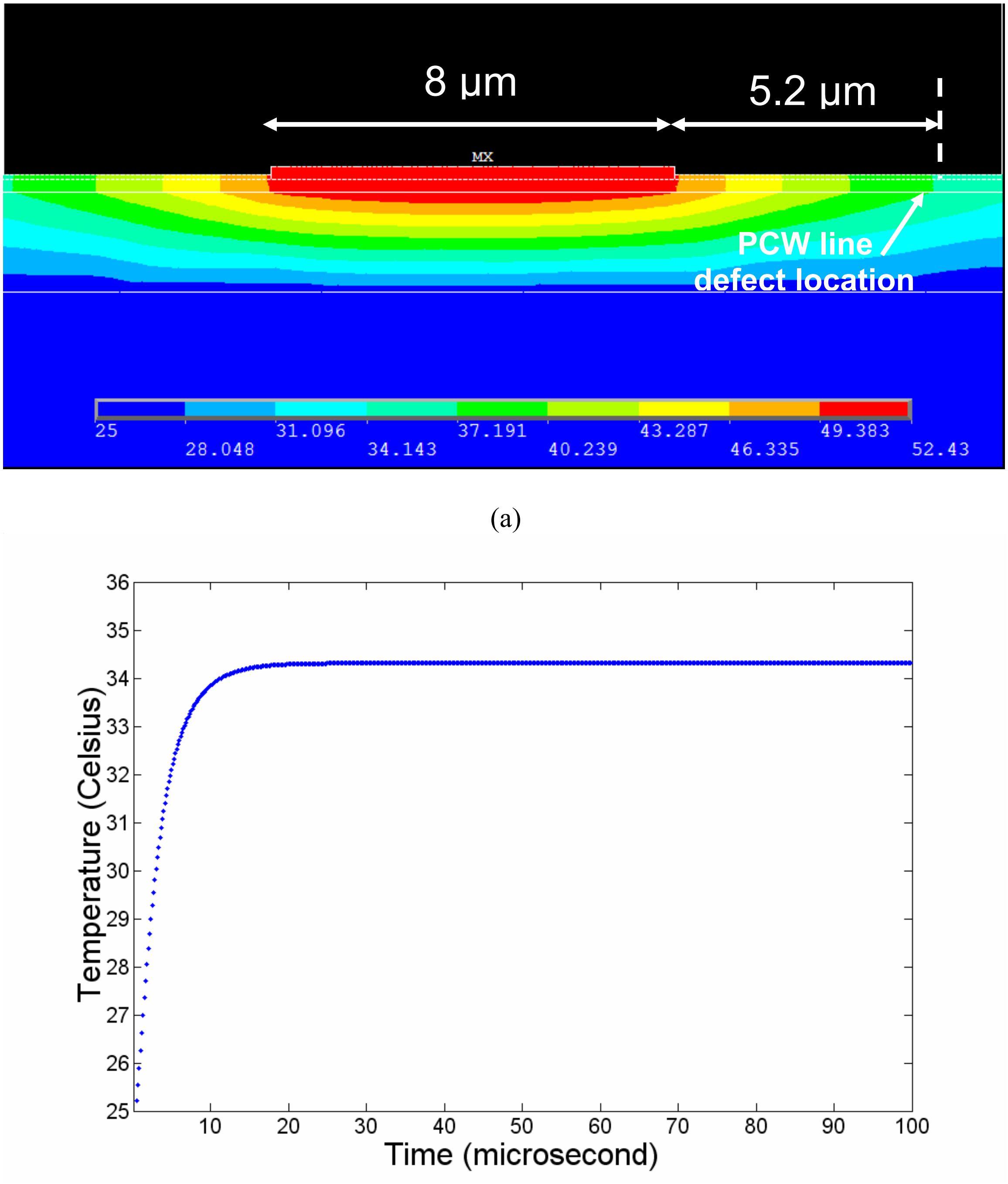

(a)

(b)

Fig. 5.3.2 ANSYS steady-state and transient thermal analyses: (a) temperature distribution across the device under a heating power of 70 mW; (b) temperature rise versus time at the center of the active region.

designed structure was less than 20 μs. This simulation indicated that our device should be faster than the previously reported PCW based SOI TO MZI, where a conventional thermal design was employed and a typical switching time over 100 μs was characterized [80].

5.4 Device fabrication

Fabrication procedures of SOI based photonic crystal devices have been developed carefully through extensive experimental trials. The fabrication sequence,

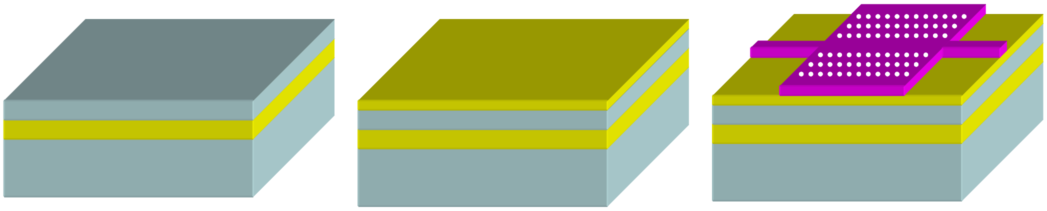

(1) Start with SOI wafer

(2) Thermal growth of oxide hard mask (~80nm)

(3) Define passive waveguides (PCWs and channel waveguides) on ZEP-520A resist(~320nm) using Jeol JBX6000 E-Beam lithography facility

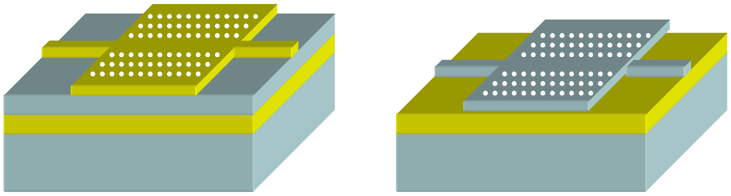

(4) Dry etch oxide with CHF_3 to transfer pattern from the e-beam resist to the oxide hard mask , strip off e-beam resist

(5) Dry etch the underlying silicon with $HBr + Cl_2$

Fig. 5.4.1 Fabrication flow of passive structures of photonic crystal devices based SOI wafer.

illustrated in Fig. 5.4.1, starts with a thorough Piranha clean of 6” SOI wafers. It is followed by a thermal oxidation of silicon top layer in water steam at 850°C for about 10 minutes, which forms an 80-nm-thick top oxide layer. Device passive structures are defined on E-beam resist (ZEP-520A) using E-beam lithography (JEOL JBX-6000FS/E, resolution: 20 nm). Following that, device patterns are transferred to the oxide mask layer by reactive ion etching (RIE) using CHF_3. A Piranha clean then strips off the e-beat resist. As a last step to form the passive structure, device layer of silicon is etched by RIE in HBr and Cl_2. The air holes of the silicon photonic crystals expanded noticeably after completing the entire fabrication sequence. E-beam resist exposure and development, dry-etching of the oxide hard mask and the SOI layer all incurred certain amount of expansion of the holes. The submicron-structures of silicon photonic crystal waveguide have been imaged by a FEI Strata DM235 SEM/FIB. Top- and 45^{o}-view scanning electron microscopy (SEM) images of the passive PCW are shown in Fig. 5.4.2.

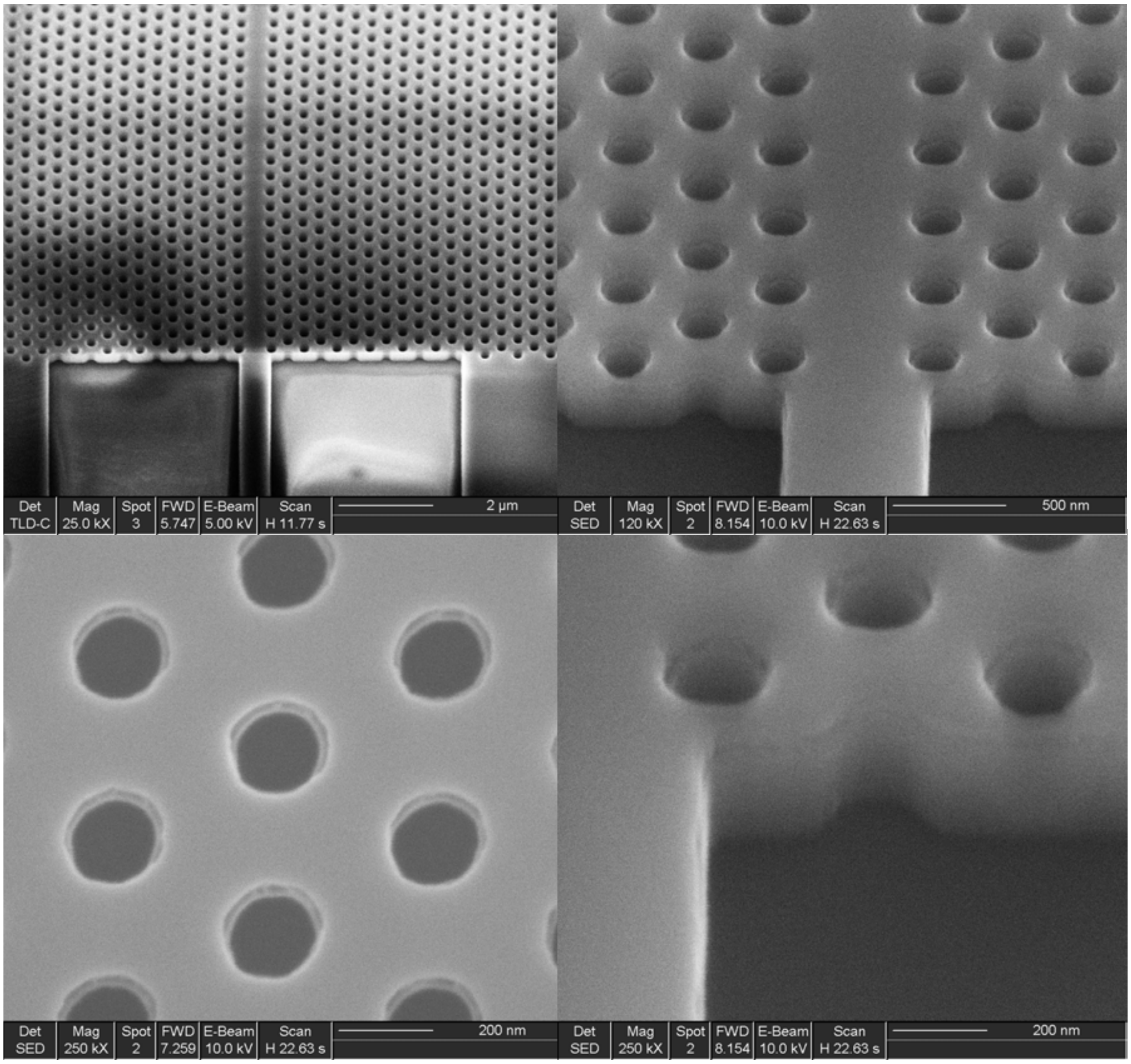

Fig. 5.4.2 SEM images of the PCW.

A thermal-optically-tuned PhC silicon MZI modulator incorporating the aforementioned passive PCW structure was fabricated and characterized. The schematic of the device structure is shown in Fig. 5.4.3 (a). Top-view microscope and SEM images of the main sections of the PhC TO MZI are shown in Fig. 5.4.3 (b), (c), and (d).

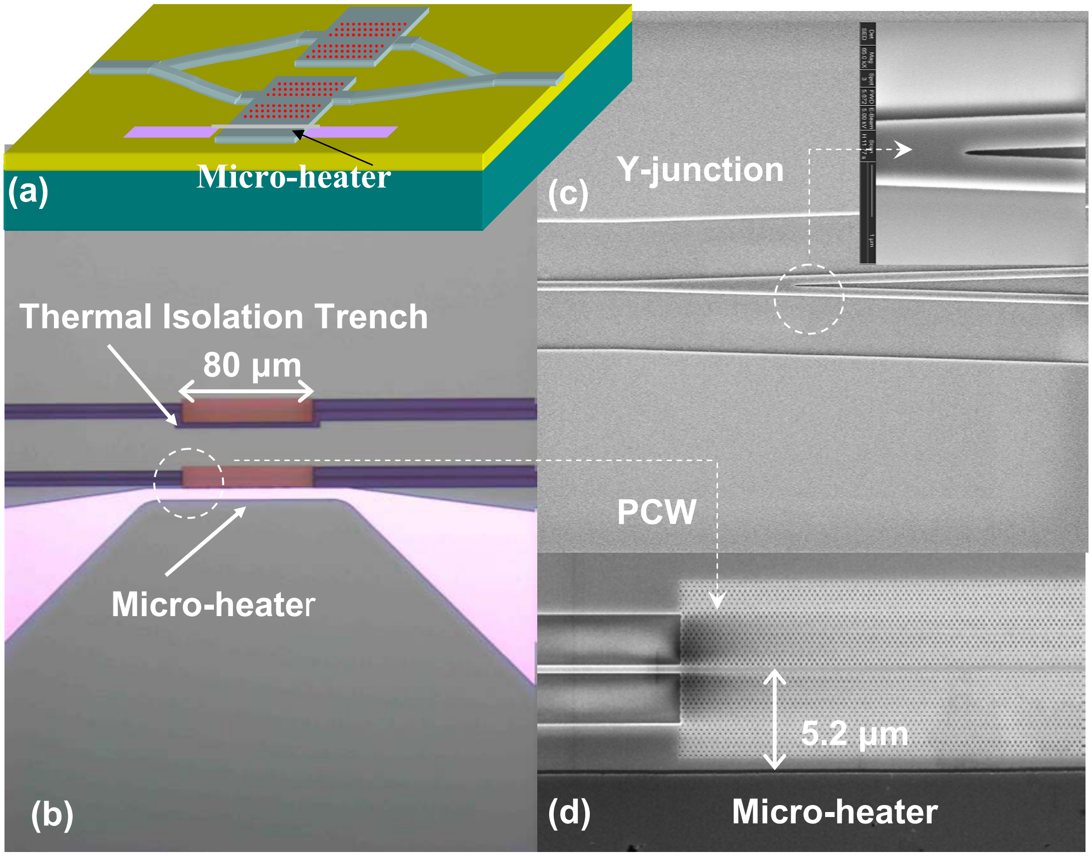

Fig. 5.4.3 Schematic, microscope and SEM images of a thermo-optically-tuned photonic crystal silicon MZI modulator. (a) Schematic of the MZI;(b)top-view microscope image of the MZI;(c)top-view SEM image of Y-junction;(d)enlarged top-view SEM of the active arm of the MZI.

Two 80 μm-long PCWs were obtained by removing central rows of air holes in a hexagonal lattice of silicon PhCs for both active and passive arms. The input and output waveguides of the MZIs were gradually widened to 2 μm at the edge of device chips to facilitate the light coupling. The lattice constant and the air hole diameter were designed to be 400nm and 212nm, respectively. An air trench was added between two PCWs to achieve a good thermal isolation between the active arm and passive arm of the MZI. A window for metal deposition was opened through the top oxide layer by photolithography. A 250 nm-thick, 8 μm-wide and 120 μm-long aluminum heater was formed by electron beam evaporation and a standard lift-off process on top of the silicon core layer. It was placed closely adjacent to the active arm of the MZI. The measured resistance of the micro-heater was approximately 20 Ω.

5.5 Device characterization

Our fabricated MZI devices were tested on a fully-automated Newport Photonics Alignment/Packaging Station. A tunable external-cavity laser source was pigtailed to a single mode lensed fiber and butt coupled into the MZI device. The output signal was collected by a multimode lensed fiber. The input and output lensed fibers can be accurately aligned with silicon waveguides by two five-axis high-precision stages under a computerized control. The input laser was polarized to transverse electric (TE) wave for optical measurements. The switching properties were obtained by applying a square wave heating current to the micro-heater. The optical performance of our MZI was characterized at a wavelength of 1548 nm, which is near the edge of the defect mode transmission spectrum, as shown in Fig. 5.5.1.

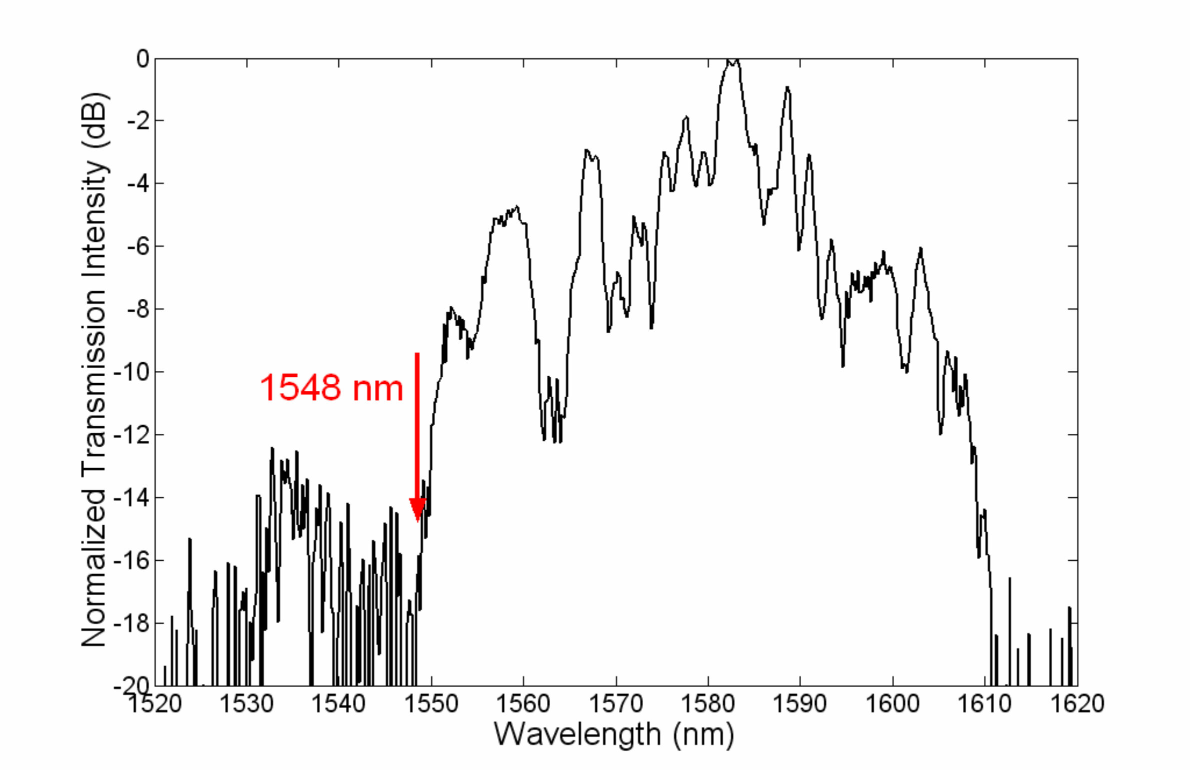

Fig. 5.5.1 Transmission spectrum of the PCW based MZI.

The switching curves under the modulated signal at 3 kHz were demonstrated on a digital communication analyzer. The switching rise time (from 10% to 90% transmission) and fall time (from 90% to 10% transmission), shown in Fig. 5.5.2 (a) and (b), were measured to be 19.6 μs and 11.4 μs, respectively. The measured rise time agrees well with the simulation result from the ANSYS transient thermal analysis. Switching time around 100 μs of a PCW based SOI TO MZI with a micro-heater sitting on the top of a PCW was previously reported. Our results clearly demonstrate a speed improvement using a novel strategy where the heater was placed on the side of the active arm and was in direct contact with the silicon core layer. Modulation traces at 1 kHz and 30 kHz are shown in Fig. 5.5.3 (a) and (b), respectively. The modulation depth decreases by half when the modulation frequency increase up to 30 KHz, which implies the 3 dB bandwidth of our thermo-optic modulator The output optical intensity against the applied heating power at λ=1548 nm was plotted in Fig. 5.5.4. A maximum modulation depth of 84% has been obtained for a switching power of 78 mW. It was previously shown by our

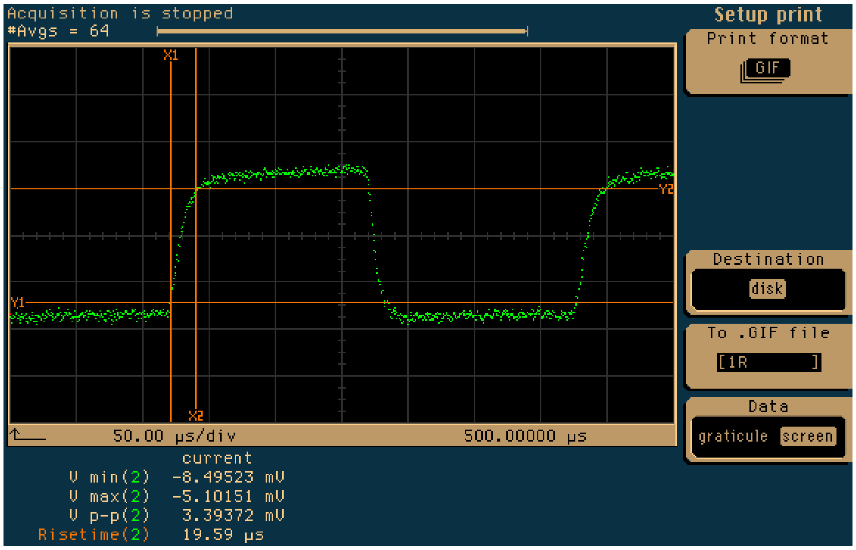

```
Acquisition is stopped
#Avgs = 64
50.00 µs/div            500.00000 µs
              current
   V min(2)   -8.49523 mV
   V max(2)   -5.10151 mV
   V p-p(2)    3.39372 mV
Risetime(2)    19.59 µs
```

(a)

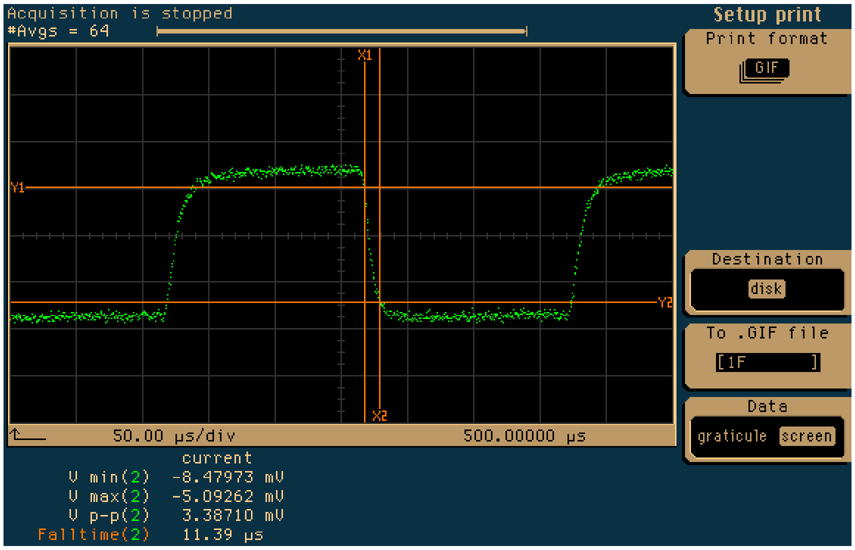

```
Acquisition is stopped
#Avgs = 64
50.00 µs/div            500.00000 µs
              current
   V min(2)   -8.47973 mV
   V max(2)   -5.09262 mV
   V p-p(2)    3.38710 mV
Falltime(2)    11.39 µs
```

(b)

Fig. 5.5.2 Switching characteristics of photonic crystal waveguide based silicon-on-insulator thermo-optic Mach Zehnder interferometer at 3 kHz: (a) rise time of 19.6 µs; (b) fall time of 11.4 µs.

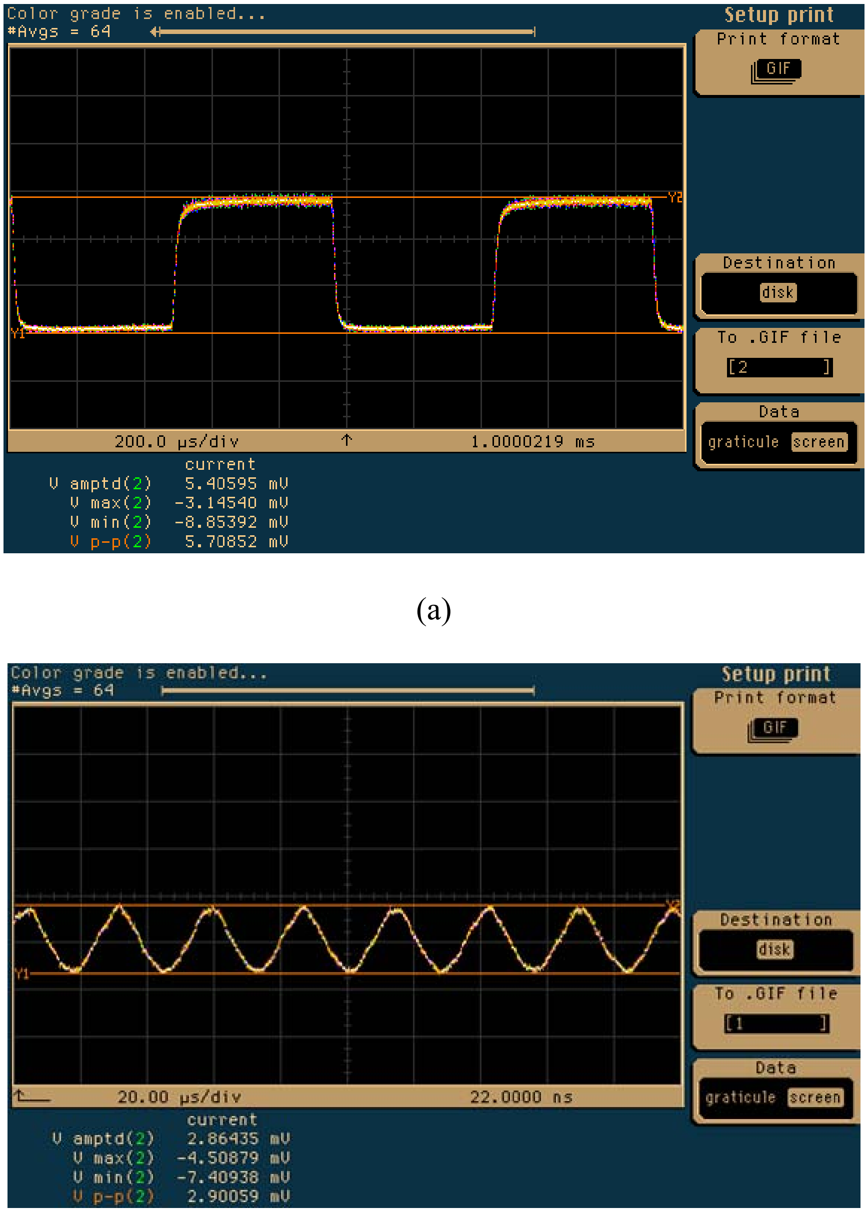

#Avgs = 64

Print format: GIF

Destination: disk

To .GIF file: [2]

200.0 µs/div 1.0000219 ms

```
             current
V amptd(2)   5.40595 mV
  V max(2)  -3.14540 mV
  V min(2)  -8.85392 mV
  V p-p(2)   5.70852 mV
```

(a)

#Avgs = 64

Print format: GIF

Destination: disk

To .GIF file: [1]

20.00 µs/div 22.0000 ns

```
             current
V amptd(2)   2.86435 mV
  V max(2)  -4.50879 mV
  V min(2)  -7.40938 mV
  V p-p(2)   2.90059 mV
```

(b)

Fig. 5.5.3 Modulation traces at (a) 1 kHz and (b) 30 kHz.

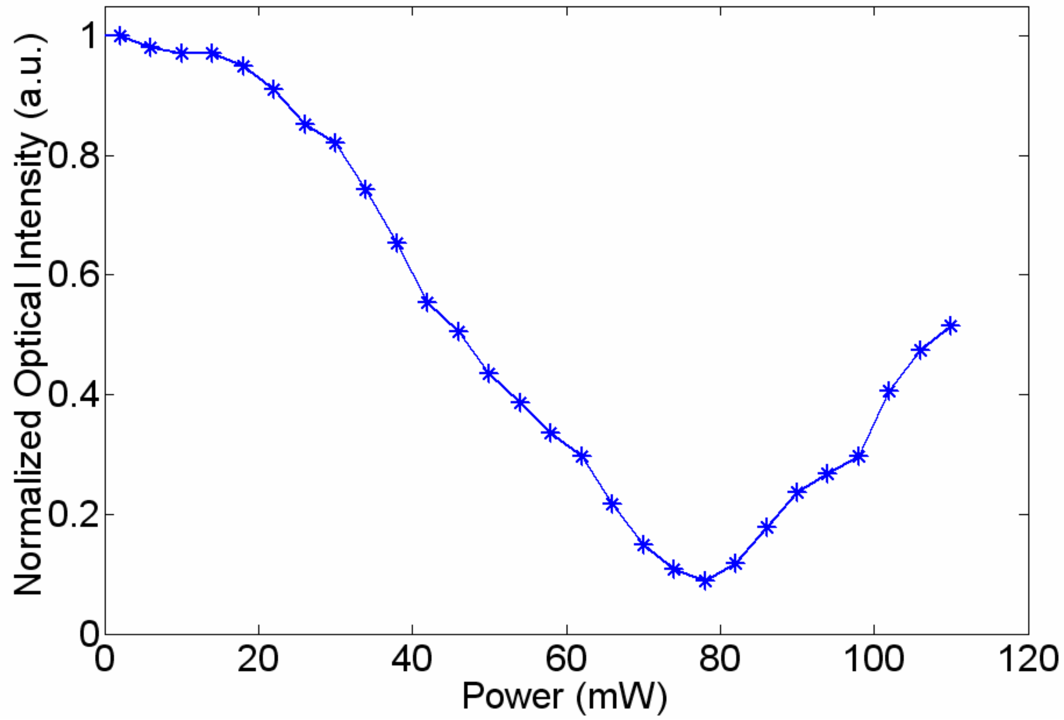

Fig. 5.5.4 Output optical intensity against the applied heating power.

simulation that a small temperature variation of 9 °C was obtained in the line-defect region with the supplied heating power of 70 mW. As already calculated, it would require an active region at least 460 μm for such an amount of temperature increase to achieve a π phase shift in a conventional rib or strip waveguide based silicon TO MZI. Our device has shown almost a one-order of magnitude reduction in the length of the device active region by incorporating PCWs into MZIs. Such a significant size reduction clearly benefited from the slow group-velocity of the PCW.

5.6 Summary

In this chapter, a novel thermal design was proposed for thermo-optically-tuned silicon-on-insulator PCW MZIs. Steady-state and transient thermal analyses were performed to assess the thermal performance of the TO MZI. Carefully designed devices were fabricated and characterized. The switching rise time and fall time were measured to be 19.6 μs and 11.4 μs, respectively, which were substantially lower than those of the reported TO PCW based MZI. Experimental results were in a good agreement with theoretical predictions. A maximum modulation depth of 84% has been obtained for a switching power of 78 mW within an interaction length of 80 μm. Reduction by one order of magnitude in the length of the device active region compared with the conventional silicon rib or strip waveguide based MZIs has been experimentally demonstrated.

Chapter 6

2-D periodic-structure-based device (II):

High-speed p-i-n diode-based photonic-crystal silicon electro-optic modulators

6.1 Introduction

6.1.1 Electro-optic effect in silicon

As discussed earlier, the thermo-optic silicon modulator is rather slow. For high-speed applications in modern telecommunication and computation systems, electro-optic effect is the only effective means to realize high-speed silicon modulators. In 1987, Soref and Bennett studied the refractive index changes in silicon [83] due to the Franz-Keldysh effect, the Kerr effect, and charge carrier effects. They found that for experimentally reasonable values of applied field and injected carriers, the change in refractive index was at least two orders of magnitude larger for the latter. Unstrained pure crystalline silicon has no linear electro-optic (Pockels) effect. However, the second order electro-optic (Kerr) effect exists, and an applied field in the range 10^4-$3x10^5$ V.cm^{-1} produces a change in refractive index (Δn) on the order of 10^{-8}-10^{-5}. Consequently, very high fields are required, which are dangerously close to the breakdown field of silicon.

Another field effect is the Franz-Keldysh effect (also called the electro-absorption or the electro-refraction effect). This effect is important near the energy bandgap. The application of an electric field of 10^4-10^5 V.cm^{-1} tilts the bandgap, which increases the tunneling probability between valence and conduction band. This results in Δn of approximately 1.5 x 10^{-5} in the near infrared for an applied field of 10^5 V.cm^{-1}. The most efficient means of varying the refractive index and/or the optical absorption is by carrier injection/depletion, which has an added advantage of being polarization independent, so it affects the TE and TM modes equally. The classical Drude theory of free-carrier absorption/refraction models the electro/hole plasma as a classical oscillator, ignoring the effects of ionized impurities, and predicts a λ^2 dependence for both the change in absorption and the refractive index. A more accurate index perturbation due to free carriers was quantified by Soref and Bennett who empirically found the refractive index changes as a function of free carriers in silicon via a Kramers-Kronig transform experimental data, which is given by

$$\Delta n = -[8.8\times 10^{-22}\cdot \Delta N + 8.5\times 10^{-18}\cdot (\Delta P)^{0.8}] \ , \qquad (6.1.1)$$

where Δn is the refractive index change, ΔN and ΔP are the variations of free-carrier concentration for electrons and holes, respectively. In fact, almost all of the silicon electro-optic modulators developed thus far have employed this modulation mechanism.

6.1.2 Research status and challenges

As the complementary metal-oxide-semiconductor (CMOS) technology continues to scale down, some physical limitations of conventional metal interconnects, such as bandwidth, power consumption and crosstalk noise, have been the impetus for the investigation of optical interconnects. The global research interest on silicon photonics has increased rapidly in recent years, trigged by the realization of cost-effect monolithic integration of the optical and electrical devices on a silicon platform, using the readily transferred very-large-scale-integrated (VLSI) technology. There has been significant progress in developing silicon low-loss waveguides, light emitters, lasers, amplifiers and photodetectors in the past few years, promising an entry of silicon micro-photonics interconnection at the hybrid, multi-chip level with migration to monolithic on-chip architectures [84]. However, the development of all-silicon electro-optic modulators has been comparatively slow, and they are a key optical interconnection component that encodes information signals onto optical carriers.

Mach-Zehnder interferometer (MZI), which converts a phase modulation to an amplitude modulation, is the most extensively studied modulator structure because of its superior optical performance, such as high-extinction ratio and large bandwidth of the operating wavelength. A historical review of the published work on silicon electro-optic MZIs is given in table 6.1.1. One may find a common problem of those reported devices — very long device interaction length. This on-chip optoelectronic integration

Year	Author	Electrical structure	Frequency bandwidth / Switching time	Length(μm)	
1991[85]	Treyz	p-i-n	50 ns	500	Experimental demonstration
1995[86]	Zhao	p-i-n	200 ns	816	
2000[87]	Dainesi	p-i-n	10 MHz	1000	
2004[64]	Liu	MOS	1 GHz	2500	
2005[88]	Liao	MOS	10 GHz	3450	
2006	Our device	PhC p-i-n	1 GHz	80	
1997[89]	Cutolo	BMFET	3.5 ns	1000	Theoretical prediction
2003[90]	Irace	p-i-n	1 GHz	3000	
2004[91]	Png	p-i-n	0.3 ns	465	
2005[92]	Gan	p-i-n	20 GHz	2500	
2005[93]	Gardes	p^+pnp^+	0.014 ns	2500	
2006	Our device	PhC p-i-n	0.077 ns	80	

Table 6.1.1 Theoretical and experimental work on the silicon Mach Zehnder interferometer modulators published in the earlier literature and our paper.

because the success of monolithic integration relies on the size and density compatibility between the optical and electrical devices. Another property they share is their modulation mechanism — plasma dispersion effect, which describes the refractive index changes corresponding to the electrically-induced variation of free-carrier concentration. Nevertheless, due to the weak response of free-carrier variation to the applied fields, the resulting silicon MZI modulators usually remain large with high power consumption. Besides, the modulation speed is another critical issue worthy of concern. Given the relatively low value of the mobility of both electrons and holes in silicon, the switching speed of the silicon electro-optic modulators is usually slower than the inherently fast III-V based devices. Innovative approaches are needed to conquer these challenges.

In this chapter, we present a gigahertz silicon MZI modulator featuring p-i-n-diode-embedded photonic crystal waveguides. A π phase shift was achieved within an interaction length of 80 μm and under an operation voltage of 2 V. It was predicted that the required interaction length to obtain a π phase shift for a guided mode is proportional to the group velocity in a waveguide [71]:

$$L \approx \frac{1}{2\sigma}\frac{n}{\delta n}\frac{V_G}{c}\lambda_{air} \qquad (1)$$

where σ is the fraction of the total energy of the mode that is stored in the device active region, δn is the perturbation of the material refractive index, V_G is the group velocity of the waveguide, and λ_{air} is the wavelength in air. The significant reduction of the device interaction length was achieved by taking advantage of the unique property exhibited by PCWs — slow group velocity, which was discussed earlier in chapter 5.

Other than the device size, the traditionally slow modulation speed of the silicon MZI modulator could be a serious concern for its practical applications. Although theoretical simulations have predicted that the silicon MZI modulators should be capable of operating in the GHz frequency domain, it was not until recently that Liu et al. [64] and Liao [88] et al. demonstrated real devices with modulation frequency bandwidth exceeding 1 GHz and 10 GHz, respectively. In both works, they used a metal-oxide-semiconductor (MOS) capacitor structure to obtain a charge density modulation within the active region of their MZI modulators, which consequently resulted in an induced modulation in the refractive index and hence an optical modulation. The major problem inherently associated with this structure is the thin thickness of the capacitive charge layer. The thin charge layer leads to a small overlap between the optical field and the index-modulation region. Devices employing this structure may suffer low modulation efficiency and thus require a very long interaction length to obtain the π-phase shift.

In contrast, an embedded p-i-n diode structure appeared to be able to maximize the efficiency of the index modulation. In a p-i-n diode, the injected carriers are usually distributed rather uniformly across the entire intrinsic region, which ensures a uniform index perturbation in the optical wave-guiding region and consequently enhances the modulation efficiency [83, 91]. Moreover, the p-i-n diode structure is inherently simple and very easy to integrate with optical waveguide structures. All of the aforementioned advantages have made it the most popular choice to realize silicon electro-optic modulators. Nevertheless, the p-i-n diode-based modulators have been considered slower than the MOS based modulators. Their speed is limited by the comparatively slow carrier injection and/or recombination process. Simulations indicated that reducing the thickness of the waveguide core layer of a silicon modulator might increase the switching speed

[90]. In conventional integrated silicon modulators, where the p-i-n diode is integrated with a rib waveguide, the thickness of the core layer is usually a few microns [85-87]. In contrast, the core layer of a silicon photonic crystal waveguide generally falls between 200nm and 300nm, which is a promising feature for speed enhancement. Optimization of driving signal assists in speed enhancement of silicon modulators. The switching behavior of the p-i-n diode adopting a novel biasing strategies was also explored.

6.2 Device electrical design using MEDICI

A two-dimensional semiconductor device simulator MEDICI was used to model our p-i-n devices. This simulator predicts the device characteristics by using the finite element method to solve the coupled Poisson's equation and charge continuity equations. Advanced physics device models are included with the simulator. In our simulation, carrier recombination models including doping concentration dependent Shockley-Read-Hall recombination and Auger recombination were adopted to account for the key physical processes in our device. The impurity concentration and field dependent carrier mobility was also specified in our device modeling. The schematics of the perspective view and the cross-sectional view of our p-i-n diode-based PhC silicon MZI are shown in Fig. 6.2.1 (a) and (b).

The p-i-n diode was implemented on a SOI wafer, which has a top silicon layer of 230 nm and an underlying buried oxide layer of 2000nm. A thick buried oxide layer was chosen to ensure a sufficiently good optical confinement of silicon waveguides. Ideally, the highly doped regions should stay far away from the optical mode to prevent additional absorption loss. However, increasing the width of the intrinsic region will slow down the carrier injection and thereby limit the device switching speed. We considered this inherent tradeoff and selected a balanced value of 4 μm for the

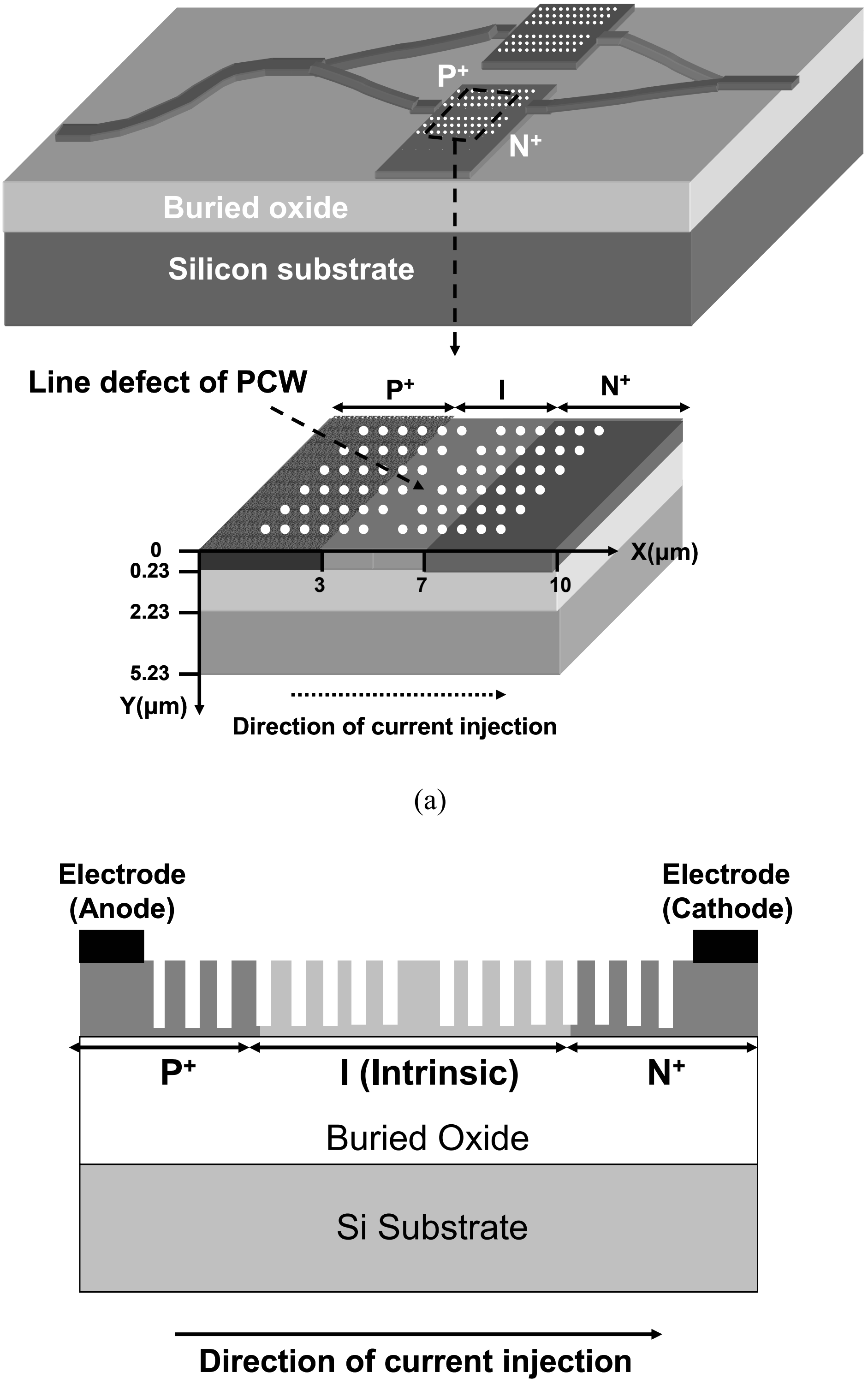

(a)

(b)

Fig. 6.2.1 Schematics of p-i-n diode-based photonic crystal Mach Zehnder interferometer: (a) perspective view; (b) cross-sectional view.

separation width based on the earlier simulation results, which is presented in chapter 5, section 5.2. We also assumed the width of both the P+ and N+ regions were 3 μm. The intrinsic region has an n-type background doping of 10^{15} cm^{-3}. A constant doping profile with a concentration of $5x10^{19}$ cm^{-3} was assumed for both P+ and N+ regions. We first evaluated switching characteristics of the p-i-n diode under a turn-on voltage (V_{on}) of 0.89 V and a turn-off voltage (V_{off}) of 0 V. The rise time (t_{on}) and fall time (t_{off}) of the current injection were defined as the time required for the injected current to swing between 10% and 90% of its maximum value. A rise time of 3.5 ns and a fall time of 1 ns are observed, as depicted in Fig. 6.2.2. One may note that the fall current is slightly larger but still stay in the same order of the rise current. Simulation showed that a reverse fall current appeared once the applied voltage stepped down from V_{on} =0.89 V to V_{off}=0 V. The temperature increase due to this comparatively high reserve current was imperceptible in the device thermal analysis. Simulations showed that a saturated carrier filling of $3x10^{17}$ cm^{-3} in the intrinsic region can be obtained with a minimal static bias of

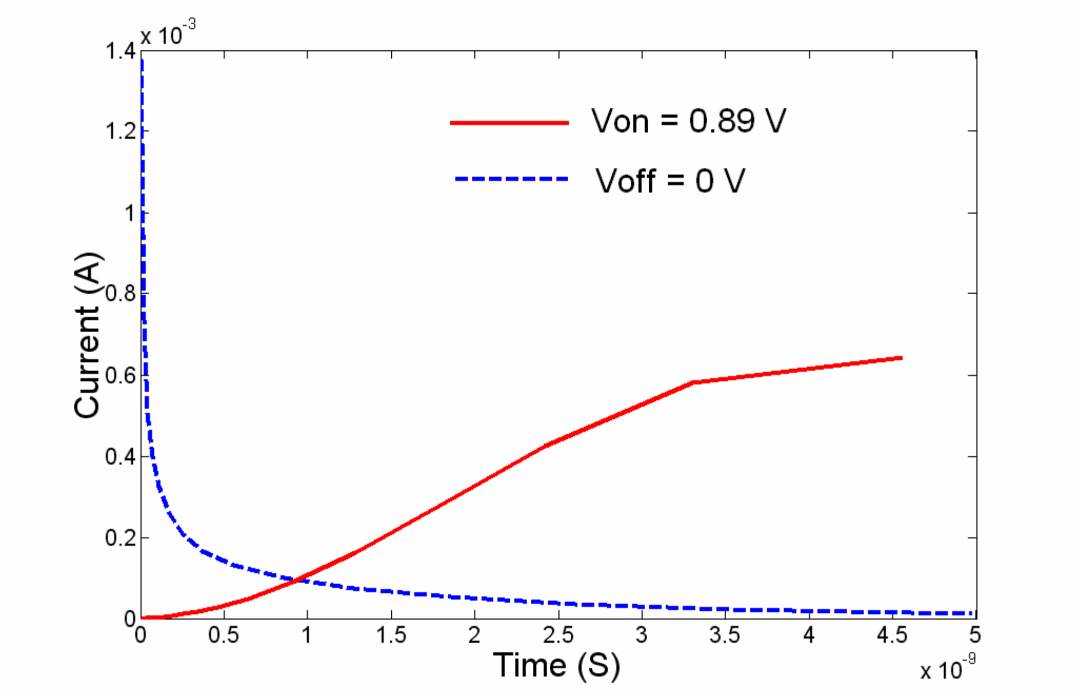

Fig. 6.2.2 Transient characteristic of the p-i-n diode under a turn-on voltage at 0.89 V and a turn-off voltage at 0 V.

0.89 V. Simulated time-dependent carrier filling across the lateral dimension of the entire diode region for both minority carriers (holes) and majority carriers (electrons) are shown in 6.2.3. As is clearly evident from the graphs, the injection of both carriers into the intrinsic region is fairly uniform. It leads to a two-dimensional uniform refractive index modulation over the whole area of the optical channel. There is carrier injection level of 3 x 10^{17} cm^{-3}, which corresponds to a refractive index variation of 0.001, is attained at 6.78 ns after turning on the diode that the carrier filling in the intrinsic region got saturated at. In fact, this filling level is a commonly targeted value ensuring a device length shorter than 1mm [85-87, 89-91]. However, the major concern with this design is its long response time. Fortunately, this problem can be solved by slightly modifying the driving signals, while leaving the original design structure unchanged.

As discussed earlier, the switching speed of a p-i-n diode is mostly limited by the carrier injection (diffusion) and/or carrier recombination process. It was predicted that over-biasing the device junction at the turn-on state enables a faster filling of the free carriers into the intrinsic region of p-i-n diode [90], while a reverse bias at the turn-off state would result in a faster extraction of the injected free carriers [94, 96]. The switching behavior of a p-i-n diode under such a unique combination of over-biasing (at the on state) and reverse-biasing (at the off state) conditions was explored. It is found in Fig. 6.2.5 that the rise time of the diode is reduced from 3 ns to 0.7 ns by increasing the forward voltage from 0.89 V to 2 V, and the fall time is reduced by half if a reverse bias of -1 V in stead of 0 V is applied at the off state. It was reported that the speed of p-i-n diode is mostly limited by the slow filling process since the extraction of free carriers under the reverse-biasing condition can be very fast [90, 94, 97]. We therefore simulated the time response of carrier filling into the diode. Note that the distributions vary insignificantly across the depth of the top silicon layer. The plotted data were taken along a line located at the half depth of the top silicon layer. To obtain a more straightforward insight, variations of the free-carrier concentration extracted from the simulation results were subsequently converted to the refractive index changes using equation (1). As is seen in Fig. 6.2.6, it only takes 0.58 ns to reach a filling level of 3 x 10^{17} cm^{-3} (corresponding to an index change of 0.001) over the whole intrinsic region. One may note that the injection current does not saturate within 2 ns after turning the diode on.

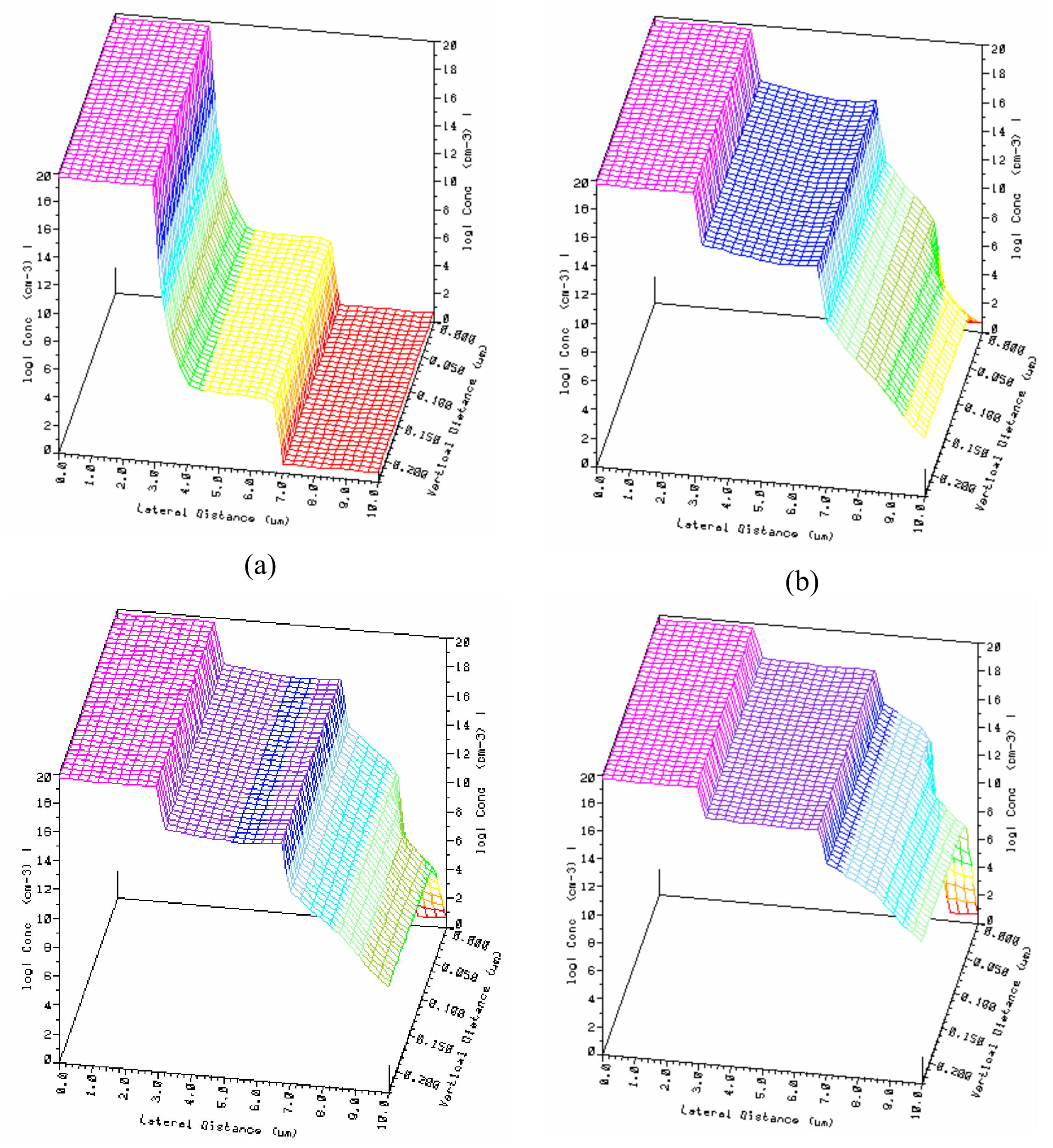

(a)

(b)

(c)

(d)

Fig. 6.2.3 Two-dimensional distributions of hole concentration under 0.89 V at: (a) of t = 0 ns; (b) at t = 0.89 ns; (c) t = 2.26 ns; and (d) t = 6.78 ns.

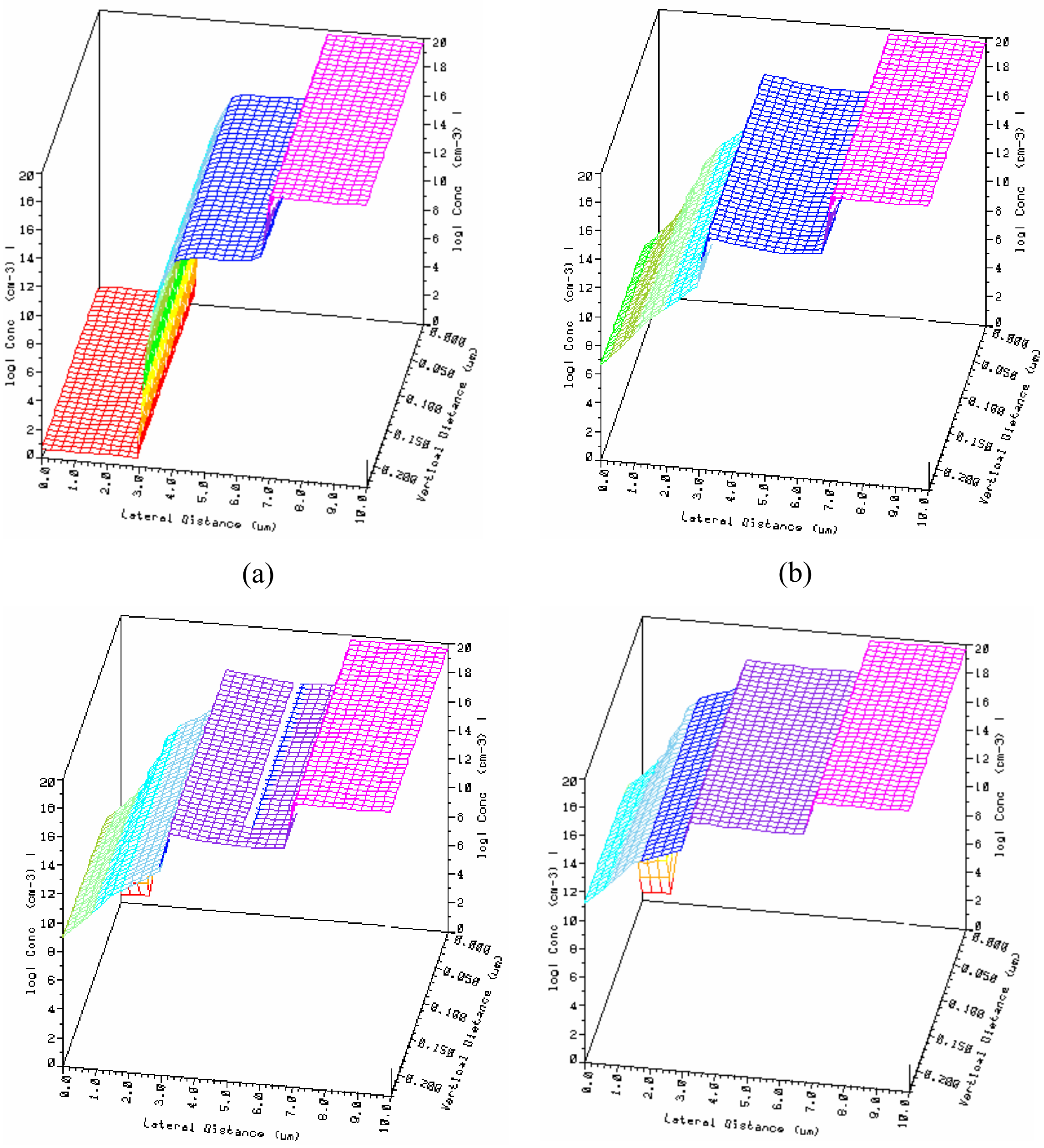

(a) (b)

(c) (d)

Fig. 6.2.4 Two-dimensional distributions of electron concentration under 0.89 V at: (a) of t = 0 ns; (b) at t = 0.89 ns; (c) t = 2.26 ns; and (d) t = 6.78 ns.

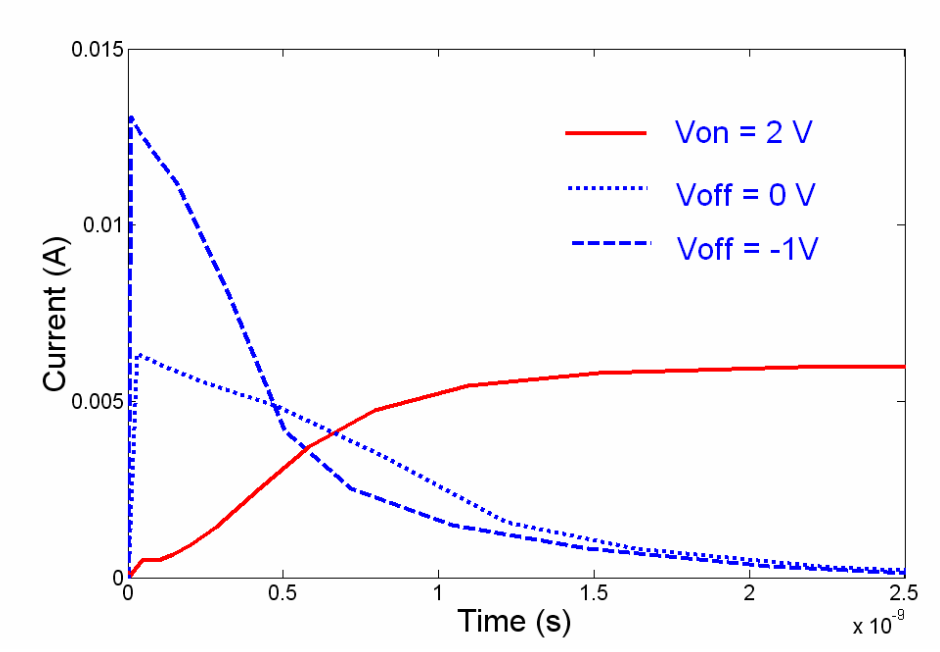

Fig. 6.2.5 Transient characteristics of the p-i-n diode with a intrinsic width of 4 μm under a turn-on voltage at 2 V and turn-off voltages at 0 V and -1V, respectively.

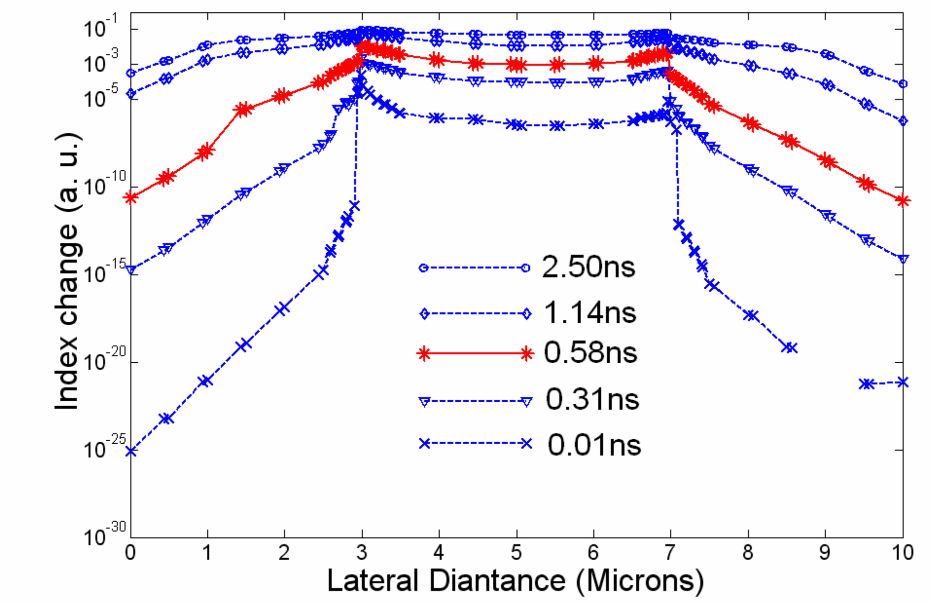

Fig. 6.2.6 Time-dependent variation of the refractive index along the lateral dimension of the p-i-n diode with a 4-μm-wide intrinsic region upon the voltage steps on from V = -1V to V = 2 V.

However, if an index change of 0.001 is the targeted value to switch the optical modulation, as is the case for most developed p-i-n based silicon MZIs, the relatively long rise and fall times of the current injection are no longer the limiting factors for the optical response of the silicon modulator. In other words, the optical response of the optical modulator could be much faster than the electrical switching speed of the p-i-n diode if the device operates under the so-called un-saturation condition. Particularly in the PCW based silicon modulator, a much smaller index change at a much lower injection level might be sufficient to switch the device due to the extremely small group velocity exhibited by PCWs. It indicates that the PCW based modulator we proposed could operate much faster than the conventional device depending on how much the index change is required for the operation. Therefore, we can confidently predict that the designed 4-μm–wide structure is capable of modulating optical signals above 1 GHz.

Reducing the width of the intrinsic region could be an effective way to further increase the switching speed, though it could also cause extra optical loss. As we analyzed earlier, the separation distance of the highly doped regions should stay wider than 1.5 μm to avoid otherwise inevitable free carrier absorption induced extra optical loss of the waveguide. As found in Fig. 6.2.7, the rise time is reduced a significant amount to 0.15 ns. The time response was simulated for the carrier filling along the lateral dimension of the device which has a W_I of 1.5 μm. Fig. 6.2.8 shows the correspondent time-dependent spatial change in the refractive index of the silicon core layer. A significant decrease in the carrier filling time was observed in this shrunk structure. Within 0.077 ns after turning on the device, a reasonably uniform index change of 0.001 was attained in the intrinsic or the wave-guiding region. This is almost 10 times faster than the 4-μm-wide structure. Therefore, it is reasonable to expect that the modulators employed such a 1.5-μm–wide structure can excel the modulations in the 10 GHz region.

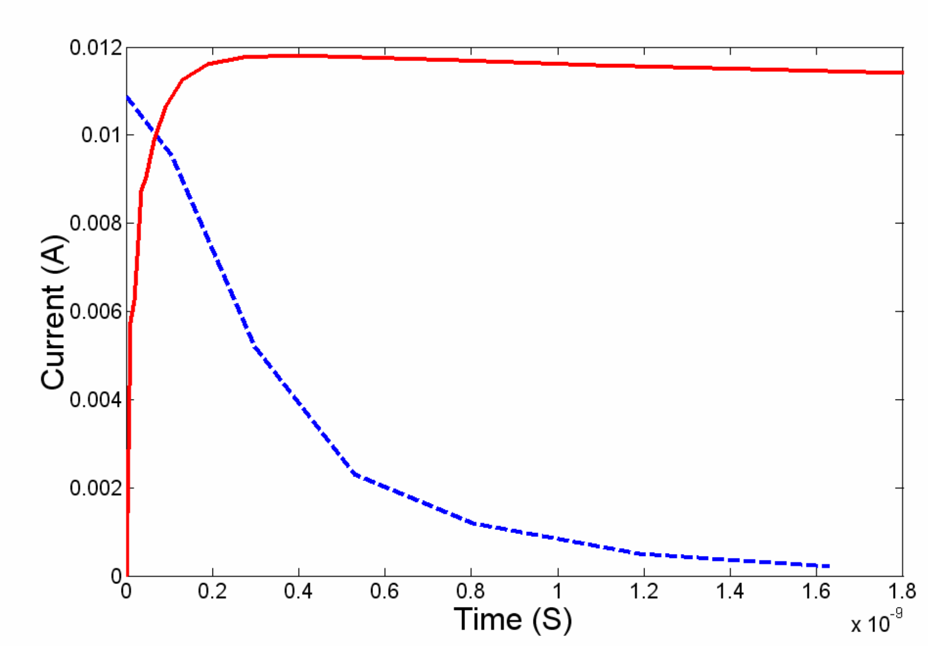

Fig. 6.2.7 Transient characteristics of the p-i-n diode with an intrinsic width of 1.5 μm under a turn-on voltage at 2 V and turn-off voltages at 0 V and -1V, respectively.

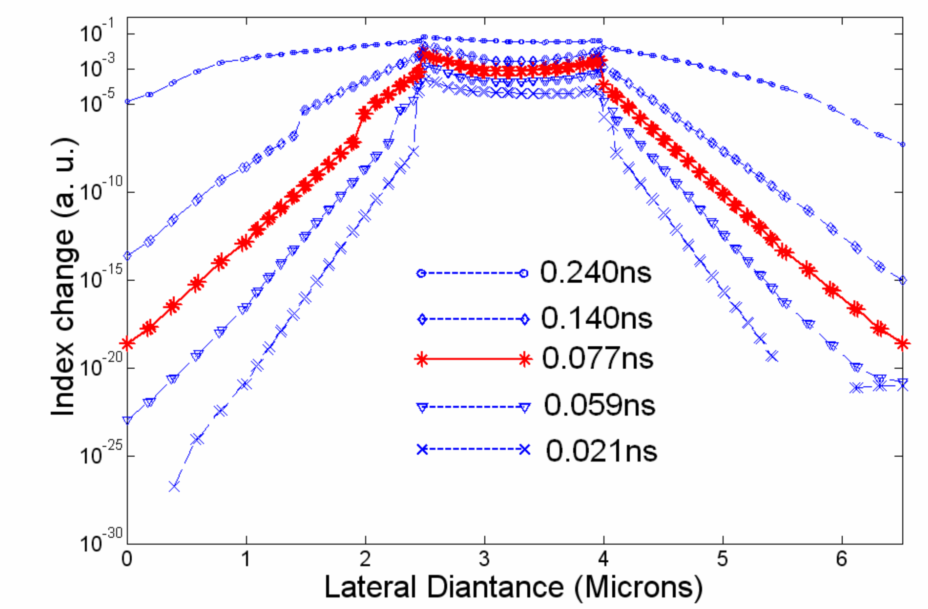

Fig. 6.2.8 Time-dependent variation of the refractive index along the lateral dimension of the p-i-n diode with an intrinsic region of 1.5 μm upon the voltage steps on from V = -1V to V = 2 V.

6.3 Device fabrication

Considering the complication of fabrication procedures, we employed the previously simulated 4-μm-wide rather than 1.5-μm-wide p-i-n diode structure to construct our silicon PhC MZI modulators. A silicon-on-insulator (SOI) wafer with the top silicon layer of 260 nm and a buried oxide layer of 2 μm was selected as the device substrate. A thermal oxide of about 80 nm, grown at 850^{o}C in H_2O atmosphere, served as an etching mask for silicon reactive ion etching (RIE). In addition, this thin oxide worked as a screen layer to minimize the channeling effect occurring in the ion implantation. The device structure using the previously simulated lattice parameters was defined by electron-beam lithography. Device patterns were transferred to the oxide layer by RIE using $CHF_{3.}$ We then stripped off the electron-beam resist with a heated Pirahna (solution of sulfuric acid and hydrogen peroxide) cleaning. The device structure was then defined on the silicon core layer by RIE to a depth of 230 nm, using oxide as the hard mask. The windows for P^{+} and N^{+} implantation were opened by photolithography. Ion implantations of Boron at 30KeV and Phosphorus at 50KeV were performed to achieve an average doping concentration about 5 X 10^{19} cm^{-3} for highly doped N^{+} and P^{+} regions. The thermal rapid annealing for 1 minute at 950^{o} in a flowing nitrogen environment was performed afterwards to anneal the lattice defects and activate the implanted atoms. Electrode contact windows were then opened by photolithography and the top thermal oxide inside the windows was removed. Aluminum electrodes were made by electron- beam evaporation and a subsequent lift off process. Finally, a good ohmic contact between the aluminum electrodes and the underlying silicon was formed by sintering the device at a temperature of 400^{o} C for 30 minutes in a forming gas ambient. Finally, a polymer layer was coated to cover the whole device, which functioned as the top cladding of silicon waveguides and as a mechanical protection layer. The microscopic image of the resulting device is shown in Fig. 6.3.1. Care was taken to the geometry design of the highly doped regions and electrodes. Our early experiments, in which the fabricated P+ and N+ regions were longer than the PCW, showed that the photonic crystal p-i-n diode tended to break down at the two ends of a PCW, as is shown in Fig. 6.3.2.

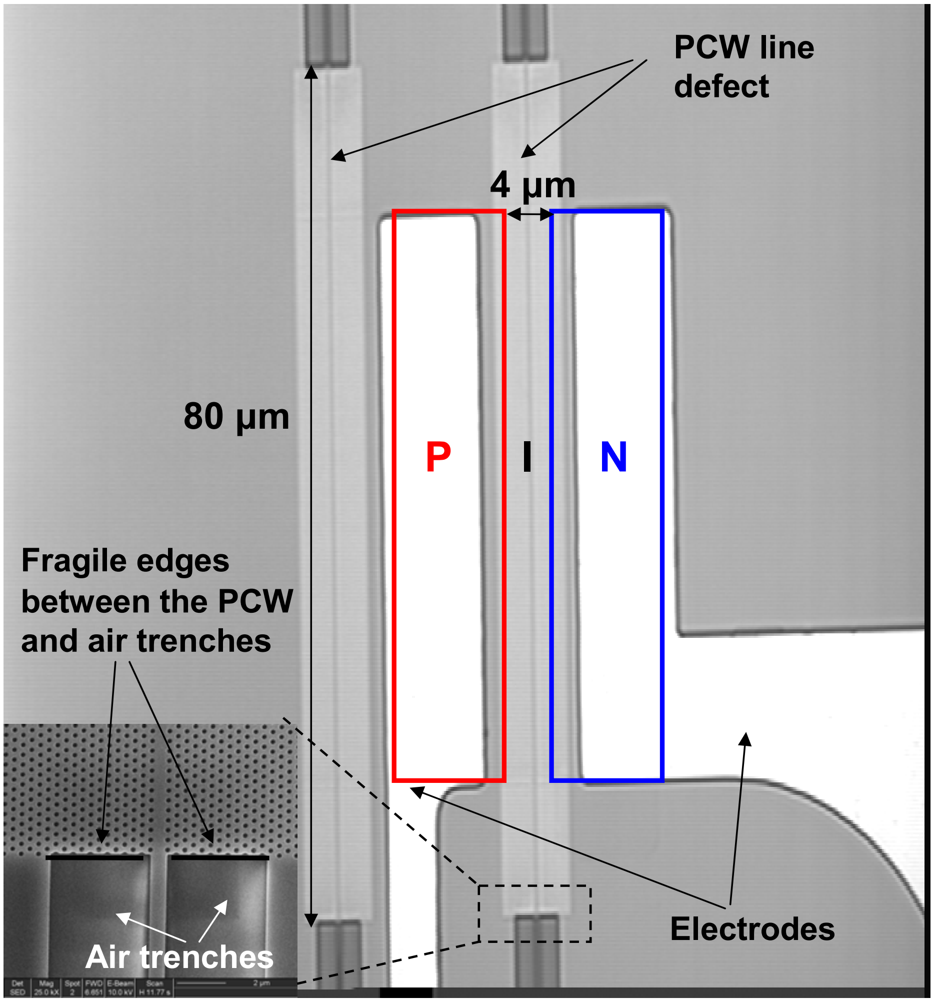

Fig. 6.3.1 Top-view of microscopic image of the p-i-n diode-based photonic crystal silicon Mach Zehnder interferometer modulator.

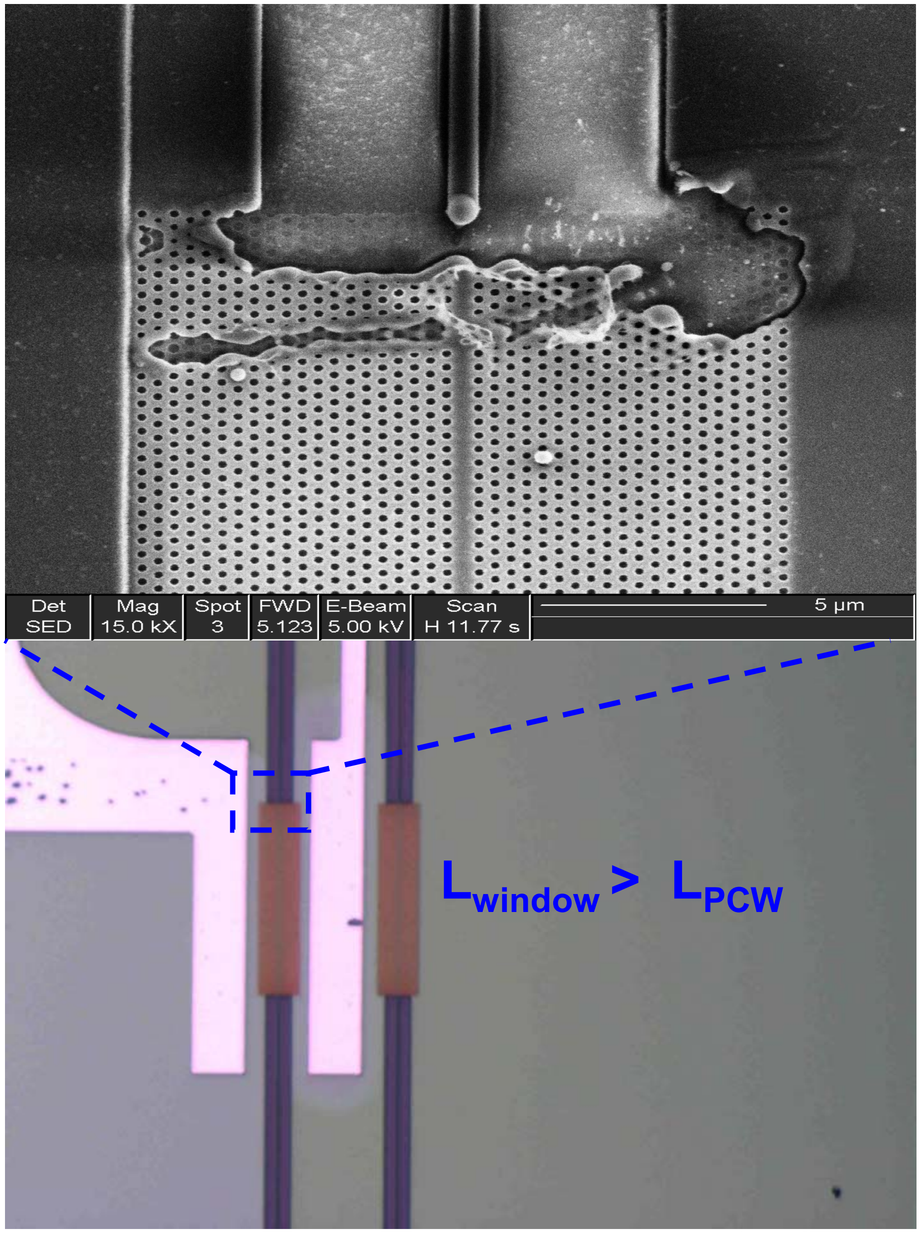

Fig. 6.3.2 Illustration of the electrical breaking-down in a device where the fabricated P+ and N+ regions were longer than the PCW.

This reliability issue was determined to be associated with the highly concentrated electrical field and electrical current density localized at the edge of PhCs. To avoid the generation of the dense current along the edges of PhCs, we shortened the length of the highly doped P^+ and N^+ regions. The reliability advantage of such an electrical design has been confirmed in the measurements.

6.4 Device characterization

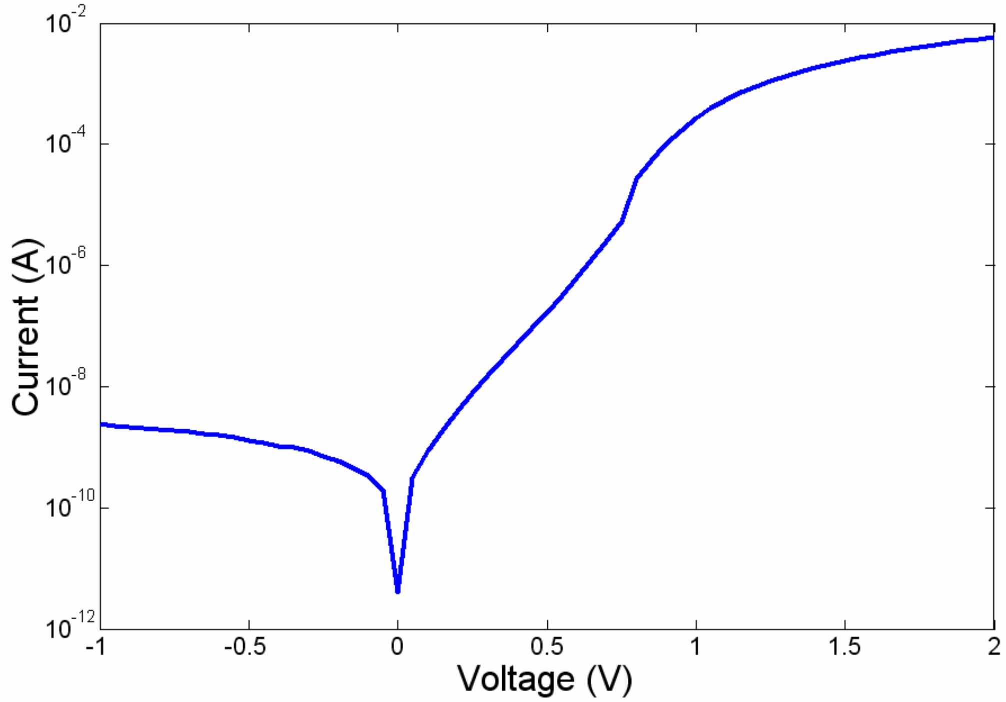

Fig. 6.4.1 I-V characteristic of photonic crystal p-i-n diode.

The I-V characteristic of our PhC p-i-n diode was measured and plotted in Fig 6.4.1. No major difference has been found in its electrical performance compared with the conventional p-i-n diode. The optical characterization of the p-i-n diode-based MZI modulator was performed on a fully-automated Newport Photonics Alignment/Packaging Station. The set-up of optical measurement is shown in Fig. 6.4.2. To minimize the parasitic capacitance and resistance which are most likely to degrade the device high-speed performance, we applied voltage between the cathode and anode of the device at a minimal distance, which is shown in Fig. 6.4.3. Transverse electric (TE) – polarized light at a wavelength of 1541nm was used for optical measurements. Polarization maintaining (PM) fibers with a lensed taper-end were used to couple the light to and from the modulator. An Agilent 8133A pulse generator (up to 3 Gbit s^{-1}) was used to generate the electrical driving signals. Modulated optical signals were detected by a 30-GHz photodetector which is internally integrated with the HP 83480A digital communication analyzer. The optical intensity at the device output as a function of applied current was plotted in Fig. 6.4.4. A maximum modulation depth of 93% was obtained at a static injection current of 7.1 mA. Square wave electrical signals at a peak-to-peak voltage of

Fig. 6.4.2 The set-up of optical measurements.

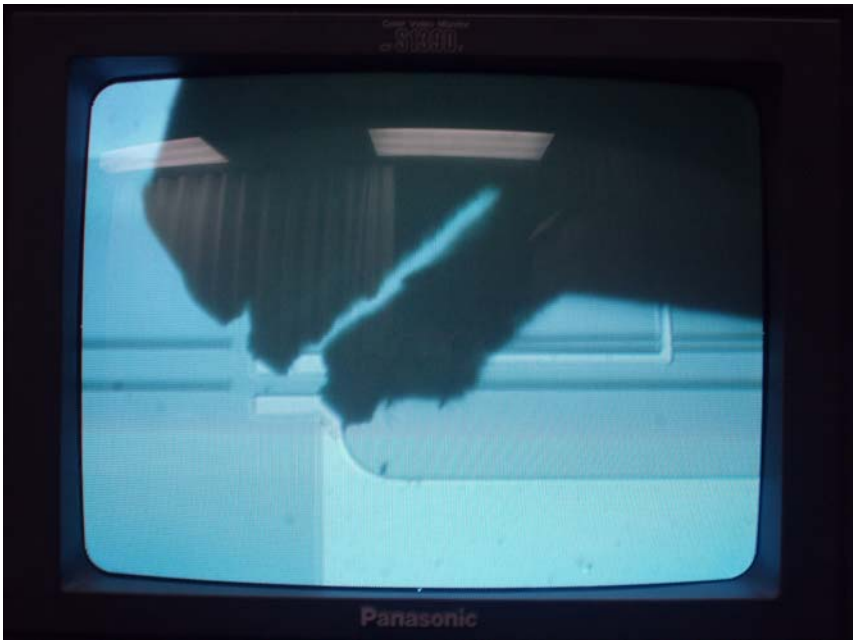

Fig. 6.4.3 The microscope image of the high speed probes which are connected to the cathode and anode of the p-i-n diode.

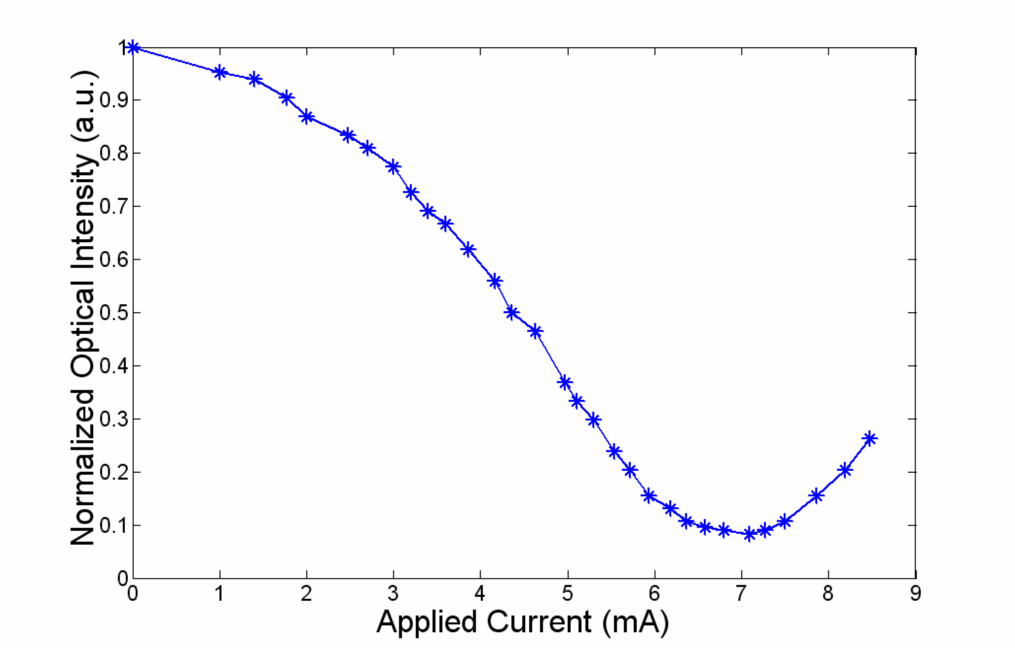

Fig. 6.4.4 Optical intensity at the device output as a function of applied current.

3V ($V_{\text{on}} = 2$ V, $V_{\text{off}} = -1$) with a duty cycle of 50% were used for dynamic modulation characterization. Dynamic modulation was also characterized. Fig. 6.4.5 shows the optical modulation traces at various bit rates.

One may note a very interesting phenomenon of how the waveform of the modulated signal evolves with the modulation frequency. The waveform of the modulated optical signal is severely distorted accompanying with a reduced modulation depth as the electrical plus rate increases to a few hundreds Kbit s^{-1}. However, the shape of modulation signals fully recovers when further increasing the modulation frequency, up to a few MHz. We believe this phenomenon is related to the competition between the entangled electro-optic and thermo-optic effects. As current injection is always associated with power dissipation, the thermal effect is always presented in the p-i-n diode. Heating increases the refractive index, in contrast to the free carrier injection which reduces the refractive index. However, the thermal response is much slower than the electrical response. The thermo-optic effect can only work up to a few hundreds of kHz [87, 98] and consequently it tends to compete with the plasma dispersion effect only at a low-frequency operation. The modulation traces shown in Fig. 6.4.5 indicate that for a very low frequency operation, the thermo-optic effect dominates the modulation mechanism in our device. However,

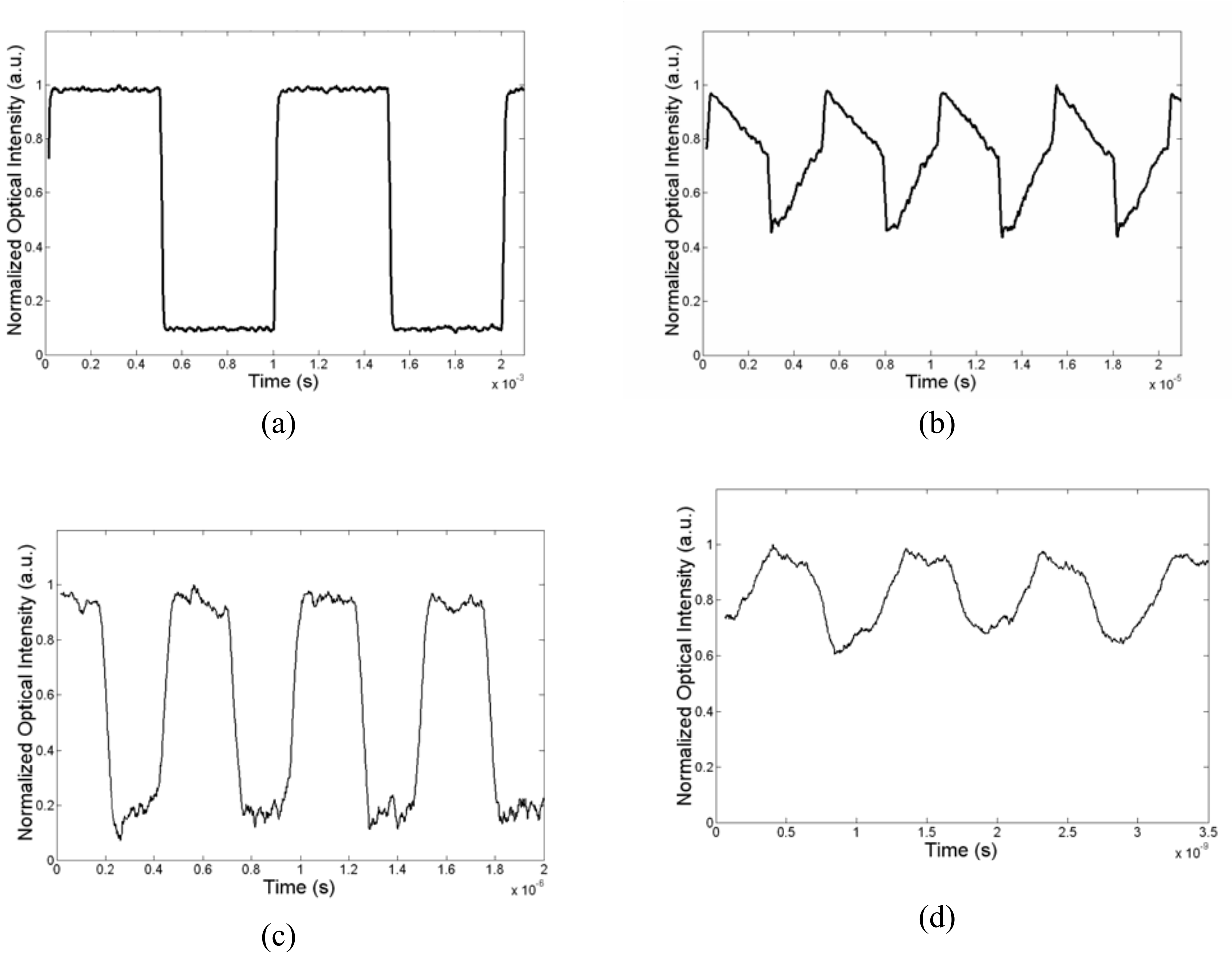

(a)

(b)

(c)

(d)

Fig. 6.4.5 Modulation traces of the p-i-n diode-based photonic crystal silicon modulator at a pulse bit rate of (a) 1 Kbit s^{-1} ; (b) 200 Kbit s^{-1} (c) 2 Mbit s^{-1}; (d) 1 Gbit s^{-1}.

such a dominance become weaker when the frequency increases, because the increasing modulation speed is hard to catch up with for the heating process. A severe degradation of the modulation signal at 200 Kbit s^{-1}, shown in Fig. 6.4.5 (b), suggested a strong competition between the thermo-optic and electro-optic effects at a corner frequency of the thermal response region. As the frequency further increases to above a few MHz, the thermo-effect is no longer able to pick up such a fast switching speed, and carrier injection takes over the task and begins to predominate the modulation mechanism. To make electro-optic modulation more efficient, a good thermal heat sink has to be designed to minimize the competition from thermo-optic effect. We believe the demonstrated modulation at 1 Gbit s^{-1} is purely due to the electro-optic effect, although there must be some degradation due to r.m.s. current heating.

A high dynamic modulation depth of 85% at 2 Mbit s^{-1} has been obtained. The modulation depth is reduced by 3-dB as the modulation frequency increases to 1 Gbit s^{-1}, which marked the 3-dB bandwidth of our device. To our best knowledge, our device is the fastest p-i-n diode-based MZI silicon modulator ever developed. The interaction length of our device is over 30 times shorter than the MOS capacitor based silicon MZIs [64] and over 10 times shorter than the conventional p-i-n diode-based EO MZIs [85-87]. Our device is also believed to be the most compact p-i-n diode-based MZI silicon modulator ever reported. We also believe that the current high-speed performance of our device is mostly limited by the performance of the uncustomized drive circuitry, not by the intrinsic capability of the device itself. We anticipate the device to perform excellently in the GHz frequency region through a specifically designed high-speed drive circuitry. Further speed improvement can be achieved using the shrunk p-i-n diode we proposed earlier.

6.5 Recommendations for future work

Future work in this project may aim to further scale down device size and boost device speed accordingly. The device presented in this chapter was developed in a hybrid configuration, in which the conventional stripe-waveguide-based 3 dB y-junction splitter was employed in conjunction with photonic crystal waveguide to construct the Mach-Zehnder interferometer structure. The angle of a y-junction splitter is usually in the range of a few degrees, which results in a comparatively long y-branch length against a given separation distance between two arms of a Mach-Zehnder interferometer. Increasing the splitting angle helps reduce the entire device length, however, at the expense of high optical loss. Studies have shown that light can propagate in the bended line-defect photonic crystal waveguide with nearly 100% transmission in certain frequency regions. It is easy to introduce a 60 ° and 120 ° bends into a triangular lattice crystal. Thus, it will be possible to generate sharp brand and 3 dB splitter of several μm in length [99-101] in photonic crystal structure, which leads to a significant reduction of the footprint of all-photonic-crystal Mach-Zehnder interferometers. Through our initial efforts, all-photonic-crystal passive Mach-Zehnder interferometers have been successfully fabricated, as shown in Fig. 6.5.1 (c) and (d). In the future work, structural optimization of the bends and y-junctions in the Mach-Zehnder interferometers should be performed to lower the optical loss of passive Mach-Zehnder interferometers.

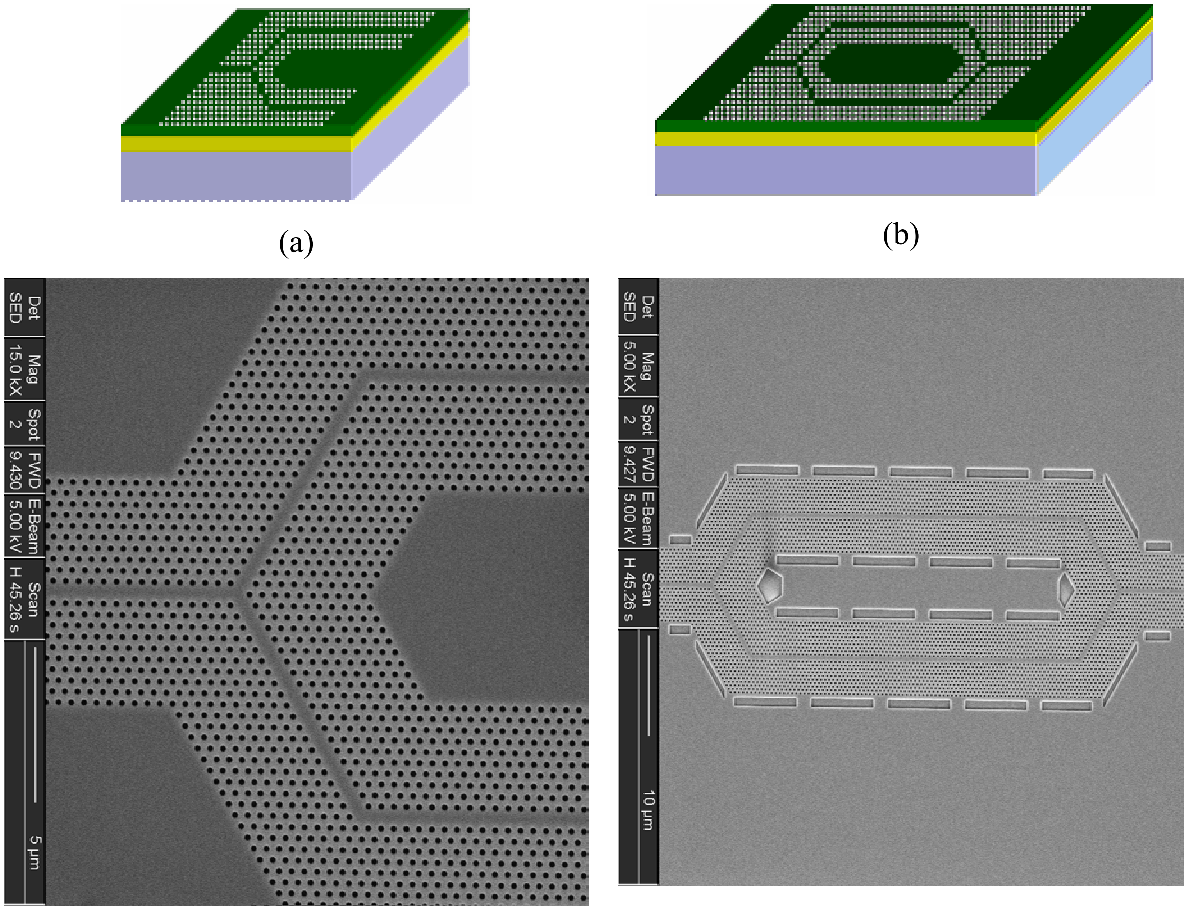

(a) (b)

(c) (d)

Fig. 6.5.1 All-photonic-crystal wave-guiding elements: (a) schematic of all-photonic-crystal Y-junction (splitter); (b) schematic of all-photonic-crystal Mach-Zehnder Interferometer; (c) SEM of all-photonic-crystal Y- junction; (d) SEM of all-photonic-crystal Mach-Zehnder Interferometer.

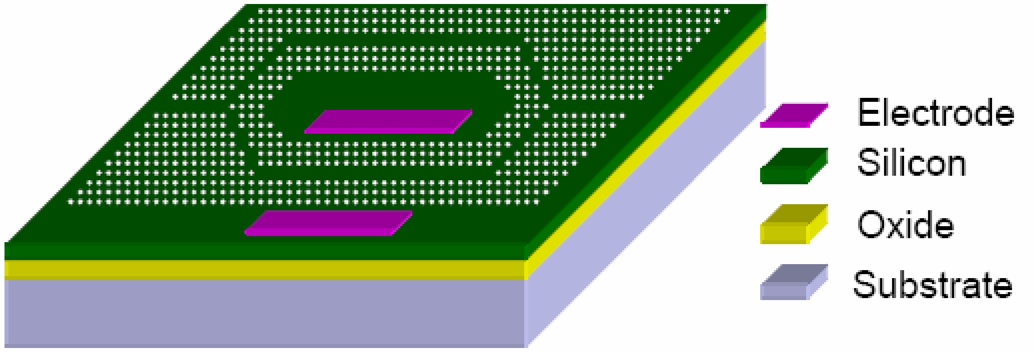

Fig. 6.5.2 All-photonic-crystal MZI with the horizontal electrode.

For an all-photonic-crystal Mach-Zehnder modulator with the horizontal electrode structures, as illustrated in Fig. 6.5.2, there is always a need to use metal wire to connect the electrode placed between the two arms to the chip edge for wire bonding. If the metal wire directly passes over the other photonic crystal waveguide, extra optical loss will occur in the other waveguide. This further causes asymmetry of optical intensity of two arms, which reduces the extinction ratio of the Mach-Zehnder modulator. To solve this problem, a vertical inter-layer electrical interconnection scheme should be employed to provide electrical routing to the substrate, which serves as the ground electrode. Essentially, an electrical via will be formed to penetrate the bottom oxide and connect one electrode to the substrate. A sequence of processes will be developed to form a via and its electrical characteristics will be tested.

A further improvement in device modulation speed could be achieved utilizing the depletion-mode operation of a p^+pnn^+ based modulator [93]. The rise time and fall time of the proposed device in reference [93] are both calculated to be 7 ps for a reverse bias of 5 V. The proposed device employed a conventional stripe-waveguide based vertical electrical structure, as shown in Fig. 6.5.3 (a). Our future research may consider incorporating a lateral p^+pnn^+ electrical structure into the photonic-crystal silicon modulator. The lateral structure brings various advantages in terms of the fabrication, wiring and packaging complications. In addition, optical loss may be lower in a lateral structure than in a vertical structure, because the extra absorption loss due to high-density free carriers in the p^+ and n^+, which is inevitably presented in the vertical structure, could be minimized in a lateral device.

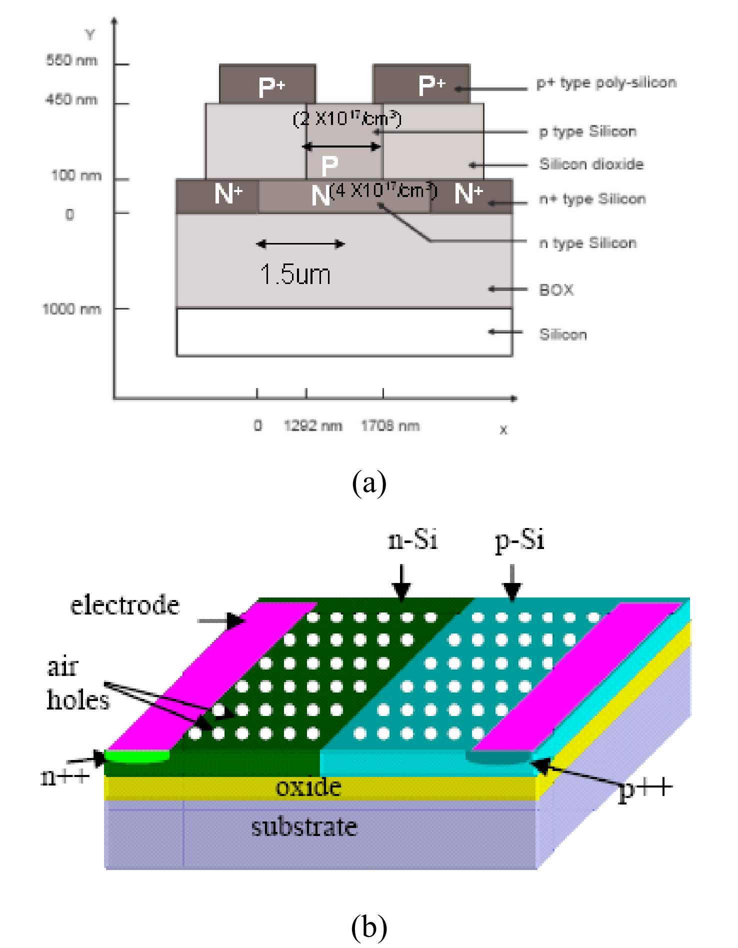

(a)

(b)

Fig. 6.5.3 Schematics of (a) vertical [93], and (b) lateral structure of the p^+pnn^+ based modulator.

6.6 Summary

In this chapter, the design, fabrication and characterization of a p-i-n diode-based photonic crystal silicon modulator, which operates in the GHz region, is presented. The incorporation of photonic crystal waveguides into a Mach-Zehnder interferometer enables a significant reduction in device interaction length. The physical mechanism of such an ultra-compact and high-speed device has been analyzed. Optical simulation using the plane wave expansion method has been performed to study the slow group velocity of the photonic crystal waveguide. To provide a guideline for the geometry design of the embedded p-i-n diode, optical mode profile of the photonic crystal waveguide was simulated. The two-dimensional semiconductor device simulator MEDICI has been employed to investigate the electrical performance of our devices. The switching behavior and time-dependent carrier injection of the embedded p-i-n diode were theoretically analyzed. A novel strategy of driving signal, which combines an over-bias turn-on voltage and a reserve-bias turn-off voltage, was proposed. The resulting improvement in device speed was experimental confirmed. I-V curve of an embedded photonic crystal p-i-n diode, which has a 4-μm-wide intrinsic region, was measured for the first time. High-speed optical modulation at 1 Gbit s^{-1} of the same device has been experimentally demonstrated. We believe the reported device is the fasted p-i-n based silicon MZI modulator ever developed. Furthermore, the feasibility of demonstrating even higher modulation speed up to 10 GHz in a shrunk device has been theoretically proven.

Chapter 7

Summary

This doctoral research focused on the investigation of one-dimensional and two-dimensional periodic-structure-based optical devices, extending from volume-grating-based wavelength-division-multiplexing (WDM) devices and Raman-Nath grating based liquid crystal beam steering devices, to photonic-crystal based silicon Mach-Zehnder interferometer (MZI) modulators.

A new application of coarse WDM for optical inter-satellite links was introduced. A four-channel CWDM was designed and fabricated for applications in both current medium bit rate (300 Mbits/s) systems based on 0.8 μm technology and future high bit rate (1.2 Gbits/s) systems based on 1.5 μm technology. This broad-band four-wavelength CWDM provided two data streams channels at 0.83 μm and 1.55 μm, one inter-satellite tracking channel at 1.06 μm, and one intra-satellite communication channel at 1.34 μm. This was the first time that a WDM device was designed and fabricated to cover such a large wavelength range in a single substrate. Surface-normal fan outs and 8mm physical separation between adjacent channels were designed to facilitate the output coupling and packaging. The features of small size and light weight made this CWDM device quite attractive for space-borne applications due to the requirements of low weight and volume.

A universal solution to solve the intrinsic tradeoff between the dispersion capacity and the efficiency bandwidth of a volume holographic grating was proposed. By using a pre-staged grating in front of a dispersion-enhanced grating, a very significant enhancement of the 3dB efficiency bandwidth can be achieved due to the phase compensation of the Bragg condition. The phase-compensation scheme was demonstrated by using the $45^o/82^o$ configuration. A 21-channel dense WDM device centered at 1555 nm with 200 GHz spacing was achieved within a 3dB bandwidth.

A two-level liquid crystal (LC) grating working at 1.55 μm was proposed and fabricated. By applying a unique biasing configuration to a double-sided structure, the distortion of the LC directors due to the fringing-field effect was significantly suppressed, which led to a much larger phase modulation depth and higher diffraction efficiency. A diffraction efficiency of 33% at the first order diffraction angle of 14.5^{o} was experimentally achieved. The efficiency has been enhanced 80 times compared with the conventional structure, which approaches the theoretical limit. Experiments have confirmed that no significant performance degradation occurs under an electrode misalignment of 2 μm. For the current device to work as a programmable grating, a common method is to selectively activate a subset of electrodes, whose pitch p is a multiple of the fundamental pitch p_0. Our structure ensures that the programmed state with the smallest p (=p_0) and therefore the worst fringing-field effect has high phase modulation depth. The other states are generally better, which was confirmed by simulations.

A novel thermal design was proposed for thermo-optically-tuned silicon-on-insulator photonic crystal MZIs. Steady-state and transient thermal analyses were performed to assess the thermal performance of the thermo-optic (TO) MZI. Devices were fabricated and characterized. The switching rise time and fall time were measured to be 19.6 μs and 11.4 μs, respectively, which were substantially lower than those of the reported TO PCW based MZI. Experimental results were in agreement with theoretical predictions. A maximum modulation depth of 84% has been obtained for a switching power of 78 mW within an interaction length of 80 μm. Reduction by one order of magnitude in the length of the device active region compared with the conventional silicon rib or strip waveguide based MZIs has been experimentally demonstrated.

A p-i-n diode based photonic crystal silicon electro-optic silicon MZI modulator has been proposed and fabricated. By incorporating photonic crystal waveguides into the MZI structure, device size has been reduced by more than one order of magnitude compared to the conventional devices. Optical simulation based on the plane wave expansion method has been performed to reveal how slow group velocity in the silicon PCW dramatically increases the induced phase shift in the MZI devices. The simulated mode profile of the guided mode in photonic crystal waveguide indicated that the intrinsic region of the p-i-n diode should be wider than 1.5 μm to avoid the additional propagation loss due to the free-carrier absorption. Extensive electrical analyses were performed to estimate device switching behaviors and time-dependent distributions of the carrier injection. Simulations showed a speed advantage using a unique electric driving signal which is composed of an over-bias voltage at the on state and a reverse-bias voltage at the off state. It was predicted by the simulation that the modulator with a width of the intrinsic region of 1.5 μm is capable of operating at a frequency in the 10 GHz region. The high-speed optical modulation at 1 Gbit s^{-1} has been experimentally demonstrated in a photonic crystal silicon electro-optical silicon MZI modulator with an interaction length of 80 μm. The thermo-optic effect due to the current inject was also analyzed.

Appendix

Publications

1. **Lanlan GU**, W. Jiang, X. Chen, L. Wang, and R. T. Chen , *Physical mechanism of p-i-n diode based photonic crystal silicon electro-optic modulators for GHz operation*, (to be submitted, 2007).
2. **Lanlan GU**, W. Jiang, X. Chen, L. Wang, and R. T. Chen et al., *High speed silicon photonic crystal waveguide modulator for low voltage operation,* APPLIED PHYSICS LETTER, 90, 071105-1-3 (2007).
3. **Lanlan GU**, Wei Jiang, Xiaonan Chen, Ray T. Chen, *Thermo-optically-tuned photonic crystal silicon-on-insulator Mach-Zehnder interferometers,* IEEE PHOTONIC TECHNOLOGY LETTER, 19, 342-344 (2007).
4. **Lanlan GU**, Xiaonan Chen, Zhong Shi, Brie Howley, Jian Liu, Ray T Chen, *Bandwidth-enhanced volume grating for dense wavelength-division multiplexer using a phase-compensation scheme,* APPLIED PHYSICS LETTER, 86, 181103-1-3 (2005).
5. **Lanlan GU**, Xiaonan Chen, Wei Jiang, Brie Howley, Ray T Chen, *Fringing-field minimization in liquid-crystal-based high-resolution switchable gratings*, APPLIED PHYSICS LETTER, 87, 201106-1-3 (2005).
6. **Lanlan GU** , Feng Zhao, Zhong Shi, Jian Liu, Ray T Chen, *Four-channel coarse WDM for inter- and intra-satellite optical oommunications*, OPTICS AND LASER TECHNOLOGY, 37, 551-554 (2005).
7. **Lanlan GU**, Xiong ZH, Chen G, Xiao ZS, Gong DW, Hou XY, Wang X , *Luminescent erbium-doped porous silicon bilayer structures,* ADVANCED MATERIALS, 13(18), 1402-1405 (2001).
8. **Lanlan GU**, Xiong ZH, Chen G, Xu SH, *Photoluminescence of erbium-doped porous silicon prepared by anodic etching of molecular beam epitaxial growth,* ACTA PHYSICA SINICA, 49 (2), 383-387 (2000).
9. **Lanlan GU**, Wei Jiang, X. Chen, R. T. Chen, *Silicon Photonic Crystal Waveguide Modulators*, IEEE/LEOS Group IV Photonic, Ottawa, Ontario, Canada, September 13-15, 2006, WC5, pp.43-45 (2006). (**Invited**)

10. **Lanlan GU**, Wei Jiang, X. Chen, R. T. Chen, *Silicon Modulators Based On Photonic-Crystal Waveguides*, SPIE Asia-Pacific Optical communications, Gwangiu, Korean, September, 2006. ((**Invited**))

11. **Lanlan Gu**, Wei Jiang, Yongqiang Jiang, Xiaonan Chen, Ray T. Chen, Photonic-crystal-waveguide based Si Mach-Zehnder modulator , Integrated Photonics Research and Applications (IPRA) Topical Meeting/ Nanophotonics (NANO) Topical Meeting, Uncasville, CT, April, 2006, NWA3, (2006) .

12. **Lanlan GU**, Yongqiang Jiang, Wei Jiang, Xiaonan Chen, Ray T. Chen, *Silicon-on-insulator-based photonic-crystal Mach-Zehnder interferometers*, Proceedings of SPIE (Photonic West 2006, San Jose, CA), vol. 6128, 261-268 (2006).

13. **Lanlan GU**, Xiaonan Chen, Yongqiang Jiang, Jian Liu, Ray T Chen, *High-spatial-frequency liquid crystal phase gratings with double-sided striped electrodes,* Proceedings of SPIE (Photonic West 2005, San Jose, CA), vol. 5741, 180-189 (2005).

14. **Lanlan GU**, Feng Zhao, Zhong Shi, Jian Liu, Ray T. Chen, *Polymer Waveguide hologram based 4-channel coarse WDM for satellite optical communications*, IEEE LEOS Summer Topics, San Diego, CA, WB1.2, Page 69-70 (2004).

15. Li Wang, Wei Jiang, Xiaonan Chen, **Lanlan GU**, Jiaqi Chen, and Ray T. Chen, *Fabrication of polymer photonic crystal superprism structures using polydimethylsiloxane soft molds*, JOURNAL of APPLIED PHYSICS, (accepted) (2007).

16. Xiaonan Chen, Wei Jiang, Jiaqi Chen, **Lanlan GU**, and Ray T. Chen, *20dB-enhanced coupling to slot photonic crystal waveguide using multimode interference coupler*; APPLIED PHYSICS LETTERS (accepted), (2007).

17. Xiaonan Chen, **Lanlan G**U, Wei Jiang, and Ray T. Chen, *Active transmission control based on photonic-crystal MOS capacitor*, Proceedings of SPIE (Photonic West 2007, San Jose, CA), (2007).

18. Xiaonan Chen, Wei Jiang, Jiaqi Chen, **Lanlan GU**, and Ray T. Chen, *High bandwidth silicon photonic-crystal modulator based on vertical MOS capacitor*, The OSA Topical Conference On Nanophotonics 2007, Hangzhou, China, (2007).

19. Xiaonan Chen, Jiaqi Silicon Photonic Chen, **Lanlan GU**, Wei Jiang, and Ray T. Chen, *Photonic Crystal Modulation Device Based On Horizontally Activated MOS capacitor*, International Conference on Group IV Photonics 2007, Tokyo, Japan, (2007).
20. Yongqiang Jiang, **Lanlan GU**, Wei Jiang, Xiaonan Chen, Ray T. Chen, *Ultra-compact current-injected optical modulator based on silicon photonic crystal waveguide*, Proceedings of SPIE (Photonic West 2006, San Jose, CA), vol. 6128, 209-218 (2006)
21. Wei Jiang, Yongqiang Jiang, **Lanlan Gu**, Li Wang, Xiaonan Chen, Ray T. Chen, *Silicon and polymer nanophotonic devices based on photonic crystals*, Proceedings of SPIE (Photonic West 2006, San Jose, CA), vol. 6124, 273-283 (2006).
22. Yongqiang Jiang, Wei Jian, **Lanlan GU,** Xiaonan Chen, Ray T. Chen, *80-micron interaction length silicon photonic crystal waveguide modulator*, APPLIED PHYSICS LETTER, 87, 221105-1-3 (2005).
23. Zhong Shi, **Lanlan GU**, Brie Howley, Yongqiang Jiang, QingJun Zhou, Ray Chen, Yihong Chen, Xiaodong Wang, H. R. Fetterman and George Brost, *True-time-delay modules based on single tunable laser in conjunction with waveguide-hologram for phased array antenna application*, OPTICAL ENGINEERING, 44(8), 084301-1-17 (2005).
24. X. Chen, Z. Shi, **Lanlan GU**, B. Howley, Yongqiang Jiang, etc., *Miniaturized delay-time-enhanced photopolymer waveguide hologram module for phased-array antenna*, IEEE PHOTONIC TECHNOLOGY LETTER, 17(10), 2182-2184 (2005).
25. Wei Jiang, Y. Jiang, **Lanlan GU**, X. Chen, Y. Chen, X. Wang, W. Bai, R.T. Chen, *Photonic crystal devices for wavelength division multiplexing and slow photon generation*, International Symposium on Photonics, Biophotonics and Nanophotonics, Nanjinag, China, May 14-18, 2005. (Invited)

26. Wei Jiang, Y. Jiang, **Lanlan GU**, X. Chen, R.T. Chen, *Photonic crystal devices for wavelength-division-multiplexing and optical modulation*, Proceedings of SPIE (Photonic East 2005, Boston, MA), vol. 6014, 60140F-1-12 (2005).(Invited)

27. Yongqiang Jiang, W. Jiang, X. Chen, **Lanlan GU**, B. Howley, R.T. Chen, *Slow photon generation on silicon nano-photonic-crystal waveguides and applications*, IEEE International Workshop on VLSI Design and Video Technology**,** Suzhou, China, May 28-31, 2005. (Invited).

28. Yongqiang Jiang, W. Jiang, X. Chen, B. Howley, **Lanlan GU**, R.T. Chen, *Nano-photonic crystal waveguides for ultra-compact tunable true time delay lines*, Proceedings of SPIE, (Photonic West 2005, San Jose, CA) vol. 5733, 166-175 (2005).

29. Jian Liu, **Lanlan GU,** Ray T. Chen, Douglas Craig, *WDM polymer substrate mode photonic interconnects for satellite communications*, Proceedings of SPIE (Photonic West 2004, San Jose, CA), vol.5358, 146-158 (2004).(Invited)

30. Zhong Shi, **Lanlan GU**, Yongqiang Jiang, Brie Howley, Yihong Chen, Ray T. Chen, *Holographic-grating-based optical-controlled true-time-delay devices*, Proceedings of SPIE (Photonic West 2004, San Jose, CA), vol. 5363, 04-S1 (2004).

31. Xu SH, Xiong ZH, **Lanlan GU,** Liu Y, Ding XM, Zi J, Hou XY, *Photon confinement in one-dimensional photonic quantum-well structures of nanoporous silicon,* SOLID STATE COMMUNICATIONS, 126 (3), 125-128 (2003).

32. Xu SH, Xiong ZH, **Lanlan GU**, Liu Y, Ding XM, Zi J, Hou XY, *Preparation of one-dimensional porous silicon photonic quantum-well structures,* APPLIED PHYSICS A-MATERIALS SCIENCE & PROCESSING, 76 (4), 589-592 (2003).

33. Xu SH, Xiong ZH, **Lanlan GU**, Liu Y, Ding XM, Zi J, Hou XY, *Narrow-line light emission from porous silicon multilayers and microcavities,* SEMICONDUCTOR SCIENCE AND TECHNOLOGY, 17 (9), 1004-1007 (2002).

34. Xu SH, Xiong ZH, **Lanlan GU**, Liu Y, Ding XM, Hou XY, *Narrow-line light emission from porous silicon microcavities prepared by pulsed electrochemical*

etching method, CHINESE JOURNAL OF SEMICONDUCTORS**,** 23 (3), 272-275 (2002).

35. Xiao ZS, Xu F, Zhang TH, Cheng G, **Lanlan GU,** *Erbium-doped optical waveguide materials based on Si nanocrystals formed by metal vapour vacuum arc ion implantation,* JOURNAL OF PHYSICS-CONDENSED MATTER, 14 (44), 11315-11320 (2002).

36. Xu F, Xiao ZS, Cheng GA, Yi ZZ, Zhang TH, **Lanlan GU**, Wang X, *High concentration erbium doping of silicon-rich SiO_2 thin films on silicon,* THIN SOLID FILMS, 410 (1-2), 94-100 (2002).

37. Xiong ZH, Liao LS, Ding XM, Xu SH, Liu Y, **Lanlan GU**, Tao FG, Lee ST, Hou XY , *Flat layered structure and improved photoluminescence emission from porous silicon microcavities formed by pulsed anodic etching,* APPLIED PHYSICS A-MATERIALS SCIENCE & PROCESSING, 74 (6), 807-811 (2002).

38. Xiao ZS, Xu F, Zhang TH, Cheng GA, **Lanlan GU**, Wan X , *A novel method to achieve 1.54 μm light emission from silica thin films,* JOURNAL OF LUMINESCENCE, 96 (2-4), 195-200 (2002).

39. Xu F, Xiao ZS, Cheng GA, Yi ZZ, Zhang TH, **Lanlan GU**, Wang X*, Erbium-doped silicon-rich silicon dioxide/silicon thin films fabricated by metal vapour vacuum arc ion source implantation,* JOURNAL OF PHYSICS-CONDENSED MATTER, 14, L63-L69 (2002).

40. Xiao ZS, Xu F, Zhang TH, Cheng GA, **GU Lanlan,** *Photoluminescence from Si and Er dual-implanted Si-rich thermal oxidation SiO_2/Si thin films,* SPECTROSCOPY AND SPECTRAL ANALYSIS, 22 (4), 538-541 (2002).

41. Xu F, Xiao ZS, Cheng GA, Yi ZZ, Zeng YX, Zhang TH, **GU Lanlan**, *Photoluminescence around 1. 54 μm wavelength from erbium–doped silicon dependence on annealing temperature,* NUCLEAR TECHNIQUES, 25 (8), 631-636 (2002).

42. Xu F, Xiao ZS, Cheng GA, Yi ZZ, Zeng YX, Zhang TH, **GU Lanlan**, *Microstructure of erbium-doped Si-rich thermal oxidation SiO_2/Si*

luminescent thin films, SPECTROSCOPY AND SPECTRAL ANALYSIS, 21 (6), 758-762 (2001).

43. Xiao ZS, Xu F, Zhang TH, Cheng GA, Xie DT, **Lanlan GU***, Infrared emission from Si implanted with high Er concentration,* CHINESE PHYSICS, 10 (7), 650-654 (2001).

44. Xiao ZS, Xu F, Zhang TH, Cheng GA, **GU Lanlan**, *A novel approach of photoluminescence from erbium-doped silicon-based materials,* ACTA PHYSICA SINICA, 50 (1),164-168 (2001).

45. Xu F, Xiao ZS, Cheng GA, Yi ZZ, Zeng YX, Zhang TH, **GU Lanlan**, Surface structure and *1. 54 μm light emission of silicon plus Erbium dual-implanted thermal SiO_2 / Si thin film,* CHINESE JOURNAL OF SEMICONDUCTORS**,** 22 (10), 1258-1263 (2001).

46. Xu F, Xiao ZS, Zhang TH, Cheng GA, Yi ZZ, Zeng YX, **GU Lanlan**, *Near-infrared light emission from single crystal silicon dually implanted with erbium and silicon,* JOURNAL OF BEIJING NORMAL UNIVERISTY (NATURAL SCIENCE), 37 (4), 476-481 (2001).

47. Xiao ZS, Xu F, Zhang TH, Cheng GA, **GU Lanlan,** *Formation and properties of nanometer Er-doped Si-based thin film materials,* JOURNAL OF BEIJING NORMAL UNIVERISTY (NATURAL SCIENCE)**,** 37 (4), 482-487 (2001).

48. Xiao ZS, Xu F, Zhang TH, Cheng GA, Yang XZ, **GU Lanlan,** Wang X, *Current status and prospect of investigation on luminescence of erbium-doped silicon*, JOURNAL OF MATERIALS, 14(10), 26-28 (2000).

Bibliography

1. Christopher Palmer, *Diffraction Gratings Handbook*, Thermo RGL, 2002.
2. M. C. Hutley, *Diffraction gratings*, Academic Press (1981).
3. T. K. Gaylord, "Analysis and applications of optical diffraction by gratings," Proceedings of The IEEE, **73,** 894-938 **(**1985).
4. E. Yablonovitch, Phys. Rev. Lett., **58**, 1059 (1987).
5. S. John, Phys. Rev. Lett., **58**, 2486 (1987).
6. J. D. Joannopoulos, R. D. Meade, and J. Winn, *Photonic Crystals*, Princeton University Press (1995).
7. S. G. Johnson, and J. D. Joannopoulos, *Photonic crystals: road from theory to practice*, Kluwer Academic Publishers (2002)
8. S. Noda, and T. Baba, Roadmap on photonic crystals, Kluwer Academic Publishers (2002).
9. K. Inoue K.Ohtaka, *Photonic crystals: physics, fabrication and applications*, Springer (2004).
10. E. Yablonovitch, T. J. Gmitter and K. J. Leung, Phys. Rev. Lett., **67**, 2295, (1991).
11. S. Noda, K. Tomoda, N. Yamanoto, and A. Chutinan, Science, **289**, 604 (2000).
12. M. G. Moharam, T. K. Gaylord, and R. Mafnusson, "Criteria for raman-nath regime diffraction by phase gratings," Optics Communications, **32**, 19-23 (1980).
13. M. G. Moharam, T. K. Gaylord, and R. Mafnusson, "Criteria for Bragg regime diffraction by phase gratings," Optics Communications, **32**, 14-18 (1980).
14. J. W. Goodman, *Introduction to Fourier Optics*, McGraw-Hill, New York (1996).
15. O. Painter, R. K. Lee, A. Yariv, J. D. O'Brien, P/ D. Dapkus, and I. Kim, Science, **284,** 1819 (1999).
16. J. K. Hwang, H. Y. Ryu, D. S. Song, I. Y. Han, H. W. Song, H. K. Park, and Y. H. Lee, Appl. Phys. Lett. **76**, 2982 (2000).
17. M. Meier, A. Mekis, A. Dodabolapur, A. Timko, R. E. Slusher, J. D. Joannopoulos, and O. Nalamasu, Appl. Phys. Lett. **74**, 7 (1999).
18. S. Fan, P. R. Villeneuve, J. D. Joanopoulos, and E. F. Schubert, Phys. Rev. Lett., **78**, 3294 (1997).

19. N. Lindgren, “Optical communication- A decade of preparations,” Proc. IEEE-Special Issue Opt. Commun, **58**, p. 1410-1421 (1970).

20. ASTRIUM, UK. First ever laser communication between satellites. [Online]. Available: http://www.ukspace.com/press/press105.htm, (2001).

21. W. H. Mott IV, R. B. Sheldon, P. O. McVay, L. P. Sheldon. *Laser Satellite Communication-The Third Generation*, Westport, CT: Greenwood Publishing , (2000).

22. G. D. Fletcher, T. R. Hicks, B. Laurent. “The SILEX optical interorbit link experiment,” Electronics & Commun Eng. J, 273-279, (1991).

23. C. Mahle, K. Bhasin, C. Bostian, W. Brandon, A. M. Rae S. Townes. “Key technology trends--Satellite systems,” [Online]. Available: http://www.wtec.org/loyola/satcom2/03_06.htm), (1998).

24. J. Bland-Hawthorn, A. Harwit, M. Harwit. “Laser Telemetry from Space,” Science, **297**, 523 (2002).

25. F. Zhao, J. Qiao, X. Deng, J. Zou, B. Guo, R. Collins etal. “Reliable grating-based wavelength division (de)multiplexers for optical networks,”Opt. Eng., **40**, 1204-1211 (2001).

26. H. Kogelnik, “Coupled wave theory for thick hologram gratings,” The Bell Sys. Tech. J. **13**. 2909-2947 (1969).

27. A. M. Weber, W. K. Smothers, T. J. Trout, and D. J. Mickish, “Hologram recording in Du Pont’s new photopolymer materials,” Practical Holography IV, SPIE OE, Laser Conference Proceedings, 1212-04 (1990).

28. W. J. Gambogi, W. A. Gerstadt, S. R. Mackara and A. M. Weber, “Holographic transmission elements using improved photopolymer films,” SPIE Computer and Optically Generated Holographic Optics, **1555**, 256-267 (1991).

29. Jian Liu, *Multi-wavelength planar optoelectronic interconnections*, Ph.D. Diss., The University of Texas at Austin, (1999).

30. Jie Qiao, *Dense wavelength division multiplexing (DWDM) for optical networks*, The University of Texas at Austin, (2001).

31. Xuliang Han, *Fan-out equalized shared optical back-plane buses*, The University of Texas at Austin, (2003).

32. J. Liu, and R. T. Chen, “Path-reversed substrate-guided-wave optical interconnects for wavelength-division demultiplexing,” Applied Optics, **38**, 3046-3052 (1999).

33. N. Karafolas, and S. Baroni, “Optical Satellite Networks,” J. Lightwave Technol., **18**, 1792-1806 (2000).

34. Yi-Kong Tsai, Yang-Tung Huang, and Der-Chin Su. Multiband, “wavelength-division demultiplexing with a cascaded substrate-mode grating structure,” Applied Optics, **34**, 5582-5588 (1995).

35. J. Liu, L. Gu, R. T. Chen, and D. Craig, “WDM Polymer Substrate Mode Photonic Interconnects for Satellite Communications,” Proc. of SPIE,5358, 146-158 (2004).

36. B. Moslehi, P. Harvey, J. Ng, and T. Jannson, “ Fiber-optic wavelength-division multiplexing and demultiplexing using volume holographic gratings,” Optics Letter, **14**, 1088-1090 (1989).

37. Jun-Won An, Nam Kim, and Kwon-Yeon Lee, “50 GHz-Spaced 42-Chinnel Demultiplexer Based on the Photopolymer Volume Grating,” Jpn. J. Appl. Phys, **41**, L665-L666 (2002).

38. Jie Qiao, Feng Zhao, Jian Liu, and Ray T. Chen, “Dispersion-Enhanced Volume Holorgram for Dense Wavelength-Division Demultiplexer,” IEEE Photonics Technology Letters, **12**, 1070-1072 (2000).

39. Yang-Tung Huang, Der-Chin Su, and Yi-Kong Tsai, “Wavelength-division-multiplexing and -demultiplexing by using a substrate-mode grating pair,” Optics Letters, **17**, 1629-1631 (1992).

40. Yi-Kong Tsai, Yang-Tung Huang, and Der-Chin Su, “Multiband wavelength-division demultiplexing with a cascaded substrate-mode grating structure,” Applied Optics, **34**, 5582-5588 (1995).

41. Maggie M. Li and Ray T. Chen, “Five-channel surface-normal wavelength-division demultiplexer using substrate-guided waves in conjunction with a polymer-based Littrow hologram,” Optics Letters, **20**, 797-799 (1995).

42. R. R. A. Syms, Practical Volume Holography (Clarendon, Oxford, 1990).

43. Zhong Shi, Lanlan Gu, Yongqiang Jiang, Howley Brie, Yihong Chen, Ray Chen, " Holographic-grating based optical-controlled true-time-delay devices," Proc. SPIE, **5363**, 39-44 (2004).

44. B. J. Chang and C. D. Leonard, "Dichromated gelatin for the fabrication of holographic optical elements," Applied Optics, **18**, 2407-2417 (1979).

45. Ichiro Fujieda, "Liquid-crystal phase grating based on in-plane switching," Applied Optics, **40**, 6552-6209 (2001).

46. Hajime Sakat, and Michiyo Nishimura, "Switchable Zero-Order diffraction filters using fine-fitch phase gratings filled with liquid crystal," Jpn. J. Appl. Phys., **39** , 1516-1521 (2000).

47. Boris Apter, Uzi Efron, and Eldad Bahat-Treidel, "On the fringing-field effect in liquid-crystal beam-steering devices," Applied Optics, **43**, 11-19 (2004).

48. D. P. Resler, D. S. Hobbs, R. C. Sharp, L. J. Friedmanks, and T. A. Dorschner "High-efficiency liquid-crystal optical phased-array beam steering," Optics Letters, **21**, 689-691 (1996).

49. Jae-Hong Park, Chang-Jae Yu, Jinyool Kim, Sung-Yeop Chung, and Sin-Doo Lee, "Concept of a liquid-crystal polarization beamsplitter based on binary phase gratings," Applied Physics Letter, **83**, 1918-1920 (2003).

50. Manuel Bouvier, and Toralf Scharf, "Analysis of nematic-liquid-crystal binary gratings with high spatial frequency," Opt. Eng., **39**, 2129-2137 (2000).

51. R. G. Lindquist, J. H. Kulick, G. P. Nordin, J. M. Jarem, S. T. Kowel, and M. Friends "High-resolution liquid-crystal phase grating formed by fringing fields from interdigitated electrodes," Optics Letters, **19**, 670-672 (1994).

52. J. Chen, P. J. Bos, H. Vithana, and D. L. Johnson," An electro-optically controlled liquid crystal diffraction grating," Applied Physics Letter, **67**, 2588-2590 (1995).

53. Chang-Jae Yu , Jae-Hong Park, , Jinyool Kim, Min-Sik Juang, and Sin-Doo Lee, "Design of binary diffraction gratins of liquid crystals in a linearly graded phase model," Applied Optics, **43**, 1783-1787 (2004).

54. Mary Lou Jepsen and Hendrik J. Gerritsen, "Liquid-crystal-filled gratings with high diffraction efficiency," Optics Letters., **21**, 1081-1083 (1996).

55. Emil Hallstig, Johan Stigwall, Torleif Martin, Lars Sjoqvist nd Mikael Lindgren, “Fringing fields in a liquid crystal spatial light modulator for beam steering,” Journal of Modern Optics, **51**, 1233-1247 (2004).

56. Richard James, F. Anibal Fernandez and Sally E. Day, “ Modelling of high resolution phase spatial light modulator,” Mol. Cryst. Liq. Cryst, **422**, 209-217 (2004).

57. Jeffrey H. Kulick, Jphn M. Jarem, Robert G. Lindquist, Stephen T.Kowel, Mark W. Friends, and Thomas M. Lesile, “Electrostatic and diffraction analysis of a liquid-crystal device utilizing fringing fields: applications to three-dimensional displays,” Applied Optics, **34**, 1901-1922 (1995).

58. Ichiro Fujieda, Osamu Mikami, and Atsushi Ozawa, “Active optical interconnect based on liquid-crystal grating,” Applied Optics, **42**, 1520-1525 (2003).

59. M. Kitamura, “Computer simulation of director profile in two dimensional electric field,” SID-IDRC, 350-353, presented at the International Display Research Conference, Monterey, CA, (1994).

60. P. Yeh, C. Gu, *Optics of liquid crystal displays*, A Wiley Interscience Publication, (1999).

61. G. Cocorullo, M. Iodice, I. Rendina, and P. M. Sarro, “Silicon thermaloptical micromodulator with 700-kHz-3-dB bandwidth,” IEEE. Photonic technology letters, **7**, 363 (1995)

62. G. V. Treyz, “Silicon Mach-Zehnder waveguide interferometer operating at 1.3 μm”, Electronics Letters, **27**, 118-120 (1991).

63. U. Fischer, T. Zinker, B. Schuppert and K. Petermann, “Singlemode optical switches based on SOI waveguides with large cross-section,” Electronics Letters, **30**, 406-408 (1994).

64. A. Liu, R. Jones, L. Liao, D. Samara-Rubio, D. Rubin, O. Cohen, R. Nicolaescu, and M. Paniccia, “A high-speed silicon optical modulator based on a metal-oxide-semiconductor capacitor,” *Nature*, vol. 427, pp. 615-618 (2004).

65. Y. Jiang, W Jiang, L. Gu, X. Chen, and R. T. Chen, “80-micron interaction length silicon nano-photonic crystal waveguide modulator,” Appl. Phy. Lett., **87**, 221105-1-221105-3 (2005).

66. E. A. Camargo, H. M. H. Chong and R. M. De La Rue, “2D photonic crystal thermal-optic switch based on AlGaAs/GaAs epitaxial structure,” Opt. Express, vol. 12, 588-592 (2004).

67. D. W. Prather, S. Shi, D. Pustai, C. Chen, S. Venkataraman, A. Sharkawy, G. J. Scheider, and J. Murakowski, “Dispersion-based optical routing in photonic crystals, ” Optics Lett., **29,** 50-52, (2004).

68. Y. A. Vlasov, Martin O’Boyle, Hendrik F. Hamann, and S. J. McNab, “Active control of slow light on a chip with photonic crystal waveguides,” Nature, **438**, 65-68 (2005).

69. M. T. Tinker, and J-B. Lee, “Thermo-optic photonic crystal light modulator,” Appl. Phy. Lett., **86**, 221111-1-221111-3 (2005).

70. M. Notomi, K. Yamada, A. Shinya, J. Takahashi, C. Takahashi, and I. Yokohama “Extremely Large Group-Velocity Dispersion of Line-defect Waveguides in Photonic Crystal Slabs,” Phys. Rev. Lett., **87**, 253902-1-253902-4 (2001).

71. M Soljacic, S. G. Johnson, S. Fan, M. Ibanescu, E. Ippen, J. D. Joannopoulos, “Photonic-crystal slow-light enhancement of nonlinear phase sensitivity,” *J. Opt. Soc. Am. B,* **19**, 2052 (2002).

72. M. Soljacic, and J.D. Joannopoulos, “Enhancement of non-linear effect using photonic crystals,” Nature materials, **3**, 211 (2004).

73. T. Asano, K. Kiyota, D. Kumamoto, B.S. Song, S. Noda, “Time-domain measurement of picosecond light-pulse propagation in a two-dimensional photonic crystal-slab waveguide”, App. Phys. Lett., **84**, 4690-4692 (2004).

74. D. Mori, T. Baba, “Dispersion-controlled optical group delay by chirped photonic crystal waveguides”, App. Phys. Lett., **85**, pp. 1101-1103 (2004).

75. T.J. Karle, Y.J. Chai, C.N. Morgan, I.H. White, T.F. Krauss, “Observation of pulse compression in photonic crystal coupled cavity waveguide”, Journal of lightwave technology, **22**, 514-519 (2004).

76. E. Kuramochi, S. Hughes, T. Watanabe, L. Rumunno, A. Shinya, M. Notomi, “Low loss photonic crystal slab waveguides: fabrication, experiment, and theory”**,** LEOS Annual Meeting, **2**, 505 – 506 (2004).

77. T. Baba, A. Motegi, T. Iwai, N. Fukaya, Y. Watanabe, and A. Sakai, " Light propagation characteristics of straight single-line-defect waveguides in photonic crystal slabs frabricated into a silicon-on-insulator substrate," IEEE J. Quantum Electron. **38**, 743-752 (2002).

78. M. L. Povinelli, S. G. Johnson, J. D. Joannopoulos, "Slow-light, band-edge waveguides for tunable time delays," Optics Express, **13**, 7145-7159 (2005)

79. L. Gu, Y Jiang, W Jiang, X Chen, R. T. Chen, "Silicon-on-insulator-based photonic-crystal Mach-Zehnder interferometers, " Proceedings of SPIE*,* **6128**, 261 (2006).

80. T. Chu, H. Yamada, S. Ishida, and Y. Arakawa, "Thermooptic switch based on photonic- crystal line-defect waveguides," IEEE. Photon. Technol. lett., **17**, 2083-2085 (2005).

81. T. Chu, Hirohito Yamada, Satomi Ishida, and Yasuhiko Arakawa, "Thermo-optic switch based on 2D-Si photonic crystals," Technical Digest of 1st IEEE lntemational Conference on Group IV Photonics, FC3, **174** (2004).

82. M. T. Tinker, and J-B. Lee, "Thermal and optical simulation of a photonic crystal light modulator based on the thermo-optic shift of the cut-off frequency," Opt. Express, **13**, 7174-7188 (2005).

83. R. A. Soref, B. R. Bennett, "Electrooptical effects in silicon," IEEE J. Quantum Electron. **23**, 123-129 (1987).

84. Richard Soref, "Silicon photonics technology: past, present and future," Proc. SPIE , **5730**, 19-28 (2005).

85. G. V. Treyz, P. G. May, and Jean-Marc Halbout, "Silicon Mach-Zehnder waveguide interferometers based on the plasma dispersion effect," Appl. Phys. Lett., **59**, 771 (1991).

86. C. Z. Zhao, G. Z. Li, E. K. Liu, Y. Gao, and X. D. Liu, "Silicon on insulator Mach-Zehnder waveguide interferometers operating at 1.3 μm" Appl. Phys. Lett., **67**, 2448 (1995).

87. P. Dainesi, A. Kung, M. Chabloz, A. Lagos, Ph. Fluckiger, A. Ionescu, P. Fazan, M. Declerq, Ph. Renaud, and Ph. Robert, "CMOS compatible fully integrated

Mach-Zehnder Interferometer in SOI Technology," Photonics Technol. Lett., **12**, 660 (2000).

88. L. Liao, D. Samara-Rubio, M. Morse, A. Liu, D. Hodge, D. Rubin, U. D. Keil and T. Franck, " High speed silicon Mach-Zehnder modulator," Optics Express, **13**, 3129-3135 (2005).
89. A. Cutolo, M. Iodice, P. Spirito, and L. Zeni, "Silicon electro-optic modulator based on a three terminal device integrated in a low-loss single-mode SOI waveguide," J. Lightwave Technol., **15**, 505-518 (1997).
90. A. Irace, G Breglio, and A. Cutolo, "All-silicon optoelectronic modulator with 1 GHz switching capability," Electron. Lett., **39**, 232 (2003).
91. C. E. Png, S. P. Chan, S. T. Lim, and G. T. Reed, "Optical phase modulator for MHz and GHz modulation in silicon-on-insulator (SOI)," J. Lightwave Technol., **22**, 1573 (2004).
92. F. Gan, and F. X. Kartner, "High-speed silicon electrooptic modulator design, " IEEE Photonics Technol. Lett., **17**, 1007-1009 (2005).
93. F. Y. Gardes, G. T. Reed, and N. G. Emerson, "A sub-micron depletion-type photonic modulator in silicon on insulator," Optics Express, **13**, 8845-8853 (2005).
94. Q. Xu, B. Schmidt, S. Pradhan, and M. Lipson, "Micrometre-scale silicon electro-optic modulator," Nature, **435**, 325-327 (2005).
95. A. A. Barrios, V. R. Almeida, R. Panepucci, and M. Lipson, "Electrooptic modulation of silicon-on-insulator submicrometer-size waveguide devices," J. Lightwave Technol., **21**, 2332 (2003).
96. A. A. Barrios, V. R. Almeida, M. Lipson, "Low-power-consumption short-length and high-modulation-depth silicon electrooptic modulator," J. Lightwave Technol., **21**, 1089-1098 (2003).
97. J. Muller, "Thin silicon film p-i-n photodiodes with internal reflection," IEEE J. Solid-State Circ. **13**, 173-179 (1978).
98. G. Cocorullo, M. Iodice, I. Rendina, and P. M. Sarro, "Silicon thermo-optical micro-modulator with 700 kHz-3 dB bandwidth," IEEE Photonics Technol. Lett., **7**, 363-365 (1995).

99. J. Yonekura, M. Ikeda, and T. Baba, J. Lightwave Technol., **17**, 1500 (1999).

100. S. G. Johnson, S. Fan, P. R. Villeneuve, and J. D. Joannopoulos, “ Guided modes in photonic crystal slabs”, Phys. Rev. B. **60**, 5751-5758(1999)

101. M. Notomi et al “Structure tuning of guiding modes of line-defect waveguides for planar lightwave circuit applications”, IEEE J. Quantum Electron., **38**, 736-742 (2002).

Vita

Lanlan Gu was born in Shanghai, China, on November 22, in 1975, the daughter of Xinbao GU and Xiuying JIANG. After completing her education at Caoyang Middle School, Shanghai, China, in 1994, she entered Fudan University, Shanghai, China. She received the Bachelor of Science and Master of Science from Department of Physics, Fudan University in 1998 and 2001, respectively. In September 2001, she entered Graduate School of The University of Texas at Austin. In January 2003, she joined the Department of Electrical and Computer Engineering at The University of Texas at Austin.

Permanent Address: Changshou Rd, 15/17A
Shanghai 600063
China

This dissertation was typed by the author.